First Principles Modelling of the Thermoelectric Properties of Half-Heusler Alloys

Kamil Domosud

Department of Physics and Astronomy
Royal Holloway, University of London

This dissertation is submitted for the degree of
Doctor of Philosophy

November 2021

Declaration

I declare that except where specific reference is made to the work of others, the work presented in this thesis is original and has not been submitted in whole or in part for consideration for any other degree or qualification in this, or any other university. This thesis is my own work and contains nothing which is the outcome of work done in collaboration with others, except as specified in the text and Acknowledgements. This dissertation contains fewer than 100,000 words including appendices, bibliography, footnotes, tables and equations and has fewer than 150 figures. Parts of this work have been published in the Journal of Materials Chemistry A.

Chapter 4 describes collaborative work containing results of inelastic neutron scattering measurements collected using the MARI spectrometer at Harwell. My collaborators Jan-Willem Bos and Srinivas Popuri were in charge of synthesising the half-Heusler compositions. I took part in the neutron scattering experiment at Harwell, under the lead and supervision of Duc Le. In addition, I performed the data reduction for the results presented in this thesis.

Chapter 5 describes collaborative work that has been published:
S. A. Barczak and R. J. Quinn and J. E. Halpin and K. Domosud and R. I. Smith and A. R. Baker and E. Don and I. Forbes and K. Refson and D. A. MacLaren and J. W. G. Bos, "Suppression of thermal conductivity without impeding electron mobility in n-type XNiSn half-Heusler thermoelectrics", Journal of Materials Chemistry A, 7:27124–27134, 2019.

Kamil Domosud

Abstract

Thermoelectric materials enable the conversion of a thermal gradient into electricity, making them candidates in applications such as waste heat recovery. Their efficiency is determined by key, often interdependent, electrical and thermal transport properties. Therefore, requiring complex optimisation of the chemical composition and synthesis process.

In this thesis, I perform first-principles modelling of the thermoelectric properties of half-Heusler alloys focused on analysis of XNiSn (X = Ti, Zr, Hf) and $Nb_{1-x}CoSb_ySn_{1-y}$ based compositions. Thermoelectric properties of complex defective supercells were performed using plane-wave DFT as implemented in CASTEP and by solving the phonon Boltzmann Transport equation and the modified Debye-Callaway model to estimate κ_l.

We successfully use the non-diagonal supercell method, phonon unfolding, and neutron weighting techniques to analyse vibrational spectra in defective half-Heuslers and compare against inelastic neutron scattering experiments performed with our collaborators. We determine that Ni interstitial vacancy clustering results in agreement with experiments. We find a reduction of the κ_l in defective $TiNi_{1.125}Sn$ and establish importance of grain boundaries.

We model the effect of interstitials on the electronic structure in n-type XNiSn (X = Ti, Zr, Hf) compositions. Interstitial Cu in TiNiSn has been experimentally observed to reduce κ_l without impeding electron mobility [1]. A promising thermoelectric with a ZT value of 0.8 at 773K. The electronic structure is investigated using DFT and DFT+U, charged calculations, and meta-GGA treatment of the exchange and correlation, considering possible localisation effects.

We determine the effect of X-site vacancies in defective n-type $Nb_{1-x}CoSb_ySn_{1-y}$ compositions, tuned to lower the average electron count, mimicking the unique, closed shell 18-electron half-Heusler system. Results predict semi-conducting behaviour in correspondence with experiments.

The calculations successfully model thermoelectric properties of stoichiometric and defective half-Heusler compositions in good agreement with experiments. This predictive power can be used in future research to aid in the optimisation of thermoelectric materials.

Acknowledgements

Firstly, I would like to sincerely thank my supervisor Keith Refson for his continuous support during my PhD studies and his wisdom and mentorship to help me grow academically and as a person through the many ups and downs. I will remember the thoughtfulness and generosity you have given me.

I am grateful for computational support from the UK national high-performance computing service, ARCHER, for which access was obtained via the UKCP consortium and funded by EPSRC grant ref EP/P022057/1. I would also like to thank for the computing resources which were provided by STFC Scientific Computing Department's SCARF cluster.

Thank you to my collaborators Jan-Willem Bos, Donald MacLaren, and Srinivas Popuri for their advice during our project meetings and for the hospitality during my visits to Scotland. Especially, Jan-Willem Bos who has given me feedback when I needed it. And, to Duc Le for his time during our experiments in Harwell.

I am thankful to Phil Meeson for his help as my secondary supervisor and Jon Goff for his guidance as my academic advisor. I would also like to thank Giovanni Sordi for his kindness, I very much enjoyed marking coursework for your students.

I am grateful to my friends and colleagues Joseph Blake and Yusuf Aziz, during the days that we were able to share an office together you always made them memorable.

I wish to acknowledge the enormous support and abundance of love that I've received from my family and my partner, Dayanara; my parents, Tomila and Jacek; my brothers, Matthew and Karol; my sister, Paulina; and my grandparents, Tadeusz and Anna. They have never stopped believing in me and this would not have been possible without their support to allow me to focus on my studies.

Finally, I wish to thank all my friends for never failing to provide me with the much-needed entertainment and being there at times of need.

Table of contents

List of figures

List of tables

Nomenclature

Greek Symbols

η	thermoelectric efficiency
γ	mode Grüneisen parameter
κ_e	electronic thermal conductivity
κ_l	lattice thermal conductivity
μ_e	electron mobility
σ_l	electrical conductivity

Acronyms / Abbreviations

BTE	Boltzmann transport qquation
BZ	Brillouin Zone
CBM	Conduction band minimum
DFPT	Density functional perturbation theory
DFT	Density functional theory
DMFT	Dynamical mean-field theory
DOS	Density of states
EBS	Effective band structure
fcc	Face-centered cubic
GGA	Generalised gradient approximation
IBZ	Irreducible Brillouin Zone
IFC	Interatomic force constant
INS	Inelastic neutron scattering

LDA Local density approximation

LSDA Local spin density approximation

NHS National Health Service

NIST National Institute of Standards and Technology

PGEC Phonon-glass-electron-crystal

RTA Relaxation time approximation

RTEG Radioactive thermoelectric generator

SPS Spark-plasma-sintering

TEC Thermoelectric cooler

TEG Thermoelectric generator

TE thermoelectric

USP Ultrasoft Pseudopotential

VBM Valence band maximum

WSN Wireless sensing networks

ZT Thermoelectric figure of merit

Chapter 1

Introduction

The energy demand of modern society results in a heavy dependence on fossil fuels, which are polluting the air and raising sustainability concerns all over the world with many countries aiming to reduce their greenhouse gas emissions [2]. One route to address this demand is through the development of renewable energy sources, but that is not the only way to go forward as energy efficiency technologies can also play an important role in reducing carbon footprint. The latter forms a key component of this thesis, exploiting the phenomenon of thermoelectricity and its associated technological applications where we will explore the properties of candidate materials for the construction of thermoelectric devices.

The thermoelectric effect is composed of three separate effects called the Seebeck, Peltier, and Thomson effects. The first allows the conversion of heat energy into electrical energy, allowing for the creation of thermoelectric generators (TEGs) using solid-state devices in the presence of a temperature gradient. On the other hand, the Peltier effect allows for a reverse process to occur, where an electric current passed through a solid-state device leads to a cooling effect, which can be designed to create a thermoelectric cooler (TEC) module. It is immediately clear that these are fascinating and powerful phenomena that can find their use in many applications. The performance of thermoelectric materials is characterised using a figure of merit called the ZT ($ZT = S^2\sigma T/\kappa$). Where S is the Seebeck co-efficient, σ is the electrical conductivity, κ is the thermal conductivity for a given temperature T. The power factor is a useful quantity defined as $S^2\sigma$ and determines the amount of work that can be done. Looking at the expression for ZT, we can see that maximising performance requires a large power factor and a low thermal conductivity. What should also be taken into account for device design is the fact that ZT curves vary greatly between materials and the often quoted peak ZT values may be promising, they may occur at temperatures that are not appropriate for the devices operating temperature. Therefore, average ZT values across a wide temperature range should also be taken into consideration. The figure of merit is one of the key estimators to determine the quality of thermoelectric materials with current research efforts aiming to design materials with ZT values > 1. Materials with a ZT of 1 can usually achieve energy conversion efficiencies of

around 5-10% [10, 11]. A longer explanation of thermoelectric performance can be found in Chapter 2.1.

We will be modelling the thermoelectric properties of a family of promising materials for use in thermoelectric devices for the application in waste-heat harvesting. Namely, the investigations found in this work will focus on half-Heusler alloys. This family of materials shows promise in delivering economically viable thermoelectric efficiencies, are of relatively low cost and have a relatively abundant composition. Making them candidates for replacing the current best performing, but toxic thermoelectrics, such as PbTe.

1.1 Applications of thermoelectrics

The market for thermoelectrics has grown considerably to a size of $460 million US dollars in 2019 with a strong forecast for future growth. This growth is estimated by a compound annual growth rate (CAGR) between 8.3-13.8% to reach a size of $1025 million US dollars by 2025 [12, 13]. Thermoelectric applications span a wide range of industry segments due to the versatility of the technology, ranging from automotive, healthcare, consumer or industrial segments and more. This section will highlight some of the key applications of thermoelectrics that we currently benefit from in the present day as well as how the technology may be improved or utilised effectively in future applications. The expected growth and vision for the future of thermoelectrics is promising with a potential timeline shown in Figure. 1.1.

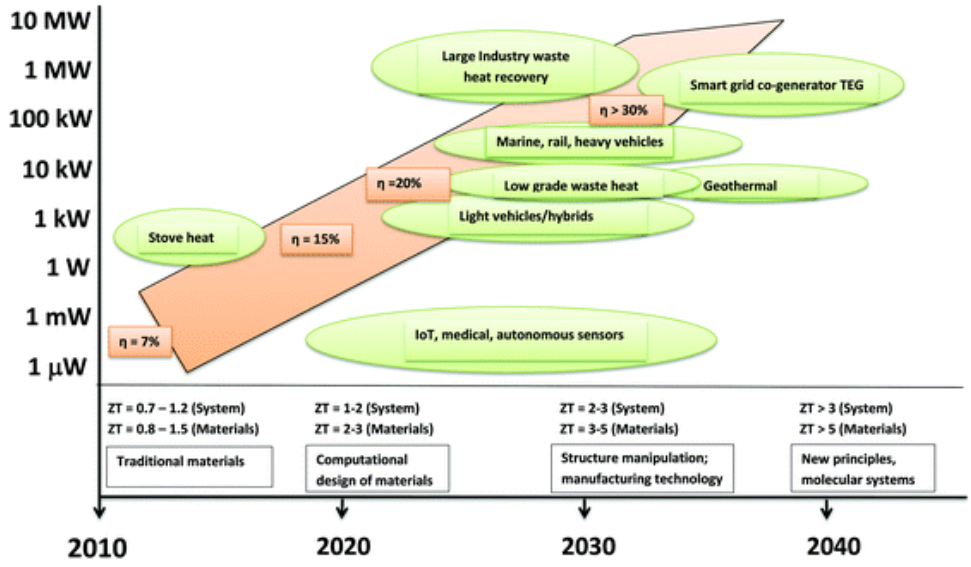

Fig. 1.1 Roadmap for deploying new thermoelectric applications based on required thermoelectric efficiency and power output using projected rate of developments in materials and manufacturing. Image taken from Freer et al. [2] with permission from the Royal Society of Chemistry.

The projected timeline largely depends on the success of scientific research in optimising performance and selecting materials that satisfy many demanding criteria, including

cost, abundance and environmental impact. Nevertheless, the mounting pressure for reducing greenhouse emissions and protecting the environment should act as a driver of development.

1.1.1 Automotive applications

Transportation is known to be one of the key sources of greenhouse emissions with continued legislative pressures for automotive manufacturers to meet carbon dioxide emissions and reduce fuel consumption. Therefore, there is scope for mass-scale deployment of thermoelectric devices utilising the Seebeck effect for the purpose of waste heat harvesting from internal combustion engines. During vehicle operation, waste heat can be extracted from the exhaust and cooling system using a TEG module to generate electric power that could reduce or replace the function of the alternator for powering the vehicle's electrical systems. In addition, provided that enough power can be generated, hybrid car systems could also be powered for further gains inefficiency. The challenges arise due to the fact that there are fluctuations in the cars operating temperature and often require additional components to boost efficiency, such as a liquid heat exchanger, which may require additional components such as valves, sensors, and pumps. This increases cost and weight, which negatively impacts efficiency and economic viability. State of the art modules using bismuth telluride (Bi_2Te_3) proved to produce good power output, but costs were too high to be economically viable as found by a UK funded project called VIPER [2]. Therefore, abundant and relatively low-cost materials that could provide sufficient power output are necessary for mass production. If successful, the technology would be beneficial for many years as the reliance on internal combustion engines is large and the phasing out process is slow. The technology can also be extended to marine transportation, replacing on-board diesel generators for powering the vessel's electronic systems. Moreover, we can also utilise the Peltier effect to enhance the efficiency and design of vehicle accessories for passenger convenience. Luxury vehicles already use thermoelectric modules for heating and cooling of seats, as portable refrigerators, or to keep beverages hot or cold [14]. However, the greatest benefit for re-designing the vehicle convenience systems lies in the heating, ventilation and air-conditioning (HVAC) systems. Thermoelectric technology with sufficient efficiency would replace the current technology composed of a heating core, AC radiator compressor-evaporator system and the required pipes and connections between those systems. Ultimately, reducing the number of required components, resulting in improved reliability and reduced weight [14].

1.1.2 Aerospace applications

Radioactive TEG (RTEG) modules have been a reliable mode of power generation on a number of space exploration missions starting with the very first module being launched into orbit in 1961 [15]. Many missions followed, including the Apollo moon missions

and Voyager deep space exploration missions, with the latter still remaining operational until this day. Most recently, RTEGs are still being used in new missions with NASA launching the Perseverance Mars rover in 2020 using a PbTe/TAGS based TEG module designed to produce around 110W of electrical power [15]. The popularity of the usage of RTEG modules is well justified. The lack of moving parts makes them very reliable and radioactive isotopes such as Plutonium 238 have a long half-life and produce a steady source of thermal power. Mission-specific complexity, such as the Mars missions require the TEG module to withstand sandstorms and reliably generate power on the surface independent of the sun angle, a challenge the alternative solar cell based power supplies have to overcome [16].

Moreover, on earth, commercial and military aircraft currently utilise TEG modules to power a range of devices such as sensors, refrigerator units, and freezers [2]. There is the future scope for waste heat from jet engines, similarly to that of the automotive and marine applications provided efficiency requirements and safety standards can be met.

1.1.3 Medical applications

A significant role of thermoelectrics in medical applications lies in TEC devices in the form of portable medical-grade refrigerators. These devices have been particularly helpful in the roll-out of the Covid vaccines, with new designs being produced by companies such as CoolMed, which have supplied over 500 such refrigerators to the NHS during the Covid-19 pandemic [17]. This enables safe storage and easy transport of vaccines for vaccine administration. As the TEC devices can be scaled down, small portable coolers can be utilised to reach more patients in remote locations and require as little as one person to carry out the transportation. The use of portable thermoelectric coolers extends to transporting other vital substances such as blood. The TEC refrigerators are solid state devices with no moving parts and are gas free, which prevents any possible leaks, reducing the risk of failure.

1.1.4 Other applications

There are a range of other applications of of considerable interest across a range of industries. Wireless sensing networks (WSN) are one such application as the technology could be used as sensors in domestic applications, sports performance tracking, medical diagnostics or even industrial plants and monitoring of aircraft engines [2]. Most applications utilise a bulk thermoelectric module design architecture, composed of alternating n-type and p-type thermoelectric materials that are connected in series and placed in parallel between ceramic plates. However, it is possible to adapt the design of thermoelectric devices though creative fabrication techniques and careful material selection to suit the particular application. For example, the dimensions of the device can be reduced by growing thin-film thermoelectric devices or though the use of organic polymers to produce

flexible devices. A conceptual flexible TEG device can be seen in Figure. 1.2 to illustrate the general design and scale of such a device.

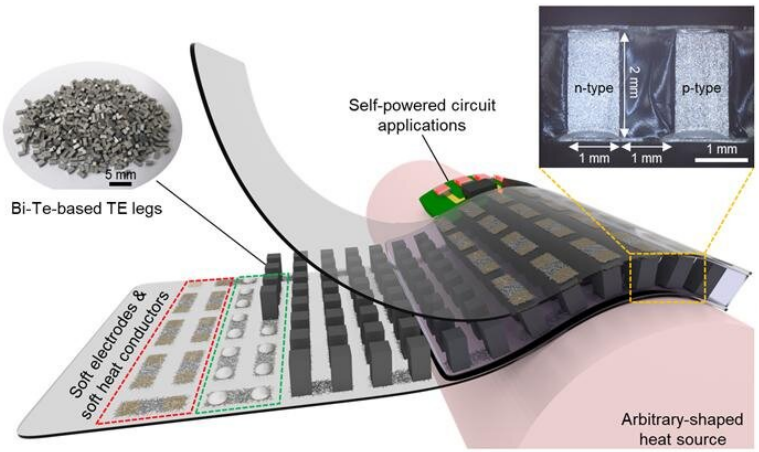

Fig. 1.2 Flexible TEG module design illustration for self-powered circuit applications. Image taken from Lee et al. [3] with permission from Nature Communications.

In the case of WSN the use of thin films would be particularly suitable, especially in the case where small thermal gradients are present during operation, which would allow to reduce the amount of material needed. Another application that would benefit from reduced use of material and flexibility are wearable thermoelectrics in the form of TEGs. On the other hand, the additional complexity of these devices and difficulty in achieving consistency and high quality fabrication [18] of thin film materials are additional challenges on top of ensuring low cost and good thermoelectric performance.

The improved waste-heat harvesting and recovery and more efficient cooling through the use of thermoelectrics offer significant opportunities to reduce energy usage and environmental burdens. Therefore, the nuclear energy industry is an obvious candidate for the technology. Nuclear fission reactors have low operating efficiency at around 25-30% [2] and produce a significant amount of waste heat that could be recovered. In addition, the improved efficiency would reduce the temperature increasing effect on local water reservoirs and rivers due to releasing hot water vapour. Lastly, energy generation of up to an estimated 10MW [2] could be produced using geothermal heat at decommissioned offshore oil platforms if economically viable efficiencies can be achieved.

1.2 Thermoelectric materials

In the previous section, we saw that thermoelectrics span a wide range of applications, each of which come with their own set of criteria related to good performance, economic viability and environmental impact. This means that correct thermoelectric material selection and optimisation are crucial. This is an enormous challenge as we have already seen that maximising the ZT value is a priority for high performing thermoelectric materials, which

is a complex optimisation problem due to the interdependence of S, σ and κ, additional consideration of factors such as earth abundance, cost, performance, stability, scalability, durability, flexibility and toxicity has to be taken into consideration. This greatly constrains the possible material search space, making experimental exploration and discovery difficult. Moreover, emphasis must be placed on developing materials with a large average ZT value over a relevant operating temperature range for the desired application rather than focusing on attaining the largest peak ZT, which may result in lower efficiency despite good peak performance. As a result, computational efforts in materials exploration and design aim to accelerate progress in this direction and provide predictive power to aid experimental endeavors. This section will discuss some of the classically used materials in thermoelectric devices, half-Heuslers that form the basis of this thesis as well as a few other promising types of materials that are currently being researched.

1.2.1 Chalcogenides

Chalcogenides are a benchmark class of materials used for thermoelectrics applications since the 1950's [19]. Traditionally the most common materials were the telluride based Bi_2Te_3 and PbTe, which are both narrow-gap semiconductors with band gaps of 0.16 eV and 0.32 eV respectively [20] and they form a part of a large number of thermoelectric devices in use today. The former Bi_2Te_3 is particularly good in the low temperature range between 20 and 150°C with ZT values of around 1-1.5 [19] and is often the material of choice for cooling applications. Optimisation in performance can be done by alloying Bi_2Te_3 with other compositions of similar crystal structure, such as Bi_2Se_3 or Sb_2Te_3, which increases phonon scattering and improves performance [11]. On the other hand, PbTe performs well over the intermediate and high temperature ranges making it a good thermoelectric for waste heat harvesting applications. Extensive research has been undertaken in the quest of their enhancement and the results in performance improvement of PbTe-based thermoelectrics can be seen in Figure. 1.3, with ZT values under 1 at the time of first discovery in 1960 to around a ZT of 2 for both n-type and p-type compositions. More recent attempts at improving performance in PbTe were based on endotaxially embedding nanoinclusions to scatter phonons and reduce the thermal conductivity [2].

Despite the good performance, the big issue of the low earth abundance of the constituent materials cannot be overlooked, resulting in endeavours in the search for alternative materials to overcome this issue and enable economic viability for applications at scale. This resulted in the discovery of materials such as SnSe that have received attention due to impressive performance with reports of a single crystal SnSe with ZT = 2.8 at 773 K [21]. The high performance is coupled with the fact that the material is environmentally friendly and cost-efficient. The performance can be attributed due to a narrow band gap and low lattice thermal conductivity. The issue arises with scalability as the single crystal form suffers from challenges such as poor mechanical properties and high production cost [21]. To overcome this, recent research has been focused on optimising the performance of

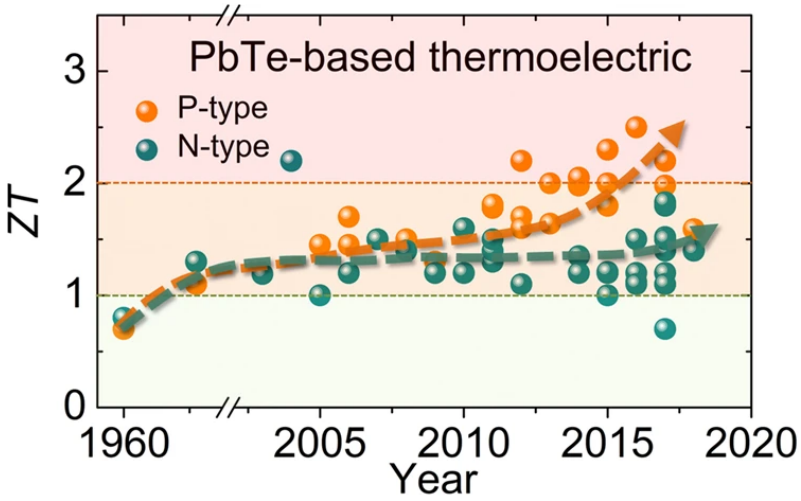

Fig. 1.3 Reported ZT values for PbTe-based thermoelectrics over time for n-type(green ball) and p-type(orange ball) materials. Image taken from Xiao et al. [4] with permission from Springer Nature.

polycrystalline SnSe and investigating alternative fabrication techniques such as aqueous synthesis compared to melting and mechanical alloying which often fail to reproduce performance figures due to variations in material morphology [21].

1.2.2 Half-Heusler Alloys

Half-Heuslers are a promising class of non-toxic, relatively abundant and low-cost thermoelectric materials that align with the criteria in the search for economically viable and environmentally friendly materials to replace the current state-of-art thermoelectrics for operation in the intermediate to high temperature ranges. These factors combined with their good thermoelectric performance allowed half-Heuslers to gain considerable research interest in recent years and they are in fact the key materials studied in this thesis. Half-Heuslers are intermetallic compounds with a chemical formula XYZ where X and Y are usually transition metals or noble metals and Z is a main-group element [22]. The half-Heusler crystal structure consists of three interpenetrating face-centered cubic (fcc) sublattices belonging to the space group $F\bar{4}3m$ with element X at the Wyckoff position 4a (0,0,0), element Y at the position 4c $(\frac{1}{4},\frac{1}{4},\frac{1}{4})$ and element Z at the position 4b $(\frac{1}{2},\frac{1}{2},\frac{1}{2})$. A visual representation in Figure. 1.4 shows the unit cell and primitive cell for the half-Heusler TiNiSn with vacancies present at the Wyckoff position 4d $(\frac{3}{4},\frac{3}{4},\frac{3}{4})$, in contrast to the full-Heusler structure with a chemical formula XY_2Z where the 4d $(\frac{3}{4},\frac{3}{4},\frac{3}{4})$ Wyckoff position is filled by the Y element.

The main advantage in thermoelectric performance stems from the materials' large power factors which are as high as 6 $\mathrm{mWm^{-1}K^{-2}}$ [2]. This is in contrast to their relatively high lattice thermal conductivity of around 3-4 $\mathrm{Wm^{-1}K^{-1}}$ [2] which impedes their thermoelectric performance. However, despite the large κ_l, current research reported maximal ZT values of 1.5 in doped $\mathrm{FeNb_{0.88}Hf_{0.12}Sb}$ and $\mathrm{FeNb_{0.86}Hf_{0.14}Sb}$ at 1200K [23].

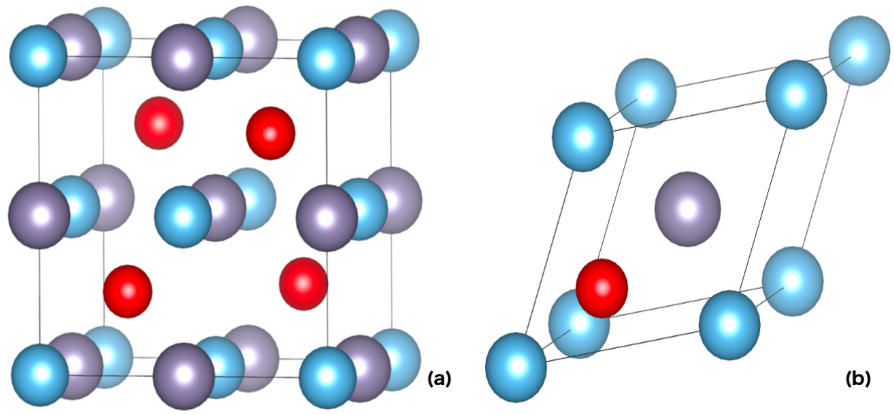

Fig. 1.4 Visual representation of the TiNiSn half-Heusler structure for a) fcc unit cell and b) fcc primitive cell. The colours of the atoms correspond to Ti (blue), Sn(purple), Ni (red). Created using the VESTA package [5]

.

Reducing the lattice conductivity forms the crucial component for optimising performance which rests upon finding new mechanisms to enhance phonon scattering. Methods such as binary or tertiary X-site alloying with heavier elements in order to reduce κ_l through mass-disorder have been investigated [24] and shown to lower thermal conductivity. In addition, unique properties of materials such as TiNiSn to accommodate significant concentrations of interstitial defects ($\sim 10\%$) have led to new opportunities for optimisation and reducing κ_l through further increasing phonon scattering [1]. Attempts at finding novel ways to boost electronic properties have also seen success, with X-site vacancies in NbCoSb shown to reduce the average electron count as to satisfy the 18 electron rule, with the defective system behaving as a semiconductor and displaying good thermoelectric properties, with a ZT value of 0.4 at 973 K [25] in a system that would otherwise be metallic and contain 19 valence electrons. The synthesis route can have significant effects on the material composition, homogeneity due to the introduction of competing binary and Heusler phases and large variations in κ_l and power factors, meaning there is a spread in the resulting thermoelectric properties [2]. This presents difficulty in regards to consistency and reproducibility of performance that need to be addressed.

1.2.3 Other materials

Half-heuslers are just one of several emerging materials being studied for thermoelectric applications. Metal oxides are another promising class of materials particularly for high temperature applications due to their good thermal stability [11]. The challenge for this family of materials is to enhance electrical properties to improve the power factors, which is being attempted via doping [2]. There are also popular mixed anion compound materials, namely oxychalcogenides, which are often arranged in alternating ionic oxide and covalent chalcogenide layers to promote higher electron mobility in the chalcogenide layer and lower κ_l in the oxide layer [26]. The best reported ZT values reached about 1.4 at 923 K

in $Bi_{0.875}Ba_{0.125}OCuSe$ [26]. Skutterides have the chemical formula MX_3, where M is a metallic element and X is a pnictide, based on derivatives of $CoSb_3$. The materials have gathered a lot of interest due to satisfy the conditions of the phonon-glass-electron-crystal (PGEC) concept where the optimal material for thermoelectric applications is described to have thermal properties of a glass and electrical properties of a crystalline material [27]. The thermal conductivity of undoped skutterudites is relatively high, but the redeeming feature lies in the presence of voids in their structure. This has been utilised by filling the voids with weakly bound guest atoms [2], resulting in rattler modes, which are localised vibrational modes that effectively scatter phonons, resulting in large reductions of the thermal conductivity [27]. This rattler behaviour has been observed and exploited in another family of materials called clathrates [2]. Therefore, clathrates often have very low thermal conductivity favourable to good thermoelectric performance. The current challenge lies in the fact that the highest performing Sn-based clathrate thermoelectrics suffer from low thermal stability. One approach that is suggested to alleviate this problem is to investigate mixed Si-Sn clathrates due to Si-based frameworks displaying good thermal stability [28]. Earth abundance is an important aspect of mass-scale production of thermoelectric devices. Hence, Si-Ge alloys have been considered due to the large abundance of Si with RTEG modules being successfully used in deep-space missions by NASA [29]. The Si-Ge alloys have a large κ_l and efforts have been made to lower the κ_l through varying the germanium content, nanostructuring and grain size reduction [2]. Improvements were substantial and ZT values of 1.3 and 0.95 have been achieved for n-type and p-type $Si_{80}Ge_{20}$ bulk nanocomposites [29]. The success in large-scale adaptation of SiGe rests upon good thermoelectric efficiency and lowering material costs due to the high price of Ge [2].

1.3 Methods for optimising thermoelectric performance

There is a broad range of established and emerging thermoelectric materials and whilst many have advantageous properties relating to high performance, they rarely tick all the boxes. This stems from the aforementioned fact that the key thermoelectric properties are often interdependent. Hence, new routes to enhancement attempt to decouple this dependence to improve the electronic properties without impeding the thermal properties and *vice versa*. The final goal is to maximise the power factor and minimise the thermal conductivity and a number of strategies exist, some of which will be outlined in this section.

1.3.1 Structural defects

Intrinsic and extrinsic point defects play a great role in tuning the thermoelectric properties of materials. In the case of intrinsic defects when no chemical impurities are present, defects in the form of interstitials, antisites, and vacancies are often present.

Interstitials occur when a normally unoccupied site is filled, a particular type of interstitial defect called a "Frenkel defect" exists if the unoccupied site is filled due to an atom migrating from its usual site. Antisites occur when a constituent element is in a different site than expected and vacancies occur when there are missing atoms from their otherwise occupied sites [30]. The presence of these defects is material dependent and is influenced by the synthesis process and conditions, especially temperature. Moreover, the addition of extrinsic point defects such as dopants or chemical impurities can aid the formation of intrinsic defects. Point defects are not always isolated and may form larger defect complexes, that can form voids or planar defects creating interfaces and grain boundaries [31].

Alloying/Doping - Alloying can be utilised to increase phonon scattering through the additional disorder in the crystal structure. In the case of TiNiSn, alloying with isovalent elements has been used to induce mass-disorder to lower the thermal conductivity without significantly altering the electronic properties [24]. In addition, TiNiSn can contain up to around 10% of Ni or Cu interstitials with further reductions to the thermal conductivity observed [1]. In the case of Cu interstitials for the TiNiSn, the Cu acts as an n-type dopant that enhances the power factor [1]. We can see that the effect of point defects requires detailed investigations and often combined approaches such as both alloying and doping can be used to extract further improvements of thermoelectric properties.

Phonon-glass-electron-crystal - The concept of a phonon-glass-electron-crystal aims to design semiconductors with crystal structures that have an efficient transmission of charge carriers and poor glass-like thermal properties. In practice, this has been realised by introducing localised vibrational modes in cage-like compounds. Trapping heavy atoms in the cage structure to observe this "rattler" behaviour which has a strong phonon scattering effect [32]. As mentioned in Section. 1.2, this approach has successfully reduced κ_l in skutterudites and clathrates [27, 28] without negatively affecting the electrical transport properties.

Band structure engineering - We have seen that doping can influence the dominant charge carrier type and concentration, depending on the desire of an n-type or p-type semiconductor [31]. This can be taken a step further in band convergence strategies due to the effect of dopants on the energy levels of the system to align electronic bands as to increase valley degeneracy at the conduction band minimum or the valence band maximum. This increases the density-of-states effective mass of either electron or holes [33] and leads to a greater amount of available states around the Fermi level, increasing the Seebeck co-efficient and therefore increasing the thermoelectric performance. [11]. Alternatively, resonant impurity atoms can lead to resonant states, perturbing the density

of states as demonstrated in Tl:PbTe [34].

Grain boundaries - The additional scattering of phonons at grain boundaries is an important factor in enhancing thermoelectric performance and reducing thermal conductivity. Tuning and understanding the size and morphology of grain boundaries is challenging and both a macroscale and nanoscale approach is often required [35]. Dense dislocation arrays at low-energy grain boundaries in $Bi_{0.5}Sb_{1.5}Te_3$ were shown successfully scatter mid-frequency phonons to significantly reduce the thermal conductivity and improve the ZT to 1.86 at 320K. The large improvements were possible as the additional scattering of phonons did not have a large impact on the electrical conductivity [36].

1.3.2 Dimensionality reduction and nanostructuring

In bulk 3D crystalline systems the key thermoelectric properties S, σ and κ are often interdependent, making them difficult to modify. However, by reducing the system size to form 2D quantum wells, 1D quantum wires or 0D quantum dots leads to changes to the electronic density of states and introduces quantum-confinement effects as the size of the material in any direction becomes comparable to the wavelength of the charge carriers [11]. This can be used to alter the DOS near the Fermi level to enhance the Seebeck co-efficient [2]. The introduction of new physical phenomena opens new opportunities to decouple the dependence of key thermoelectric properties and enhance them separately [37]. Moreover, low-dimensionality results in a large number of interfaces that can effectively scatter phonons that significantly contribute to κ_l. Experiments on 2D superlattices of Bi_2Te_3 and Sb_2Te_3 have found that the reduction in κ_l was more significant than the change to the electrical conductivity [37]. The enhancements to the power factor and κ_l both contribute to improvements in ZT. However, in practice, it was found that the enhancement to the power factor is not as effective at improving the ZT value and thermoelectric performance as the reduction of κ_l [2].

Nanostructuring of thermoelectric materials has successfully been shown to enhance thermoelectric performance by embedding nanoinclusions into the semiconducting matrix of a host bulk material. After embedding of SrTe nanocrystals into a bulk PbTe matrix, strong phonon scattering was observed without impeding the hole mobility, allowing to achieve a ZT value of 2.2 for this p-type thermoelectric material [38]. Improvement of the thermometric figure of merit using this approach has been seen in a number of other nanocomposites from Bi_2Te_3 [39], SiGe [40] and In_2O_3 [41] based compositions. The phonon mean free path determines the distance between scattering events of phonons which cumulatively contribute to the thermal conductivity. Hence, by incorporating various nanostructures that span a wider length scale, phonons with a broad range mean free paths can be selectively scattered to lower the thermal conductivity [42]. These nanocomposites can usually be fabricated using spark plasma sintering (SPS), ball milling, hot pressing.

However, the preparation conditions are important for reproducibility of performance [43] and manufacturing processes for nanostructuring materials can be challenging.

1.4 Modelling Thermoelectric Properties

The continuous search for new strategies and mechanisms for improving thermoelectric performance through experimental methods has shown a lot of success, but the broad range of candidate materials and complex material compositions makes experimental efforts difficult, costly, and time-consuming. This often results in limited ability to search for new materials and often finds materials with poor performance. On the other hand, access to high-performance computing is improving and continuous developments in materials modelling techniques are being made. This places great importance on theoretical modelling as it can aid experimental research in regard to material selection. Initial high-throughput screening of a large number of materials to test for phase stability and estimate ZT values can be used to efficiently compile a list of promising candidate thermoelectric materials [44]. Moreover, first-principles calculations can be used to compute all of the necessary components in determining the electronic and thermal transport properties to investigate the thermoelectric performance of materials and gain an additional understanding of the underlying mechanisms for their optimisation. To determine electron transport properties code implementations to solve the semi-classical Boltzmann transport equation have been written. Although, calculations of electron transport are not undertaken in this work, the currently available codes to do this include BoltzTraP [45], BoltzTraP2 [46] and BoltzWann [47]. On the other hand, we do compute thermal transport properties by solving the phonon Boltzmann transport equation with the aid of the ShengBTE package [48]. Other codes such as almaBTE [49], phono3py [50] are also capable of solving the phonon BTE. Solving the phonon BTE comes at a large computational cost as phonon density of states, second-order and third-order force constants need to be computed using DFT codes to provide the necessary input. This may be computed using the many available DFT packages such as CASTEP [51], Quantum Espresso [52], VASP [53] and others. However, it should be noted that not all DFT codes are supported by the BTE solver packages. In addition, we also compute κ_l using an alternative theoretical model in the form of the modified Debye-Callaway model with the help of the mDCThermalC code [54]. Here, the required input requires computing the phonon dispersion, phonon velocities, and mode parameters, which can be obtained using packages such as CASTEP [51] and Phonopy [55].

1.5 Thesis Structure

Real-world applications of thermoelectrics and their capabilities as an energy recovery technology have been discussed. A mention of the state-of-the-art thermoelectric materials

and promising candidates have been outlined, particularly half-Heusler alloys which are the focus of this work. Potential methods for optimising thermoelectric performance have been described. Theoretical and computational frameworks allowing for modelling of the relevant material properties and optimisation mechanisms investigated in this thesis were presented. A summary of the thesis structure can be found below.

Chapter 1 : Introduction - This chapter introduces the field of thermoelectrics and its real-world applications. An overview of state-of-the-art and promising thermoelectric materials is presented. In addition, key optimisation techniques to enhance performance and the computational tools available to model and predict material properties are described.

Chapter 2 : Theory - The theory chapter includes the key theoretical framework to provide an understanding of the thermoelectric effect, first principles simulations, bandstructure theory, lattice dynamics, and thermal transport.

Chapter 3 : Methodology - In Chapter 3, the methods used to perform the first principles calculations are described in detail. The computer programs used are noted and appropriate procedure for testing and convergence of the calculations is described, including the choice of computational parameters. Details of inelastic neutron scattering experiments and experimental parameters are also provided. This will ensure that the investigations contained in this thesis can be repeated if one wishes to do so.

Chapter 4 : Computing lattice thermal conductivity of defective supercells - This chapter investigates XNiSn (X= Ti, Zr, Hf) based half-Heusler compositions, which have shown promising performance as n-type thermoelectric materials. However, the stoichiometric materials suffer from a relatively high lattice thermal conductivity. Therefore, an investigation of the effect of interstitial Ni and Cu defects on the vibrational properties and κ_l are investigated. A homogeneous and clustered Ni defect model is used to describe the vibrational properties, this required using supercells to capture the desired ordering of interstitials. The neutron weighted phonon density of states is computed to enable a direct comparison against results from inelastic neutron scattering experiments for compositions with comparable interstitial content. Lastly, the lattice thermal conductivity is computed for TiNiSn and $TiNi_{1.125}Sn$ through solving both the phonon Boltzmann Transport equation and the modified Debye-Callaway model.

Chapter 5 : Electronic properties of XNiSn (X = Ti, Zr, Hf) with interstitial defects - The electronic structure properties of parent TiNiSn, ZrNiSn and HfNiSn and chosen defective supercells containing Ni or Cu interstitials are computed. Due to the use of supercells, band folding is present and a method for computing the effective bandstructures is implemented. The previous chapter investigated the role of Ni and Cu interstitials on vibrational properties. However, thermoelectric properties are often interdependent and this chapter aims to understand the consequences and differences of Ni and Cu interstitials on the electrical properties. A mismatch between a computationally predicted metallic state and experimentally observed semiconducting behaviour is found.

Charged calculations through removal of electrons are performed to determine the level of charge compensation that may be present. The Hubbard U model and meta-GGA treatment of the exchange and correlation are used to investigate localisation effects. Finally, effective electron masses are calculated using the parabolic band approximation.
Chapter 6 : Electronic structure properties of $Nb_{1-x}CoSb_ySn_{1-y}$ - In the final results chapter, the effects on the electronic structure properties of $Nb_{1-x}CoSb_ySn_{1-y}$ due to X-site vacancy and doping are investigated. Calculations are performed with and without Sn doping, with a defect concentration targeted to reduce the average number of valance electrons from the expected 19 in stoichiometric NbCoSb to satisfy the 18 electron rule, which is often used as a predictor of semiconducting behaviour. The disagreement of experimental lattice parameters with previous simulations of stoichiometric NbCoSb is explored. In addition, to tackle the main focus of the chapter, calculations of the electronic band structures and effective electron masses are performed to provide insight into the properties of defective compositions and to spot potential mechanisms for optimisation.
Chapter 7 : Conclusions - The final chapter provides a summary of the results and findings of the investigations found in this work. Suggestions for future research directions and computational methods for modelling thermoelectric properties are discussed.
Appendix A : - Comparison of INS phonon DOS obtained using the MARI instrument for XNiSn (X = Ti, Zr, Hf) based compositions to display the effects of binary and ternary X-site substitution.

Chapter 2

Theory

2.1 Thermoelectric effect

2.1.1 Seebeck effect

The thermoelectric effect has three manifestations in the form of the Seebeck, Peltier and Thomson effect. The first to be discovered was the Seebeck effect in the year 1821 when T. J. Seebeck managed to produce a voltage difference across a junction when two dissimilar materials were joined together in the presence of a thermal gradient [56]. This occurs as the mobile charge carriers diffuse towards the cold side of the junction, which creates a potential difference and thus an electrical current between the junctions in a closed circuit. The concentration of electrons follows the Fermi distribution around the Fermi energy and is temperature dependent, resulting in a larger number of electrons above the Fermi energy at the hot end of the material and the electrons will transport energy to the cold end to equilibrate the system. If the temperature difference is maintained, the charge must build up generating a thermovoltage. A possible set-up to produce this effect can be seen in Fig 2.1. This proportionality between the voltage difference and temperature is an intrinsic property, called the Seebeck coefficient, also known as the thermopower, which represents the proportionality of the voltage difference due to the temperature difference. It can be defined as [57]:

$$S = -\frac{\triangle V}{\triangle T} = -\frac{V_{hot} - V_{cold}}{T_{hot} - T_{cold}}, \tag{2.1}$$

where S is the Seebeck co-efficient, $\triangle V$ represents the voltage difference and $\triangle T$ corresponds to the temperature difference between the hot and cold sides of the junction. The thermopower is measured in the units of V/K and is small in metallic systems (few $\mu V/K$) and much larger in semiconductors (few hundred $\mu V/K$) [56]. This study focuses on exploiting this effect for the purpose of waste heat harvesting. Finding an n-type and p-type semiconducting material pair with a high Seebeck coefficient is one of the key components in optimising the performance of a thermoelectric generator device. The sign

of the voltage reveals if the material is n-type or p-type as a result of either negative or positive charge carriers being responsible for the Seebeck effect.

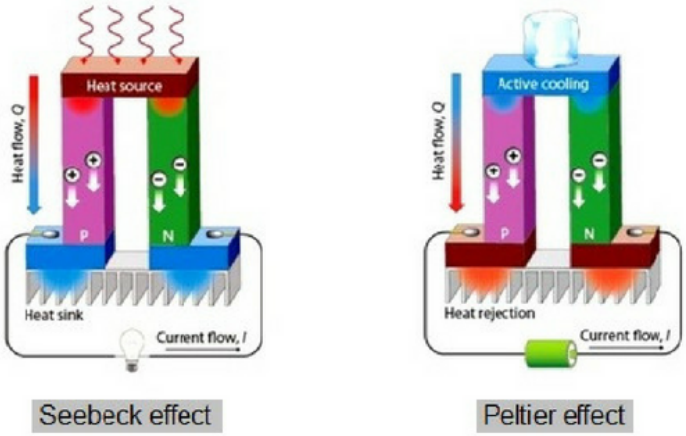

Fig. 2.1 A thermoelectric circuit for a thermoelectric generator (left) and a thermoelectric refrigerator (right). The white arrows represent the diffusion direction of the charge carriers in the n-type and p-type semiconductors respectively. Image taken from [6].

2.1.2 Peltier and Thomson Effect

A related manifestation of the thermoelectric effect was discovered a few years later. This is known as the Peltier effect, which occurs when a current I is passed through a junction of two dissimilar materials to either absorb or expel heat at a junction. [11]. Heat will be absorbed or rejected at the junction dependent on the type of charge carrier diffusing when an electric current is applied. When an electric field is applied through the material at constant temperature the electric current density of the electrons, $\mathbf{j}_q$ can be expressed as [58]:

$$\mathbf{j}_q = ne\mu_e E, \tag{2.2}$$

where n is the electron concentration, e is the electron charge, μ_e is the electron mobility and E is the electric voltage. The corresponding energy flux can then be written as [58]:

$$\mathbf{j}_U = n(E_c - \mu + \tfrac{3}{2}k_B T) - \mu_e E, \tag{2.3}$$

here μ refers to the Fermi energy and E_c is the energy at the conduction band edge [58]. The Peltier co-efficient relationship can then be written as $\mathbf{j}_U = \Pi j_q$ for electrons. In the case of holes, a similar relationships can be found [58]:

$$\begin{aligned} \mathbf{j}_q &= pe\mu_h E \\ \mathbf{j}_U &= p(\mu - E_v + \tfrac{3}{2}k_B T) - \mu_h E, \end{aligned} \tag{2.4}$$

where p is the hole concentration, E_v is the energy of the valance band edge and μ_h is the hole mobility. It should be noted that the Fermi level has to be recomputed in the case of doped semiconductors, where donor and acceptor levels in the band gap have to be considered. This can be calculated by assuming the charge neutrality condition, which states that the sum of the positive charges is equal to the sum of the negative charges. The amount of Peltier heat generated or absorbed per unit time is given using the following relationship [58]:

$$Q = (\Pi_A - \Pi_B)I, \tag{2.5}$$

where Q is the produced or absorbed heat, Π_A and Π_B are the Peltier coefficient's of conductor A and B and I is the electric current between the conductors. This is not the total rate of heat generated as other effects, such as Joule heating are not taken into account. The Peltier effect is often used to create thermoelectric heat pumps and thermoelectric coolers.

Finally, we arrive at the last thermoelectric effect, namely the Thomson effect. This provides an extension to the Seebeck and Peltier effects and concerns only one conductor. If the conductor is subject to a thermal gradient along it's length from an external heat source an electrical current will be generated and *vice versa* when an electrical current is passed across the material a thermal gradient will be present.

2.1.3 Quantifying thermoelectric performance

For a device to function effectively a large enough thermal gradient is required to generate electricity. To achieve good performance, the materials used generally need to be doped semiconductors and are usually designed in an n-type and p-type material arrangement, a schematic of this can be seen in Figure 2.1.

When assessing the thermoelectric performance of a material, the efficiency can be determined through a dimensionless figure of merit called the ZT value, given by [57],

$$ZT = \frac{S^2 \sigma T}{\kappa_e + \kappa_{lat}}, \tag{2.6}$$

where S is the Seebeck coefficient, σ is the electrical conductivity, with $S^2\sigma$ being the power factor. Whereas κ_e and κ_{lat} are the electronic and lattice thermal conductivity respectively. The higher the ZT value the better the efficiency, but ultimately the average ZT across the operating temperature range is the most important in devices. The parameters involved are interdependent and therefore obtaining a good ZT value becomes an optimisation problem dependent highly on the underlying crystal structure, with an aim to reduce the lattice thermal conductivity whilst maintaining a high power factor. The equation for maximum thermoelectric efficiency, η_{max} can be written as [11]:

$$\eta_{max} = \frac{T_H - T_C}{T_H} \frac{\sqrt{1+z\bar{T}} - 1}{\sqrt{1+z\bar{T}} + \frac{T_C}{T_H}} \tag{2.7}$$

with $\bar{T}$, T_H and T_C corresponding to the average temperature, hot side temperature and cold side temperature respectively. Here, we can see that optimising the ZT value is crucial to obtaining good efficiency. Looking at Equation. 2.6 we can see that increasing the power factor will not improve efficiency if the electronic and lattice thermal conductivity terms seen in Equation. 2.6 remain large. Semiconductors have the ability to become good thermoelectric materials as the carrier concentration can be controlled through doping to optimise the power factor. The optimisation problem is further complicated as increasing doping concentration leads to an increase in κ_e with their relationship described through the Wiedemann-Franz law[57]:

$$LT = \frac{\kappa_e}{\sigma}, \tag{2.8}$$

where L is the Lorenz factor, which is a constant. This means that the key remaining component for the optimisation of ZT and thermoelectric efficiency lies in reducing the lattice component of the thermal conductivity, κ_{lat} and is one of the focal points of this work.

2.2 Density Functional Theory

Modelling atomic interactions exists in the realm of quantum mechanics. This means that if we were to attempt to gain insight into the material properties, we would need to solve the many-body Schrödinger equation [59]. The time independent equation is given by,

$$\hat{H}\Psi(\mathbf{r}_i, \mathbf{R}_A) = E\Psi(\mathbf{r}_i, \mathbf{R}_A), \tag{2.9}$$

where E is the total ground state energy, $\hat{H}$ is the Hamiltonian operator and Ψ is the full many-body wavefunction with the electron and nuclear co-ordinates $\mathbf{r}_i$ and $\mathbf{R}_A$ for an electron i and nucleus A. However, upon adding atoms to the system, the complexity of this approach scales with dimensions of $3n_{electrons} + 3N_{atoms}$ and quickly becomes prohibitively expensive to compute. However, a range of approximations has been utilised in order to access ground state solutions. In this chapter, we will see how this can be achieved through the use of density functional theory (DFT), which allows us to overcome this computational complexity to an extent that simulating systems containing hundreds or even thousands of atoms is now possible.

2.2.1 Born-Oppenheimer Approximation

The Born-Oppenheimer Approximation, also known as the adiabatic approximation is one of the principal approximations made in quantum chemistry. It springs from the fact that

in most cases the nuclei are relatively heavier and move much slower than the electrons. Hence, the nuclei can be assumed to be fixed in space with electrons moving within a field around them. This of course requires many corrections and breaks down when the nuclei have a lot of kinetic energy or when the ground state energy of the nuclear motion is comparable to the size of the band gap [60]. This allows the many-body Hamiltonian to be written as the electronic Hamiltonian, describing the motion of N electrons in a field of point charges and the electronic Hamiltonian then takes the following form [60],

$$\hat{H}_e = -\sum_{i=1}^{N} \frac{1}{2} \bigtriangledown_i^2 - \sum_{i=1}^{N} \sum_{A=1}^{M} \frac{Z_A}{\mathbf{r}_{iA}} + \sum_{i=1}^{N} \sum_{j>i}^{N} \frac{1}{r_{ij}}, \tag{2.10}$$

where the first term describes the operator for the kinetic energy of electrons, the second term describes the operator for the Coulomb interaction between the electron i and the atomic number of nucleus A. Finally, the third term represents the electron-electron repulsion between electrons i and j.
The solutions can then simply be found using [60],

$$\hat{H}_e \Psi_e = E_e \Psi_e, \tag{2.11}$$

With the electronic wave-function Ψ_e being dependent explicitly on the electronic co-ordinates and only parametrically on the nuclear co-ordinates,

$$\Psi_e = \Psi_e(\mathbf{r}_i; \mathbf{R}_A), \tag{2.12}$$

Similarly, reversing the argument and treating the electronic co-ordinates as their average values over the wave function we can find the Hamiltonian describing the motion of nuclei. In conclusion, this provides the scope for the development of the Hamiltonian in DFT, which will be described in the following section.

2.2.2 Hohengberg-Kohn Theorems

One of the main quests in developing the theory is to look for an easier solution to the many electron wavefunction. More specifically the electron density. The main foundation and success of DFT rest on the first and second Hohenberg-Kohn theorems, which were published in 1964 [61].

First Hohenberg-Kohn theorem

To begin with, the first theorem provides the model that will allow the electron density to uniquely describe the Hamiltonian, due to the one-to-one mapping of the electron-nuclear potential, only varying by a constant [61]. The proof begins from writing the Hamiltonian in the form:

$$\hat{H} = \hat{T} + \hat{V}_{ee} + \hat{V}_{ext}, \tag{2.13}$$

where $\hat{T}$ is the kinetic energy operator, $\hat{V}_{ee}$ is the electron interaction operator and $\hat{V}_{ext}$ is the external potential. After writing the Hamiltonian we attempt a proof by *reductio ad absurdum* in the following way:

1. Assume two different external potentials can give rise to the same ground state density,
2. Use the ground state and a trial wave function,
3. Apply the variational principle.

The ability to use the trial function comes from the non-unique description of the density, meaning that two different ground state wavefunctions Ψ_1 and Ψ_2 and their associated Hamiltonians $\hat{H}_1$ and $\hat{H}_2$ both give the groundstate density $n_0(\mathbf{r})$. Therefore we can now write [61]:

$$\begin{aligned} E_1^0 < \langle \Psi_2 | \hat{H}_2 | \Psi_2 \rangle &= \langle \Psi_2 | \hat{H}_2 | \Psi_2 \rangle + \langle \Psi_2 | \hat{H}_1 - \hat{H}_2 | \Psi_2 \rangle \\ &= E_2^0 + \int n_0(\mathbf{r})[v_{ext,1}(\mathbf{r}) - v_{ext,2}(\mathbf{r})]d\mathbf{r}, \end{aligned} \tag{2.14}$$

where E_1^0 and E_2^0 are the resulting groundstate energies. Reversing the above calculation for the ground state energy of the trial wave function, it can be shown that there is a contradiction:

$$E_1^0 + E_2^0 < E_2^0 + E_1^0 \tag{2.15}$$

As a result we can conclude that the ground state density specifies the electron-nuclear potential uniquely.

Second Hohenberg-Kohn Theorem

Leading on from the first theorem, the energy can now be found for all N-electron densities and be written as a functional of the density n(**r**) [61]:

$$E[n] = T[n] + V_{ee}[n] + V_{en}[n] \tag{2.16}$$

$$= F[n] + \int n(\mathbf{r}) v_{ext}(\mathbf{r}) d\mathbf{r}, \tag{2.17}$$

where F[n] is a universal functional of the density. Hence, if we know the true groundstate density then E[n] is equal to the groundstate energy [61]. On the other hand, the next statement shows that for any trial density $\tilde{n}(\mathbf{r})$, the energy evaluated for that particular density will satisfy the following relation:

$$E[n(\mathbf{r})] \leq E[\tilde{n}(\mathbf{r})], \tag{2.18}$$

a minimisation procedure must be performed in order to find the ground state if $\tilde{n}(\mathbf{r}) \neq n(\mathbf{r})$. However, searching for all densities in large systems, even of a few electrons becomes impractical. Moreover, there is no access to all possible wave functions, so DFT is an approximate functional approach rather than a wave function approach [62]. Thus, requiring a computationally practical approach, leading to the Kohn-Sham method, which is outlined in the next section.

2.2.3 Kohn-Sham Theory

There was quite a lot of scepticism from the practical aspects of real calculations after the introduction of the Hohenberg-Kohn theorems due to the fact that even though the ground-state energy functional could be written as a functional of the density, this was not the case for the $T[n]$ or $V_{ee}[n]$ functionals [63]. Kohn and Sham realised the Kinetic energy(K.E) has to be calculated more efficiently and their idea was to write the exact K.E for a non-interacting system, but use the density of the real system instead. This leads to coupled single particle equations that depend on the density alone and takes the form of [63]:

$$E_i\Psi_i(\mathbf{r}) = (-\frac{1}{2}\bigtriangledown^2 + V_H[n(\mathbf{r})] + V_{XC}[n(\mathbf{r})] + V_{ext}[n(\mathbf{r})])\Psi_i(\mathbf{r}), \tag{2.19}$$

with E_i and $\Psi_i(\mathbf{r})$ being the energy and wavefunction of electron i and $n(\mathbf{r})$ is the density, given as:

$$n(\mathbf{r}) = \sum_{i=1}^{N}\sum_{s}|\psi_i^s(\mathbf{r})|^2, \tag{2.20}$$

where N represents the number of electron orbitals and s represents the electron spin. $\psi_i^s(\mathbf{r})$ is in general a two component spinor, which is able to describe collinear magnetic states. This can have a significant effect on the electron energy levels and should be considered to model magnetism. In the case of a known non-magnetic system, the spin up and spin down components of $\psi_i^s(\mathbf{r})$ are equal and need not be treated separately in a calculation. The right side of the Equation 2.19 describes the functionals for the kinetic energy, Hartree potential, exchange and correlation potential and the external potential respectively. However, the form of the Hartree functional introduces a self-interaction error, which is the residual error of an electron interacting with itself due to the approximate nature of the exchange-correlation functional [64]. The functional form of which is:

$$V_H[n(\mathbf{r})] = \int \frac{n(\mathbf{r}')}{|\mathbf{r}-\mathbf{r}'|}d\mathbf{r}' \tag{2.21}$$

to remedy this the error is swept onto exchange-correlation functional E_{XC}, which contains all of the unknown contributions to the energy arising from non-classical effects and to some extent the K.E, as clearly the non-interacting system will not have the same exact

value as that of an interacting one [62]. Although this is theoretically an exact form for the solution, due to the fact E_{XC} is unknown the output will still be approximate.

2.2.4 Bloch's Theorem

The Kohn-Sham scheme allows to exactly write the many-body problem for electrons as a set of single electron equations. The set of wavefunctions that minimises the total energy can be found self-consistently. In practice, this is usually done by placing the atoms at some specified coordinates and generating the potential for the nuclei. Then a guess has to be made for the density, which will either be the density of a homogeneous electron gas, a randomly assigned density, or a density chosen using another starting density model. At this point, the density can be used to solve the Kohn-Sham equations and solve for the energy. From here there is now a new set of wavefunctions from which the density can be re-computed. If at this point the energy the self-consistent energy is identical for both the trial density and output density then the ground state has been found. However, if this is not the case then the process is repeated until the change in energy reaches convergence within the user specified tolerance criteria. This would require computing an infinite number of electrons and an infinite number of wavefunctions. To overcome this problem and enable calculations at a reasonable computational cost, we can often utilise the periodicity of the system, allowing simulation cells to contain hundreds of atoms with the help of Bloch's theorem. The theorem enables to write the electronic wavefunction as two components, the wave-like component and a periodic function which has the periodicity of the simulation cell[63]:

$$\Psi(r)_{i,\mathbf{k}} = exp(-i\mathbf{k}.\mathbf{r})\phi_{j,\mathbf{k}}(r), \tag{2.22}$$

where the periodic function $\phi(r)$ is described by a discrete set of plane waves, $\mathbf{k}$ is a wavevector within the first Brillouin zone and j is the band index.
In CASTEP [51] the periodic functions of choice are plane waves. A plane wave can be written as,

$$\Psi_{j,\mathbf{k}} = \sum_{G} C_{j,\mathbf{k},\mathbf{G}} \exp^{-i\mathbf{G}.\mathbf{r}}, \tag{2.23}$$

where $\mathbf{G}$ is the reciprocal lattice vector and satisfies the condition $\mathbf{G}.\mathbf{a} = 2\pi m$ with $\mathbf{a}$ being a lattice vector and m is an integer. $C_{j,\mathbf{k},\mathbf{G}}$ are the plane wave coefficients, which form the basis set. This discrete and periodic nature makes this form suitable for deploying the fast Fourier transform method to speed up diagonalisation of the eigenvalue equation in computer simulations and allows the calculations to be much more cost efficient. This is a key advantage of plane wave basis set over alternatives such as the Gaussian basis set as the wave function remains periodic in reciprocal space [65].

2.2.5 Exchange and Correlation

The contribution of the E_{XC} has to be further developed as trying calculations without it would generally lead to meaningless results. The general form of the exchange and correlation functional is:

$$V_{XC} = \frac{\partial E_{XC}}{\partial n(\mathbf{r})} \tag{2.24}$$

where E_{XC} is the total exchange and correlation energy. The exchange component of this energy originates from the already mentioned self-interaction term due to the Hartree energy and also due to the fermionic nature of the electrons, which requires that we satisfy the Pauli exclusion principle. On the other hand, the correlation energy encompasses the difference between the assumed non-interacting system and the true interacting system [66]. Various exchange-correlation functionals have been developed and many performing calculations to a high degree of accuracy. Throughout the calculations in my investigation, I have predominantly used the Perdew-Burke-Ernzerhof(PBE) E_{XC} functional, which is known to give good results and is commonly used [67].

When enhancing the accuracy with exchange-correlation functionals, these days there are complex methods, starting from the local density approximation (LDA). However, the LDA is regarded as inaccurate for atomization energies in highly interacting systems. However, it builds a foundation for the PBE functional.

In the scheme of the LDA approximation, the contribution of this exchange correlation functional to the energy at a particular point in space depends only on the density at that point [66].

$$E_{XC}[n] = \int n(\mathbf{r}) \varepsilon_{XC}^{LDA}(n(\mathbf{r})) d\mathbf{r} \tag{2.25}$$

After obtaining this, the exchange and correlation components are usually separated according to their respective density components. In LDA the exchange functional is given by [66]:

$$E_X^{LDA}[n] = -\frac{3}{4}\left(\frac{3}{\pi}\right)^{1/3} \int n(\mathbf{r})^{4/3} d\mathbf{r}, \tag{2.26}$$

and the correlation component is parametrised using quantum Monte-Carlo energy calculations as a function of the density of a homogeneous free electron gas, under a chosen interpolation scheme[68].

However, the LDA approximation tends to underestimate the bond lengths, and in order to make up for this issue, the next step is to make the exchange-correlation density dependent on both the electron density and the gradient, where the gradient can better account for local inhomogeneities[69]. This leads to the topic of the PBE exchange-correlation generalised-gradient-approximation (GGA) functional.

$$E_{xc}[n(\mathbf{r})] = \int (\mathbf{r})\varepsilon_{xc}^{GGA}(n(\mathbf{r}), n(\mathbf{r}), \bigtriangledown n(\mathbf{r}), \bigtriangledown n(\mathbf{r}))d\mathbf{r} \tag{2.27}$$

The exchange-correlation density can be split into the exchange and correlation components as before. Which is simply:

$$\varepsilon_{xc}^{GGA}(n(\mathbf{r}), \bigtriangledown n(\mathbf{r})) = \varepsilon_{x}^{GGA}(n(\mathbf{r}), \bigtriangledown n(\mathbf{r})) + \varepsilon_{c}^{GGA}(n(\mathbf{r}), \bigtriangledown n(\mathbf{r})) \tag{2.28}$$

in the case of a spin-polarized case, the exchange-correlation also depends on the spin up and spin down components of the spin density, $n^{\uparrow}$ and $n^{\downarrow}$ respectively, forming the local spin density approximation (LSDA) and can be extended to GGA's through a dependence on the spin up and spin down components of the spin density as well as their gradients [14].

The way the LDA exchange density is improved is through applying an enhancement factor that is a function of the reduced density gradient [70].

$$E_{x}^{GGA}[\rho] = (\mathbf{r})\varepsilon_{x}^{LDA}(\rho(r))F_{x}(s)dr, \tag{2.29}$$

where the reduced density is a dimensionless parameter of the following form:

$$s(r) = \frac{|\bigtriangledown \rho(r)|}{2(3\pi^2)^{\frac{1}{3}}\rho^{\frac{4}{3}}(r)} \tag{2.30}$$

and the PBE functional has the enhancement factor, which takes the form:

$$F_{x}^{PBE}(s) = 1 + \kappa - \frac{\kappa}{1 - \mu s^2/\kappa}, \tag{2.31}$$

where κ has the value of 0.804 [70].

There are ways to go further beyond and develop hybrid exchange functionals. These use a mixture of the Hartree-Fock exchange term and the general gradient approximation exchange described in the above equations. These may perform better for particular calculations, but for many systems and properties of interest PBE provides good performance.

2.2.6 DFT+U

The accuracy of computing electronic structure properties using approximate DFT functionals, such as LDA or PBE is system specific and often depends on properties that one wishes to study. Although the LDA and PBE functionals perform well in many cases, they often excessively delocalise electrons due to the self-interaction error of partially occupied Kohn-Sham orbitals and favour metallic ground states [71], particularly in strongly correlated systems. In order to tackle this issue whilst minimising additional computational expense, a simple formalism called DFT+U has been proposed, which aims to apply a "+U" correction based on the Hubbard model [72] in order to improve the description and predictive power of correlated systems. The general formulation of the method consists of

applying this correction to specified localised orbitals (usually d or f orbitals) and a regular treatment of the valence electrons according to the formulation of the chosen functional, this can be written as:

$$E_{DFT+U} = E_{DFT} + E_{Hub} - E_{dc} = E_{DFT} + E_U \tag{2.32}$$

where E_{DFT} is the approximate DFT total energy, E_{Hub} is the Hubbard Hamiltonian term and E_{dc} includes the double counting term, to remove the interaction energy modelled by the Hubbard term from the DFT functional [71]. The final term E_U, is simply the grouping of the Hubbard interaction and double counting term. This E_U term is often simplified for practical implementation purposes as:

$$E_U = \frac{U^l}{2} \sum_a Tr[\mathbf{n}^{l\sigma}(1 = \mathbf{n}^{l\sigma})] \tag{2.33}$$

where U^l is the effective U parameter at an atomic site l and $\mathbf{n}^{i\sigma}$ is the atomic orbital occupation number for site l with spin σ. Approximate DFT functionals produce an unphysical non-linear total energy curve with respect to the number of electrons for orbitals with fractional occupation. The Hubbard correction encourages Mott localisation on atomic sites, reducing the tendency for partial occupation. Therefore, the U correction aims to compensate for this discrepancy. The effect of the Hubbard U correction, though the increased accuracy in describing the electron interactions can lead to recreating insulating behaviour and size of the band gap for systems which would've otherwise been predicted as metallic. In addition, this approach can also improve the description of structural and magnetic properties of strongly correlated systems. However, the value of U must be re-computed for each system under investigation or particular implementation of the method and not treated as a means to reach agreement with experiment [71].

2.2.7 Pseudopotentials

The purpose of a DFT calculation is to extract an accurate set of properties of interest. Modelling core electrons entails short wavelength oscillations, meaning large Fourier components and therefore a high cut-off energy. The cut-off energy is a parameter that determines the size of the basis set and is described in more detail in Section 3.1.3. However, the core electrons are shielded by the valence electrons and are largely unperturbed by the chemical environment. It is the valence electrons that play a role in the bonding. This allows us to replace a strong ionic potential with a pseudopotential. The design of a pseudopotential focuses on replicating the valence electron wavefunctions exactly outside of the core region $r > r_c$, but to vary smoothly within the core region as seen in Figure 2.2. Allowing to remove the nodes in the core region, meaning the wave functions can now be represented by a much smaller number of plane waves [7]. Moreover, pseudopotentials can include relativistic effects for the core electrons if they are non-negligible.

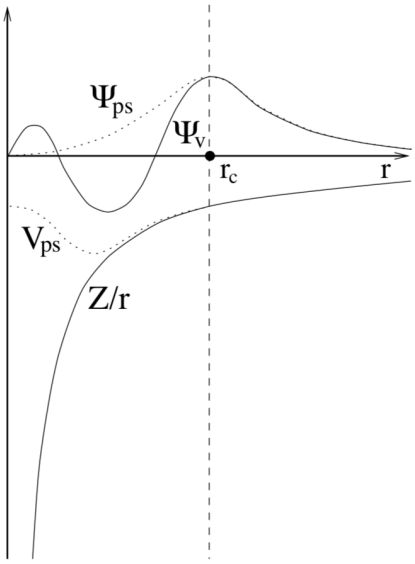

Fig. 2.2 An all electron wavefunction Ψ_V, ionic potential Z/r (solid lines), pseudopotential wavefunction $\Psi_p s$ and pseudopotential V_{ps} (dashed lines). Image taken from [7].

It should be noted, that a non-local pseudopotential is usually required to achieve accuracy in modelling the behaviour of elements. The general form of such an operator can be written as [7]:

$$V_{PS} = \sum_{l,m} |Y_{lm} > V_l(\mathbf{r}) < Y_{lm}| \tag{2.34}$$

where $|Y_{lm} >$ are spherical harmonics and V_l is the pseudopotential for angular momentum l. The pseudopotentials are constructed to accurately reproduce the properties of an all-electron atom. DFT calculations of different atomic configurations of isolated spherically symmetric atoms are used to perform the fitting [73]. If the isolated pseudoatom manages to reproduce the properties of the single atom in any chemical environment then the pseudopotential is said to be transferable.

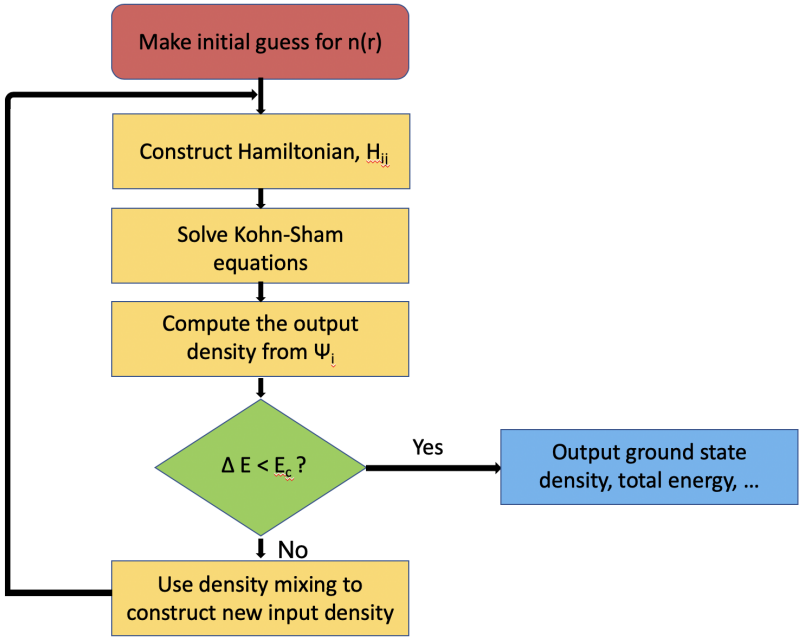

Fig. 2.3 Flowchart describing the self-consistent loop for computing the ground state density and total energy.

Putting everything together we can now self-consistently solve the Kohn-Sham equations. The procedure for doing so can be seen in the flowchart in Figure 2.3. Where the self-consistent loop will keep updating the electron density until the change in energy is smaller than the user specified convergence tolerance E_c.

2.3 Electronic Structure

2.3.1 Band Theory

Solving the Kohn-Sham equations allows us to obtain information about the allowed energy levels of the system at a particular **k**-point within the Brillouin zone. This gives us the ability to define the dispersion relation E(**k**), for a chosen set of **k**-points. The variation of each energy level can be plotted along a path formed by the set of **k**-points, often chosen to be along the high symmetry directions within the BZ, forming bands. This gives a visual representation of the nature of the dispersion and often provides great insight into the material properties. one key feature that can be determined is the presence and size of a band gap in a semiconductor. If there are no allowed states between the top of the valence band and the bottom of the conduction band, semi-conducting or insulating behaviour will be observed. The distinction can be made by quantifying the size of the band gap. For a material to be semi-conducting this band gap has to be small, to allow thermal excitation of electrons to the conduction band, allowing for conduction of electrons to occur, if the band gap is too large the material will act as an insulator. On the other hand, if the valance and conduction bands cross, the electrons can freely move between the bands, and the material

is classified as a metal. In addition, the band gaps can be further categorised into direct band gaps, where the position of the VBM and CBM occurs at the same **k**-point in the Brillouin zone or indirect band gaps, when the position of the VBM and CBM are found at a different **k**-point, requiring additional momentum for photon emission. This additional momentum is usually transferred via phonons. When designing semi-conducting devices, optimising the electronic properties plays a crucial role. Quantifying the magnitude of the dispersion gives insight into the nature of the charge carriers, with highly dispersive or flat dispersion-less bands suggesting delocalised or localised states respectively. Moreover, thermoelectric properties, such as the Seebeck coefficient can be approximated, with localised bands, leading to higher Seebeck coefficients.

2.3.2 Effective Mass

An electron or hole in a crystal displays a different behaviour to that of a free electron in a vacuum. In order to compensate for this difference, we can assign the holes and electrons an effective mass m^* [74]. This allows us to retain the free particle model, but allow the mass to adjust the particles response to forces accordingly. The effective mass tensor can be written as [75]:

$$\left(\frac{1}{m^*}\right)_{ij} = \frac{1}{\hbar^2}\frac{\partial^2 E_n(\mathbf{k})}{\partial k_i \partial k_j}, \tag{2.35}$$

where $E_n(\mathbf{k})$ is the energy for band of index n at k-point **k** and the indices i and j represent the x, y and z directions in reciprocal space. The valence band maximum (VBM) has a negative gradient and has a negative effective mass. This is equivalent to a the response which would be experienced by a positively charged particle in an electric field, this is known as a hole. Where as, the conduction band minimum (CBM) has a positive mass and corresponds to an electron.

Effective masses may be highly anisotropic. Therefore, a scalar approximation called the "density of states effective mass", m^*_{dos} which may be used in transport theory can be defined as [75]:

$$m^*_{dos} = \sqrt[3]{g^2 m^*_l m^*_t m^*_t}, \tag{2.36}$$

where m^*_l and m^*_t are the longitudinal and transverse effective masses and g is the number of equivalent band minima inside the first Brillouin zone. Flat bands will produce large effective masses and steep gradients produce low effective masses. The variations in effective mass can span three orders of magnitude in relation to the electron rest mass, m_0.

2.4 Lattice Dynamics

2.4.1 Phonons

A phonon is a quantum of vibrational energy within a solid as a photon is a quantum of energy in an electromagnetic wave [58]. They are a quantum mechanical manifestation of wave-like normal modes observed in classical mechanics from which any arbitrary vibration can be described as a superposition of these normal modes. [76]. In order to study bulk properties of crystals, periodic boundary conditions must first be invoked, called the Born von Karman boundary conditions, which reduce the infinite system to a unit cell representation, albeit ignoring surface effects[24]. For an infinite crystal, vibrations can be considered as a travelling wave, where the direction and amplitude of vibration of each atom in one unit cell is invariant across all other unit cells. We can describe a crystal with a unit cell of atoms with positions in mechanical equilibrium and write an expression for a displacement $u_{\kappa,\alpha}$ from their initial equilibrium position $R_{\kappa,\alpha}$. In calculations of lattice dynamics, the first step is usually writing the Taylor expansion of the energy, for a unit cell labelled l and atoms labelled κ, this can be written as [77]:

$$E = E_0 + \frac{1}{2}\sum_{l}\sum_{\kappa,\alpha,\kappa',\alpha'} u_{\kappa,\alpha,l}.\phi^{\kappa,\kappa'}_{\alpha,\alpha'}(l).u_{\kappa',\alpha',l} + ... \tag{2.37}$$

where α and α' correspond to the Cartesian indices. In this expansion, all terms past the second-order term are neglected as the harmonic approximation is assumed. Moreover, there is no first-order term present as it is equal to zero, due to the equilibrium condition[77]. In order to obtain the necessary components to compute the vibrational properties using electronic structure theory, the degrees of freedom can be decoupled via the Born Oppenheimer approximation, which is outlined in Section 2.2.1. One then needs to obtain the matrix of force constants is given by [77]:

$$\phi^{\kappa,\kappa'}_{\alpha,\alpha'}(l) = \frac{\partial^2 E}{\partial u_{\kappa,\alpha,l}\partial u_{\kappa',\alpha',l}} \tag{2.38}$$

The guess for the solution to the equations of motion takes the form of a plane wave [77]:

$$u_{\kappa,\alpha} = \varepsilon_{m\kappa,\alpha\mathbf{q}} e^{(i\mathbf{q}.\mathbf{R}_{\kappa,\alpha} - \omega_m t)} \tag{2.39}$$

where $\mathbf{q}$ is the phonon wavevector and $\varepsilon_{m\kappa,\alpha\mathbf{q}}$ is the polarization vector with one longitudinal and two transverse modes for each wave vector. The equilibrium position vector $\mathbf{R}_{\kappa,\alpha}$ takes the form:

$$R_\kappa = \kappa\mathbf{a}_1 + \kappa\mathbf{a}_2 + \kappa\mathbf{a}_3 \tag{2.40}$$

with a_1, a_2 and a_3 being primitive lattice vectors along the respective x, y and z axes. From here the consequence of the Born von Karman boundary condition results in:

$$e^{i\mathbf{q}(\mathbf{R}_\kappa + N_i a_i)} = e^{i(\mathbf{q}.\mathbf{R}_\kappa)}, \tag{2.41}$$

enforcing a quantisation on the allowed values of $\mathbf{q}$ as:

$$\mathbf{q}_i = \frac{2\pi}{N_i a_i} l_i, (i = 1,2,3), \tag{2.42}$$

$$l_i = -\frac{N_i}{2}, -\frac{N_i}{2} + 1, ..., \frac{N_i}{2} - 1 \tag{2.43}$$

and N is the number of unit cells in the system [76].
Hence, it can be seen that a translation vector can bring any other $\mathbf{q}$ vector back into the first Brillouin Zone, and so the full set of allowed $\mathbf{q}$ points inside the first Brillouin zone describes the system completely. The phonon diagonalises the harmonic Hamiltonian and thus the solutions can be found by solving the dynamical matrix as an eigenvalue problem[78]:

$$D^{\kappa,\kappa'}_{\alpha,\alpha'}(\mathbf{q})\varepsilon_{m\kappa,\alpha\mathbf{q}} = \omega^2_{m,\mathbf{q}}\varepsilon_{m\kappa,\alpha\mathbf{q}} \tag{2.44}$$

where the dynamical matrix can be written in the form involving the Fourier transform of mass-reduced force constant matrix [79]

$$D^{\kappa,\kappa'}_{\alpha,\alpha'}(\mathbf{q}) = \frac{1}{\sqrt{M_\kappa M_{\kappa'}}} C^{\kappa,\kappa'}_{\alpha,\alpha'}(\mathbf{q}) = \frac{1}{\sqrt{M_\kappa M_{\kappa'}}} \sum_l \phi^{\kappa,\kappa'}_{\alpha,\alpha'}(l)\, e^{-i\mathbf{q}.\mathbf{R}_l}, \tag{2.45}$$

where M is the mass of an atom. If the solutions can be obtained then the eigenvectors will give the atomic displacements at each phonon mode and the square roots of eigenvalues will give the frequencies [80]. Therefore, all phonon properties can be determined solely through the knowledge of the interatomic force constant (IFC) matrix, which can be computed. Theoretical derivation of the second-derivative can be facilitated using the Hellmann-Feynman Theorem to find the forces, which correspond to the first derivative of the energy with respect to atomic displacement λ:

$$F = -\langle\psi|\frac{dV}{d\lambda}|\psi\rangle \tag{2.46}$$

then the second derivative $\frac{dF}{d\lambda}$ contains the required second-order energy, which by variational theorem also gives the first-order change in density, wavefunctions and potential. The second derivative is non-vanishing and has to be evaluated using either a technique called the finite displacement method[81]. This works by computing the electronic response of the system by calculating the numerical derivative at two atomic coordinates separated by a small displacement. Alternatively, this can be computed through the response wave function $\frac{d\psi}{d\lambda}$ using density functional perturbation theory (DFPT) calculated at a small distortion from the equilibrium geometry [82].

2.4.2 Phonon Dispersion

The dynamical matrix gives the relationship between the frequency and specific phonon mode at each allowed **q** point to give us the dispersion relation $\omega = \omega(\mathbf{q})$. Hence, allowing to plot this phonon dispersion relation and analysing each normal mode of vibration. There are 3 modes of vibration allowed for each atom for each polarisation with no energy transfer in between each mode[78]. There are always 3 long wavelength solutions are called the acoustic modes and represent in-phase motion of the atoms, moving along their respective cartesian directions. Whereas, short wavelength modes, called the optic modes involving out-of-phase motions and are only present when there are two or more different atoms within the unit cell, with $3n-3$ possible modes and with n being the number of atoms. These modes arise due to mass difference or charge difference of the atoms [24]. Phonon dispersions are generally plotted for a range of high symmetry directions, which depend on the particular Brillouin Zone of the simulation cell and it is accepted that those directions are sufficient to study vibrational spectra sufficiently. The group velocity of a phonon mode can be written as:

$$v_{j\mathbf{q}} = \frac{d\omega(j\mathbf{q})}{d\mathbf{q}}, \tag{2.47}$$

where j represents a phonon branch and $v_{j\mathbf{q}}$ is the group velocity.
We can also compute the mode Grüneisen parameter, γ which is usually used to measure the anharmonic phonon scattering rate and can be written as [63]:

$$\gamma(\mathbf{q}j) = -\frac{V}{\omega(\mathbf{q}j)}\frac{\partial\omega(\mathbf{q}j)}{\partial V}, \tag{2.48}$$

where V is the cell volume and $\omega(\mathbf{q}j)$ is the phonon frequency for a given **q**-point and phonon branch index j. This can be computed using a finite difference method, which requires three phonon calculations. The first is for eigenvectors at the equilibrium volume V and the remaining two are for cells with slightly larger and smaller volumes than the relaxed cell volume.

2.4.3 Density of states

If the phonon dispersion is known, then one can compute the density of states(DOS), $g(\omega)$, defined as the number of vibrations in a range of angular frequencies ω and $\omega + d\omega$[80]. In a crystal, the unit cell volume is equal to the total volume of the crystal divided by the number of unit cells, $\frac{V}{N}$ and the volume of the Brillouin Zone is equal to the reciprocal unit cell volume $\frac{(2\pi)^3 N}{V}$. Since there is one wave vector per unit cell, the number of wave vectors in a reciprocal unit cell is $(\frac{2\pi}{L})^3 = \frac{N_0\Omega}{8\pi^3}$[80]. In CASTEP the total density of states is computed as [80]:

$$g(\omega) = \int dk \sum_j \delta(\omega_j(k) - \omega(q)) \tag{2.49}$$

in the above equation, **j** represents the phonon mode as before. The accuracy of the calculated density of states can then be increased by including a larger number of **q** points, within the Brillouin Zone. Although only the irreducible part of the Brillouin Zone needs to be computed, so crystal symmetries can be exploited in lowering computational costs. Moreover, once the DOS is obtained then expressions for various thermodynamic functions can be written, of particular importance is generally the heat capacity behaviour. For phonon mode occupation number n, this is defined as:

$$c_v = \int \frac{\partial n}{\partial T} \omega g(\omega) d\omega \tag{2.50}$$

For example, the DOS for acoustic modes has an explicit frequency dependence at low ω of $\omega = ck$ where c is the average speed of sound and k is the modulus of the wave vector. But, optical modes are fully dependent on the force constants and do not have a known particular dependence[80].

2.4.4 Finite displacement method

The finite displacement is one of the methods for computing the IFC matrix in *ab initio* lattice dynamics. This is achieved by applying a small displacement to atoms away from their equilibrium positions and computing the forces of the perturbed configuration. The central-difference formula can then be used to compute the numerical derivative to find the force constants [81]:

$$\frac{\partial F_{\kappa,\alpha}}{\partial u} \approx \frac{F^{+}_{\kappa,\alpha} - F^{-}_{\kappa,\alpha}}{2u} = \frac{\partial^2 E}{\partial u_{\kappa,\alpha} \partial u_{\kappa',\alpha'}}, \tag{2.51}$$

where $F^{+}_{\kappa,\alpha}$ and $F^{-}_{\kappa,\alpha}$ are the positive and negative displacements respectively. This will allow to compute the dynamical matrix at $\mathbf{q} = 0$. To compute the dynamical matrix at any arbitrary wavevector **q** the finite displacement method can be combined with the supercell method. This approach relies on the fact that the IFC matrix is short-ranged and entails constructing a supercell containing enough atoms to fit an imaginary sphere of radius R_c beyond which the force constants can be assumed as negligible [83]. This magnitude of the radius R_c is system-dependent and is usually smaller for metallic systems than semiconductors and often increases with the complexity of the system. When the criteria for the size of the supercell $L > 2R_c$ is met then at the supercell wavevector $\mathbf{q}_{sc} = 0$, we can write [84]:

$$C^{\kappa,\kappa'}_{\alpha,\alpha'}(\mathbf{q}_{sc} = 0) = \phi^{\kappa,\kappa'}_{\alpha,\alpha'}(l), \tag{2.52}$$

where α denotes the index of atom κ in the primitive cell l. Using the definition of the dynamical matrix in Equation 2.45, we can apply the Fourier transform to compute the dynamical matrix at any **q** [84].

2.4.5 Non-diagonal Supercell method

An extension to the supercell method called the non-diagonal supercell method was formulated to reduce the computational cost of the supercell method through the use of smaller supercell matrices with non-zero off-diagonal elements [85]. It was proven that for a wave vector with reduced fractional coordinates $(m_1/n_1, m_2/n_2, m_3/n_3)$ there exists a commensurate supercell that has a number of primitive cells equivalent to the least common multiple of n_1, n_2 and n_3 [85]. This allows for more efficient sampling of the vibrational Brillouin Zone that scales better than the cubic scaling achieved with only diagonal supercell matrices [85] and can be used to compute the dynamical matrix on an arbitrary **q**-point grid [83]. This method has provided sufficient reduction in the computational cost for the calculations of thermal conductivity in defective supercells found in this work to make them possible using the available computational resources.

2.4.6 DFPT

Adding perturbation theory to DFT further extends its abilities in performing *ab initio* calculations, gaining insight into lattice dynamics and external electromagnetic field responses to those perturbations [79]. This method can overcome shortfalls of experimental quantities that are second-order, for example, the derivative of energy based on the atomic position to determine vibrational frequencies.
DFPT has been formalised using two approaches. Firstly, the self-consistent solution using Green function methods, which was implemented by Baroni[82]. This begins with an initial *ansatz* that the required physical quantities can be written as a perturbation series

$$X(\lambda) = X^{(0)} + \lambda X^{(1)} + (\lambda)^2 X^{(2)} + ... \tag{2.53}$$

where λ is the small perturbation[86]. Also, the coefficients in the expansion obey the relation:

$$X^{(n)} = \frac{1}{n!}\frac{d^n X}{d\lambda^n}|_{\lambda=0} \tag{2.54}$$

the first-order Kohn-Sham potential is given by:

$$H_{KS}^{(1)} = T^{(1)} + v_{ext}^{(1)}(r) + e^2 \int \frac{\rho^{(1)}(r`)}{|\, r - r` \,|} dr` + \int \frac{\delta v_{xc}}{\delta \rho(r`)} \rho^{(1)}(r`) dr` \tag{2.55}$$

Combining this with the variation in Kohn-Sham orbitals gives the Sternheimer equation[87]:

$$(H_{KS}^{(0)} - \varepsilon_n^{(0)}|\psi_n^{(1)}\rangle = (H_{KS}^{(1)} - \varepsilon_n^{(1)}|\psi_n^{(0)}\rangle \tag{2.56}$$

and by the means of the orthogonality condition and normal perturbation theory procedure, the usual Rayleigh-Schrödinger resembling perturbation result can be found for the first order perturbation:

$$|\psi_n^{(1)}\rangle = \sum_{m \neq n} C_{nm}^{(1)} |\psi_m^{(0)}\rangle \tag{2.57}$$

with the corresponding coefficients given by:

$$C_{nm}^{(1)} = \frac{\langle \psi_m^{(0)} | H_{KS}^{(1)} | \psi_n^{(0)} \rangle}{\varepsilon^{(0)} - \varepsilon_m^{(0)}} \tag{2.58}$$

determining the solution of the first-order correction then requires the knowledge of all eigenvalues[86]. However, the simplification by Baroni comes from the next steps. Firstly, writing the equation of the first order electron density and, which has a linear dependence on the Kohn-Sham Hamiltonian[82]. The products of occupied states cancel and mean that the first-order perturbation will apply to the coupling of valence and conduction band manifolds.

A projection operator can be used to cast the wave function onto the conduction band manifold[82]:

$$P_c(H_{KS} - \varepsilon_v^{(0)})P_c|\psi_v^{(1)}\rangle = -P_c H_{KS}^{(1)}|\psi_v^{(0)}\rangle \tag{2.59}$$

where

$$P_c = \sum_c |\psi_c^{(0)}\rangle\langle\psi_c^{(0)}|$$

Finally, we can use the Green's function operator in this approach, via the equation shown below:

$$|\psi_v^{(1)}\rangle = G_v H_{KS}^{(1)}|\psi_v^{(0)}\rangle \tag{2.60}$$

and G_v is given by:

$$G_v = \sum_c \frac{|\psi_c^{(0)}\rangle\langle\psi_c^{(0)}|}{(\varepsilon_v^{(0)} - \varepsilon_c^{(0)})} \tag{2.61}$$

In conclusion, this form of the wave function means the solution can be found only using the occupied state eigenvalues.

2.4.7 The Gonze (2n + 1) Theorem

The theorem itself simply states that a derivative of a Hamiltonian eigenenergy of the $(2n+1)$ order only needs the eigenfunctions up to the n^{th} term. This will be true for any Hamiltonian with a small perturbation[11]. Adding the perturbation means that the variational principle is obeyed, which means the true wave function functional yields the true minimum value for ground state energy. What Gonze showed was the first perturbative expansion of the Kohn-Sham energy functional. In addition, he proved the existence of even-order variational principles. By using the method of Lagrange multipliers and constraining the particle number, he formulates an expression for the energy [88]:

$$E_0^{(2n+1)} = (\widehat{E}_{(\lambda)}[\sum_{i=0}^{n} \lambda^i \phi_0^{(i)}] - \Lambda_0(\lambda)\widehat{C}_{(\lambda)}[\sum_{i=0}^{n} \lambda^i \phi_0^{(i)}])^{(2n+1)}, \tag{2.62}$$

where Λ is the Lagrange multiplier and $\widehat{C}$ is a functional constraining the domain of the variation of the wave function. This is the form for the $2n+1$ theorem and the even-order can be shown to obey the stationary principle. Using principles of gauge freedom when finding the Lagrange multiplier for the expansion of the Kohn-Sham orbitals, after analysis it can be shown that the first-order wave function is orthogonal to the valence manifold[86]:

$$\langle \psi_\alpha^{(0)} | \psi_\beta^{(1)} \rangle = 0 \tag{2.63}$$

The approach by Gonze can be linked back to the Green function approach and can be written in the form of the Sternheimer equation[86]. The Gonze and Green's function methods should both converge to the same answer, but only Gonze's method relies on the variational principle and so it converges better. In addition, it is more accurate because the Green's function method has additional errors from first-order errors in the wavefunctions, $\psi^{(1)}$ when computing the second-order energy [89].
The introduction of both of the approaches by Baroni and Gonze meant that since then DFPT calculations could be implemented with a much more accuracy [79], providing advances in simulations of lattice dynamics and electromagnetic field responses.

2.4.8 Phonon unfolding

When modelling the phonon dispersion of a system that breaks translational crystal symmetry due to complexities caused by various defects, alloying, interfacial reconstruction or other deviations from an ideal crystal, we can use the supercell method to attempt to model such crystal structures [90, 91]. However, this approach results in the folding of the phonon dispersions due to the smaller first Brillouin zone of the supercell, which means that analysis of the calculated phonon dispersion becomes very difficult [91]. Hence, a method for unfolding the supercell phonon dispersion onto a corresponding primary-cell Brillouin zone is required. An unfolding scheme using a generalised projection algorithm has been proposed [91] and has been used to unfold the phonon dispersion of defective supercells found in this thesis. This method uses the plane wave basis and constructs a projection operator $\hat{\mathbf{P}}_b (b = 1,2,3,...,n)$ where n is the number of supercell Brillouin zones contained in the primary-cell Brillouin zone, which can be written as [91]:

$$\hat{\mathbf{P}}_b = \sum_{j,\alpha} |w_{j,\alpha,b}\rangle\langle w_{j,\alpha,b}| \tag{2.64}$$

and $|w_{j,\alpha,b}\rangle$ takes the form [91]:

$$|w_{j,\alpha,b}\rangle = \frac{e^{i(\mathbf{G}_b+\mathbf{g}_j).\mathbf{R}_I}}{\sqrt{N}} \delta_{\alpha,\alpha'}, \tag{2.65}$$

where $\mathbf{R}_I$ is the position of the I^{th} atom, N is the number of atoms, $\alpha = 1,2,3$ corresponds to the the x, y, z Cartesian directions, $\mathbf{G}_b$ and $\mathbf{g}_j$ are the reciprocal lattice points of the supercell and primitive cell respectively. This projection operator can be used to compute the unfolding weight [91]:

$$|c_{\mathbf{Q}+\mathbf{G}_b}|^2 = \langle \phi_{\mathbf{Q}} | \hat{\mathbf{P}}_b | \phi_{\mathbf{Q}} \rangle, \tag{2.66}$$

where $\phi_{\mathbf{Q}}$ is the component of the phonon polarisation vector $\psi^{\alpha}_{\mathbf{Q}}$ [91]:

$$\psi^{\alpha}_{\mathbf{Q}}(\mathbf{R}_I) = \phi^{\alpha}_{\mathbf{Q}}(\mathbf{R}_I) e^{i\mathbf{Q}.\mathbf{R}_I}, \tag{2.67}$$

obtaining these unfolding weights allows plotting the supercell phonon dispersion along the primary-cell Brillouin zone. Due to the generalised approach of this method, this scheme can be used for any complex system requiring the use of supercells to model the desired structure and analyse the nature of the phonon dispersion.

2.5 Transport properties

2.5.1 Thermal conductivity

Within the harmonic approximation there are no phonon-phonon interactions between different modes and lattice momentum is conserved, so heat conduction in this scenario is infinite, which is clearly non-physical in a real crystal. Only by including scattering mechanisms which provide thermal resistivity does the thermal conductivity become finite. The scattering mechanisms are of either of geometrical or phonon scattering nature [58]. These include anharmonic effects, grain boundary, defect or mass-disorder scattering as well as others. I will mainly try to investigate three phonon scattering events for the two allowed coalescence and decay processes which obey energy conservation laws. Where either two phonons annihilate to produce one phonon or one phonon decaying into two phonons. This can be expressed in terms of momentum as [92]:

$$q + q' = q'' + G \tag{2.68}$$

and

$$q = q' + q'' \tag{2.69}$$

where each phonon has their own frequency ω, ω' and ω''. In the coalescence process, the reciprocal lattice vector G is necessary for a process called Umklapp-scattering, where momentum conservation requires a translation of the new phonon back into the first Brillouin zone, effectively reversing the direction of the phonon. It is therefore this process which can cause thermal resistivity and lead to a finite value for thermal conductivity[58]. All processes which lie within the first Brillouin zone are called normal processes and there is no change to the total momentum and $G = 0$. However, it is clear that for Umklapp

scattering to occur the wavevectors of the two interacting phonons must be of the order of $\frac{1}{2}G$ and so the rate of Umklapp scattering increases as the temperature increases. Therefore the thermal conductivity is lower at higher temperatures and the mean free path value when computing the thermal conductivity stems only from this type of process whilst ignores the remaining normal processes [58].

One way to model lattice thermal conductivity is through the phonon Boltzmann transport equation(BTE). It translates the phonon mode occupation number into a distribution function $f_{j\mathbf{q}}(\mathbf{r},t)$ at position $\mathbf{r}$ and time t, where the distribution is the Bose-Einstein distribution as phonons are bosons. And j labels the phonon branch. This would lead to a set of mode distributions along a trajectory, but thermal transport is a random process and energy does not travel ballistically [58]. Therefore, the thermal flux is dependent on the temperature gradient and a mean free path that represents the average phonon path between collisions. The total change of the phonon mode occupation number in the presence of a thermal gradient is then expressed as [48]:

$$\frac{\partial f_{j\mathbf{q}}}{\partial t} = \frac{\partial f_{j\mathbf{q}}}{\partial t}|_{diffusion} + \frac{\partial f_{j\mathbf{q}}}{\partial t}|_{scattering} \tag{2.70}$$

with the contribution separated for the diffusion and scattering mechanisms. Firstly, looking at the diffusion, phonons have a group velocity, v_q and by taking the thermal gradient into account on which $f_{j\mathbf{q}}$ depends according to the position $T = T(\mathbf{r})$, the diffusion rate can be written as:

$$\frac{\partial f_{j\mathbf{q}}}{\partial t}|_{diffusion} = -v_j(\mathbf{q}) \bigtriangledown T \frac{f_{j\mathbf{q}}}{\partial T} \tag{2.71}$$

At this point a steady state approximation can be introduced where the total rate of change in the phonon distribution must be zero. Now the BTE takes the form:

$$-v_{j\mathbf{q}} \bigtriangledown T \frac{f'_{j\mathbf{q}}}{\partial T} + \frac{\partial f_{j\mathbf{q}}}{\partial t}|_{scattering} = 0, \tag{2.72}$$

where $f'_{j\mathbf{q}}$ is the deviated occupation number, which is given as the average occupation number based on the Bose-Einstein distribution, but with a number of modes deviated from equilibrium due to the thermal gradient.

The BTE can be solved by approximating the thermal current to be small for most practical applications of the method, so that the deviation of the phonon mode distribution from equilibrium will be small and can be expanded to first order as $f_{l\mathbf{q}} = f^0_{j\mathbf{q}} + g_{j\mathbf{q}}$, where $f^0_{j\mathbf{q}}$ is the equilibrium phonon distribution according to Bose-Einstein statistics and $g_{j\mathbf{q}} = -\mathbf{F}_{j\mathbf{q}} \bigtriangledown T \frac{df^0_{j\mathbf{q}}}{dT}$, considering only two -phonon and three-phonon as the scattering mechanism, the linearized BTE can be written [48]:

$$\mathbf{F}_{l\mathbf{q}} = \tau^0_{l\mathbf{q}}(\mathbf{v}_{l\mathbf{q}} + \Delta_{l\mathbf{q}}) \tag{2.73}$$

And, $\tau^0_{j\mathbf{q}}$ is the relaxation time denoting the time a phonon mode will travel before scattering, $\mathbf{v}_{j\mathbf{q}}$ is the phonon velocity and $\Delta_{j\mathbf{q}}$ is the measure of the deviation from the relaxation

time approximation (RTA) with dimensions of velocity. If we were to set $\Delta_{j\mathbf{q}} = 0$. This would equate to a solution equivalent to the RTA where the solution to the BTE does not include correct treatment of normal three-phonon scattering processes [48]. Solving the linearized BTE allows us to then compute the lattice thermal conductivity, κ_l [48] and write it as:

$$\kappa_l = \frac{1}{k_B T^2 \Omega N} \sum_{j\mathbf{q}} f^0_{j\mathbf{q}}(f^0_{j\mathbf{q}} + 1)(\hbar\omega_{j\mathbf{q}})^2 \mathbf{v}_{j\mathbf{q}} \mathbf{F}_{j\mathbf{q}}, \tag{2.74}$$

where Ω is the unit cell volume, k_B is the Boltzmann constant, N is the number of q points in the regular grid used to discretise the Brillouin zone for a calculation, $\hbar$ is the reduced Planck constant, $\omega_{j\mathbf{q}}$ is the phonon frequency. To obtain the necessary components of this equation we require the second-order force constants that will allow to determine the phonon velocity and phonon frequency as well as the phonon distribution function. However, the complex and computationally demanding aspect arises in the computation of $\tau^0_{j\mathbf{q}}$ and $\Delta_{j\mathbf{q}}$ that require the knowledge of the third-order anharmonic force constants, which can be obtained from the expansion of the total potential energy of the system and written as [48]:

$$\phi^{\kappa,\kappa',\kappa''}_{\alpha,\alpha',\alpha''} = \frac{\partial^3 E}{\partial u_{\kappa,\alpha} \partial u_{\kappa',\alpha'} \partial u_{\kappa'',\alpha''}}, \tag{2.75}$$

and $\phi^{\kappa,\kappa',\kappa''}_{\alpha,\alpha',\alpha''}$ be calculated using a the supercell finite-difference method. Here, $\alpha, \alpha', \alpha''$ correspond to Cartesian coordinates and $\kappa, \kappa', \kappa''$ are the atomic indices. This method allows us to theoretically model κ_l going beyond the RTA and obtain a better prediction particularly in systems where normal three-phonon processes are important.

2.5.2 Modified Debye-Callaway Model

There exist alternative methods of computing the lattice thermal conductivity than the previously described approach using the relaxation time approximation or iterative solution of the Boltzmann transport equation. The method we will present here is based upon a modified Debye-Callaway model that builds upon the traditional Debye-Callaway description of κ_l to provide an accurate and computationally inexpensive calculation to approximate κ_l. The advantage of the method stems from the fact that it does not require the knowledge of an anharmonic force constant matrix [54]. In the Debye-Callaway model the total contribution to κ_l comes from contributions of the acoustic modes, namely the longitudinal κ_{LA} branch and the two transverse branches κ_{TA} and $\kappa_{TA'}$ and their sum can be written as [93]:

$$\kappa = \kappa_{LA} + \kappa_{TA} + \kappa_{TA'} \tag{2.76}$$

The modified Debye-Callaway model updates this description to include an additional contribution from a pseudo-optic branch κ_O, so that the new weighted average to describe the total κ_l can be written as [54]:

$$\kappa = \frac{c_V^{aco}}{c_V^{aco}+c_V^{opt}} \times \frac{\kappa_{LA}+\kappa_{TA}+\kappa_{TA'}}{3} + \frac{c_V^{opt}}{c_V^{aco}+c_V^{opt}} \times \kappa_O, \tag{2.77}$$

where c_V^{aco} and c_V^{opt} are the specific heat of the acoustic and optic branches respectively. In the Debye-Callay model the contribution of both the Umklapp phonon processes and the normal phonon processes contribute to the thermal conductivity, the latter is accounted as it can redistribute the phonon energy and momentum which can effect the resistive scattering processes [54, 93]. Therefore the total scattering rate, which the thermal conductivity is a function of, is specified as $\frac{1}{\tau_C} = \frac{1}{\tau_R} + \frac{1}{\tau_N}$ with τ_R denoting the contribution due to all resistive scattering processes, such as Umklapp phonon-phonon scattering and τ_N corresponds to the contributions from normal phonon scattering [93]. Hence, we can write the partial conductivity as $\kappa_i = \kappa_{i1} + \kappa_{i2}$ with i corresponding to the LA, TA or TA' modes to take the form [54]:

$$\begin{aligned} \kappa_{i1} &= \frac{1}{3} C_i T^3 \int_0^{\Theta_i/T} \frac{\tau_C^i(x) x^4 e^x}{(e^x-1)^2} dx \\ \kappa_{i2} &= \frac{1}{3} C_i T^3 \frac{\int_0^{\Theta_i/T} \frac{\tau_C^i(x) x^4 e^x}{(e^x-1)^2} dx}{\int_0^{\Theta_i/T} \frac{\tau_C^i(x) x^4 e^x}{\tau_N^i(x)\tau_R^i (e^x-1)^2} dx}, \end{aligned} \tag{2.78}$$

in the above equations $C_i = k_B^4/(2\pi^2\hbar^3 v_i)$, k_B is the Boltzmann constant, $\hbar$ is the Planck constant, $x = \hbar\omega/k_B T$, where ω is the phonon frequency and v_i is the phonon velocity for the respective phonon branch. The specific heat of the acoustic and optic branches mentioned previously in Equation. 2.77 can be computed using the Debye model for the acoustic branches and using the Einstein model for the optic branches [54]:

$$\begin{aligned} c_V^{aco} &= 3\frac{N}{V} k_B f_D \left(\frac{\Theta_D}{T}\right) \\ c_V^{opt} &= (3p-3)\frac{N}{V} k_B f_E \left(\frac{\Theta_E}{T}\right), \end{aligned} \tag{2.79}$$

where Θ_D and Θ_E are the Debye temperature and Einstein temperature respectively, N is the number of primitive calls and f_D and f_E are the Debye and Einstein function [54]:

$$\begin{aligned} f_D(x) &= \frac{3}{x^3} \int_0^x \frac{y^4 e^y dy}{(e-1)^2} \\ f_E(x) &= x^2 \frac{e^x}{(e-1)^2}, \end{aligned} \tag{2.80}$$

The method as implemented in the mDCThermalC code used for the calculations of the thermal conductivity in this thesis takes into account phonon-phonon normal scattering processes, Umklapp scattering, and isotope scattering processes. The inputs required are

the phonon dispersion, phonon velocity, and mode Grüneisen parameters which can be obtained from *ab inito* DFT calculations [54]. This method applies to a wide range of materials, but it should be noted that an approximation to the optical branch is made as it is treated as a longitudinal acoustic branch in the outlined formalism.

Chapter 3

Methodology

3.1 Computational methods

Modelling the properties of materials to give a picture of real physical phenomena with confidence requires choosing the correct theoretical framework for the system one wishes to study. In addition, a complex procedure to correctly implement and test the theory and methods is required before reaching a final result. Computing resources are vastly more abundant than they have ever been before, but many *ab inito* endeavours can easily become prohibitively expensive. The often differentiating factor of a materials modelling expert is the ability to strike a fine balance in the trade-off between accuracy and computational expense. Consequently, each of the steps in a computational procedure requires extra care and thorough consideration of the modifiable parameters in the calculations as well as the limitations of the chosen model.
This chapter will attempt to provide the necessary detail and insight to enable reproducibility of the results found in this work as well as outlining the software used and tests performed in order to verify the results.

3.1.1 First principles calculations

All of the DFT calculations for the determination of the electronic structure and vibrational properties were obtained using the CASTEP first principles simulation package [51]. CASTEP is a leading DFT plane wave basis code, which has the ability to compute a wide range of properties of crystalline solids, surfaces, molecules, liquids and amorphous materials. This includes the use of the CASTEP "on-the-fly" ultrasoft pseudopotential (USP) libraries which have been used throughout.

3.1.2 Requirements for a CASTEP calculation

In order to prepare and run a simulation, the CASTEP code requires two input files in the form of a <seedname>.cell and <seedname>.param file, the former specifying the key structural information, such as the lattice vectors, ionic positions, choice of

pseudopotentials, symmetries, cell constrains, Monkhorst-Pack **k**-point grid for sampling the Brillouin zone [94], and more calculation specific information. This can include the choice of the Hubbard U parameter, spin initialisation, phonon interpolation grids, and more.
On the other hand, the <seedname>.param input file is responsible for task dependent parameters in a calculation. The key parameters being the choice of task, the exchange-correlation functional, and the plane wave cut-off energy. However, the parameter file enables much more control than this, including setting initial conditions, control of parallelism, memory, level of output data and many task-specific options. The user need not specify all of the parameters as there are many default parameters already set and it is good practice to alter parameters one at a time and consult the output thoroughly to check for any apparent errors.

3.1.3 Convergence testing

Cut-off Energy

A crucial aspect of obtaining a reliable result lies in the convergence testing with respect to the energy cut-off and **k**-point grid size. The plane-wave cut-off determines the size of the basis set and is dependent on the type of atom in the system one wishes to simulate.
As an example, convergence tests had to be performed for stoichiometric half-Heusler compositions with an X-site substitution, i.e. XNiSn (X = Ti, Zr, Hf), but the cut-off can be assumed to be kept the same in the case of excess Nickel in $XNi_{1+x}Sn$ compositions as there is no change of element involved, reducing unnecessary computational expense.
Thankfully, it turns out that the size of the basis-set required can be truncated up to some cut-off energy. Due to the fact that only the plane waves with small kinetic energy have the largest contribution to the accuracy of the total energy.[95] The size of the matrix for solving the Kohn-Sham equations is determined by the cut-off energy, defined as the highest Fourier component:

$$E_c = \frac{\hbar^2}{2m}|\mathbf{k}+\mathbf{G}|^2, \tag{3.1}$$

where **k** and **G** are the real and reciprocal lattice vectors respectively.
Systematic calculations of total energy and stress at varying values of cut-off energy and **k**-point grid sizes, were performed for convergence purposes. An example for a convergence test for NbCoSb can be seen in Figures 3.1a and 3.1b. Oscillations in the total energy upon increasing the **k**-point grid size are to be expected as convergence is not variational and will vary depending on the chosen discrete **k**-point mesh used. Therefore the **k**-point grid should be converged based on the required convergence tolerance criteria.
The total energy is computed using a self-consistent loop with the help of a density mixing scheme. One should test different density mixing schemes, using the *mixing_scheme* keyword in the parameter file if a calculation is failing to converge or the convergence

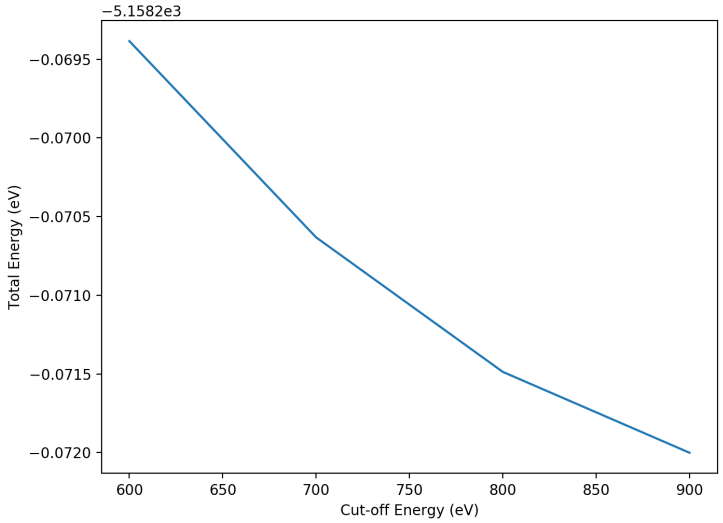

(a) Total Energy of NbCoSb vs cut-off energy.

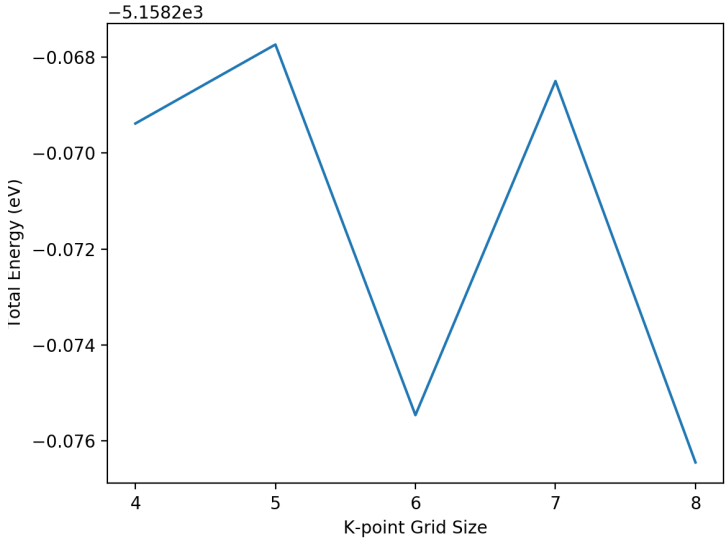

(b) Total Energy of NbCoSb vs k-point grid (n x n x n).

Fig. 3.1 Total energy convergence with respect to energy cut-off and k-point grid for NbCoSb.

procedure is taking many self-consistent loops to do so. After benchmarking various schemes available in CASTEP, I have found the Pulay [96] density mixing scheme to be the best performing. In addition, all of the calculations presented in the results section were converged to a total energy difference of 0.5meV per atom or less with stress converged to less than 0.1GPa.

Basis set convergence is important to make sure the orbitals are represented as accurately as possible. This is because ground state energy is variational. Hence, better convergence of the basis set results in a lower error in energy. However, convergence should be prioritised with the property of interest in mind and can usually provide good accuracy for the required purpose with incomplete basis sets whilst using a reasonable amount of computational resources. A significant speed-up can be gained due to the fact that when converging with respect to cut-off energy a grid with few **k**-points can be used as the convergence is independent or vice versa. Forces converge even faster than the aforementioned parameters due to not having to deal with the large Fourier components near the nucleus. However, they are not always possible to converge depending on the choice of unit cell. In this case, a stress convergence can be done instead. By default, no Hubbard U parameter is specified, but the correction can be applied to a chosen set of atoms and orbitals within the <seedname>.cell file.

K-point sampling

The set of allowed **k**-point values is determined by the periodic boundary conditions. There will be a number of contributing occupied electronic states that specify the electronic potential and are therefore needed in order to accurately compute the correct total energy of the system. Computing many quantities, such as the total energy or density requires a Brillouin zone integral, the general form of this integral for some lattice-periodic function *F(**k**)* is given by [97]:

$$\frac{\Omega}{(2\pi)^3}\int_{BZ} d\mathbf{k}F(\mathbf{k}) = F_0 \approx \sum_{j=1}^{N_w} w_j F(\mathbf{k}_j), \tag{3.2}$$

where Ω is the cell volume, F_0 is the lowest Fourier component, w_j are weighting factors for a special set of **k**-points found using the Monkhorst-pack method [94], N_w is the number of irreducible **k**-points within the irreducible Brillouin Zone (IBZ) wedge, where $j = 1,...,N_{special}^{irred}$ and $\sum_j w_j = 1$. The number of special points in the IBZ depends on the point-symmetry of the system [97]. Due to the fact that nearby **k**-points have similar solutions and in high symmetry systems with filled bands, such as semiconductors, a great example being the half-Heusler systems in question, meaning that the total energy can be computed efficiently whilst requiring a relatively small **k**-point grid. This is evident from my calculations the desired convergence criterion was reached with a 6x6x6 Monkhorst-pack grid in the primitive cell. Generally denser grids are required for metallic systems. A **k**-point convergence test such as the one that has been described can generally

minimise the computational expense whilst keeping the error relatively low. Moreover, when computing defective structures generally a supercell has to be created in order to represent the desired periodicity, which increases the number of atoms in the system. In turn, increasing the computational expense. However, this can be offset by the fact that increasing the simulation cell size reduces the size of the Brillouin zone. Hence, the same sampling density as for the primitive cell can be achieved with a smaller **k**-point grid.

3.1.4 Structural Relaxation

Geometry optimisation was done in order to make sure the structure is as close to equilibrium as possible ensuring the total energy and forces are converged to a high degree of accuracy, dictated by a user-modifiable set of convergence tolerance criteria. This optimisation problem was tackled using a gradient minimisation algorithm developed by Broyden, Fletcher, Goldfarb and Shanno(BFGS) [98] as well as a modified, low memory version of this called L-BFGS [99]. Calculations were deemed successful if two consecutive minimisation steps meet the minimum convergence criteria or better.
A high-quality convergence is especially important when performing a well converged phonon calculation, more so than for studying the electronic structure properties. Failure to do so can lead to large errors in phonon frequencies and give rise to imaginary frequencies, giving a qualitatively and quantitatively incorrect picture.
The convergence values for the **k**-point grid depending on the size of supercell used to obtain the results in this work are those stated in Table 3.1. Whereas the forces were converged to 0.03eV/atom and stress was converged to 0.05 GPa or better. Lattice parameters were re-optimised when changing from the Generalised-Gradient Approximation (GGA) PBE [69] exchange-correlation functional to the meta-GGA rSCAN [100] where applicable.

Cell Dimensions	K-Point Grid
1x1x1	6x6x6
2x2x2	4x4x4
2x2x4	4x4x2
2x4x4	4x2x2

Table 3.1 Simulation cell size dependent structural relaxation convergence parameters.

3.1.5 Electronic Band Structure

In the CASTEP package, there are two methods for computing a band structure. The first is the bandstructure task, which computes the set of eigenvalues at a chosen set of k-points. This set can be specified within the <seedname>.cell file as a path along with a set of high-symmetry directions or simply as a list. It is important to ensure that a robust set of high symmetry directions is chosen as failing to do so can result in not being able to

visualise key features of the band structure for analysis. However, this only needs to be done within the irreducible wedge of the Brillouin zone and symmetry equivalent points will be detected by the code to reduce computational expense.
The second method is selected by choosing the spectral keyword for the task parameter, this will then also require an additional input parameter spectral_task, which provides information about the task-specific to a spectral calculation. The spectral task is a newer implementation and is recommended. However, the spectral task is not yet fully implemented to be used with the band unfolding tool bs_sc2pc.f90, which is necessary when computing band structures of supercells. This will be described in more detail later. Due to this restriction of the spectral task, all of the band unfolding calculations presented in this thesis were performed using the bandstructure task.
Furthermore, CASTEP also contains two useful tools to post-process the output band structure data. The data can be found within the <seedname>.bands output file. The first of which is a Perl [101] script that is aimed to allow easy plotting of the band structure, called dispersion.pl. The other is a Fortran90 [102] script, namely orbitals2bands.f90. This is an optional, but recommended post-processing tool which attempts to perform a band crossing detection and re-order the bands appropriately, re-writing the <seedname>.bands file to retain the same file formatting.

Effective Band Structure

As mentioned earlier, when studying defective systems a supercell is usually required to model the structure [103], this means the well-defined E versus $\vec{k}$ relationship is no longer present. Therefore, obtaining a direct comparison with ordered structures or experiments to study the effects of the defects or substitutions requires additional work. This can be achieved through the use of effective band structures (EBS) to obtain an unfolded representation of the bands. The amount of folding present increases with supercell size and the number of the defects in the structure, prohibiting any attempt to analyse supercell band structure from a usual plot of eigenvalues obtained for each **k**-point. The method consists of computing the spectral weight of the supercell energy eigenvalue at a given supercell **K**-point by projecting the corresponding eigenstate on all primitive cell Bloch states corresponding to a **k**-point in the primitive cell. Where the weight represents the Bloch character preserved in the supercell [103]. Hence, with this information, the spectral function $A(\mathbf{k}, E)$ can be derived. Where its resolution in **k** is limited by the chosen set of **k** points at which the EBS and BS were evaluated [103].
A test was performed on a defect free supercell of the stoichiometric TiNiSn, the result of which can be seen in Figure 3.2. Here, the spectral weight can be seen to match the underlying primitive cell band structure as expected. The advancements of this method have also allowed some techniques to be applied to phonon dispersion unfolding[91], which I have also required in order to analyse and compare the effects on the nature of the phonon modes. This will be described in Section 3.1.6.

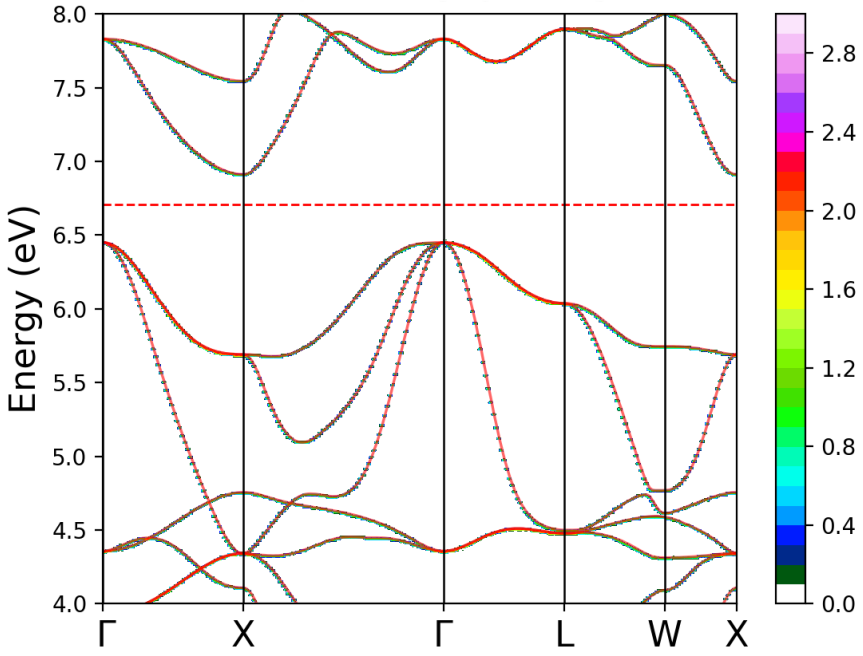

Fig. 3.2 Unfolded band structure of a 2x2x2 supercell of the TiNiSn primitive fcc unit cell. The value of 1 on the colour bar corresponds to a single non-degenerate band per energy interval. The continuous red line is the band structure for TiNiSn, calculated using a primitive fcc unit cell. The dotted red line indicates the Fermi energy.

Density of States

Having a band dispersion is very insightful. However, it does not give the whole picture, this is where a density of states (DOS) can provide additional information and is often important in understanding the underlying physics.

The computational procedure is almost identical to that of the band structure calculation, it can be invoked by changing the Brillouin zone sampling path to a sampling grid, in order to evenly sample and count the total number of states at each energy level. Therefore, the DOS is an integral through the Brillouin zone of the primitive cell and takes the form:

$$g_n(\varepsilon) = \int \frac{d\mathbf{k}}{4\pi^3} \delta(\varepsilon - \varepsilon_n(\mathbf{k})), \tag{3.3}$$

where g_n and ε_n are the DOS and the energy for a band of index n. A dense grid is often required to obtain a good DOS. Moreover, as space is discretised. Plotting often requires a broadening scheme, which aims to discern between real and fictitious sharp peaks, whilst computing the DOS on a relatively coarse grid. However, symmetry equivalent **k**-points do not need to be recomputed. This is utilised to reduce the computational cost. There are two ways to approach this in CASTEP. The <seedname>.bands file can be read and plotted by a script provided as part of the CASTEP distribution, called dos.pl. This enables the use of a fixed width broadening scheme. Using a fixed-width Gaussian function has limited ability to deal with sharp features of a DOS and in order to overcome this, there is a post-

processing program called OptaDOS [104]. This utilises an adaptive broadening scheme, which takes into account the band gradients, thus coping better with the aforementioned difficulties with sharp features. OptaDOS has many additional capabilities for computing optical, core-level excitation spectra as well as partial and joint electronic DOS [104]. Moreover, the program can give additional output with information regarding the presence and magnitude of a band gap or locating the valence band maximum as well as the conduction band minimum, which can be helpful when performing analysis of the effective electron mass.

Effective electronic mass

There are many approaches to approximating the effective electron mass from a band structure calculation. Quite often this requires a manual procedure of fitting a parabola to the bands by hand. However, there are now semi-automated procedures available to do this. The natural choice for the calculations in this work is the EMC code [105]. This program has been specifically written as an interface to CASTEP in order to work with CASTEP's band structure code.
The basis upon which the EMC program is formulated rests on a finite difference method for evaluating the second derivatives of the energy numerically. As this is a semi-automated procedure, the program requires an additional emc-input file as well as editing the code script to choose between a three or five point stencil for generating a k-point list. For this, the user must specify the index of the band and the **k**-point at the bands extrema to generate a set of **k**-points for which the band structure will be performed to obtain the necessary data to compute the derivatives. To aid this process, one can use the OptaDOS output information to find the location of the VBM and CBM. However, this will not always succeed and if one wishes to compute effective masses of supercells, particularly with defects present, the matter becomes significantly more difficult. This is because band folding can lead to translations of the VBM or CBM onto a different **k**-point. In addition, the required components of the effective mass may not appear as part of the same band. Hence, extra care is required when preparing the input file. Finally, there is one more important input parameter, namely the step_size, which determines the difference between the **k**-points in the generated list. There is no correct way to choose this. However, choosing too small a step size will give a better approximation to the derivative when for light bands and a large step size favours heavy bands. It is best to benchmark the step size against experimental data if possible. The EMC code must first be run only with the emc-input file to generate the **k**-point list. This list must then be input into the CASTEP <seedname>.cell file. Once this is done, one might then proceed with a regular CASTEP band structure calculation. When this is ready the EMC code may be run again for a chosen band index to compute the effective masses.

3.1.6 Lattice Dynamics

Finite Displacement Method

Obtaining the vibrational spectra within the harmonic approximation requires the knowledge of the second-order force constants. This task was also done using CASTEP. There are two implementations to chose between, a finite-displacement supercell approach or DFPT. During the preliminary stages of research, both methods and their convergence were tested on stoichiometric compositions, and the finite-displacement method was chosen to complete this task. Hence, this is the method that will be described in more detail here.
The method focuses on evaluating forces on a set of perturbed configurations. These are configurations containing small positive and negative displacements in each direction, one atom at a time. Then using the central difference formula with the computed forces to construct the force constant matrix (FCM) [83]. In order to compute the FCM for an arbitrary choice of q-point, a supercell is required. The method relies on the short-ranged nature of the forces, which generally converge quickly as L > 2R_c, where L is the supercell size and R_c is a spherical cut-off radius. Hence, upon increasing supercell size the approximate force constant matrix will begin to converge. This may be done by setting the task parameter to *phonon* and adding an additional parameter, phonon_task to textitfinite-displacement in the <seedname>.param file. When the FCM has been computed, a Fourier interpolation scheme may be used. This can be specified with the phonon_fine_method parameter and setting it to *interpolation*. This will then generate a dynamical matrix for a fictitious supercell size and can be specified in the <seedname>.cell file, by setting the phonon_fine_kpoint_path or the phonon_kpoint_mp_grid keyword to produce high-quality phonon dispersion and density of states plots. A dense grid is often required to obtain a good quality DOS, but this may be done as a continuation of the phonon calculation using the output <seedname>.check checkpoint file. In addition, the phonon_calculate_dos parameter must be set to true. The output will be saved to the <seedname>.phonon file and will contain the Total DOS as well as the contribution to the DOS from each atomic species. This allows the plotting of a partial phonon DOS, in order to analyse the phonon spectra in more depth.
Even though the DFPT method computes the force constants on a q-point grid and therefore tends to scale better than increasing the supercell size. The finite displacement method has its advantages and has recently received a significant speed-up. There are two main advantages to note. The DFPT method is much harder to implement and therefore can be used only with norm-conserving pseudopotentials, but the finite-displacement method makes use of the USP set, which significantly reduces the required cut-off energy, in the case of TiNiSn this is a reduction from 1600eV to 600eV. Moreover, thanks to the non-diagonal supercell method [85], which as the name suggests, uses smaller non-diagonal supercell matrices in order to access all of the necessary perturbations for each k-point. This speed-up allowed for much larger supercells to be accessible using the computational resources available.

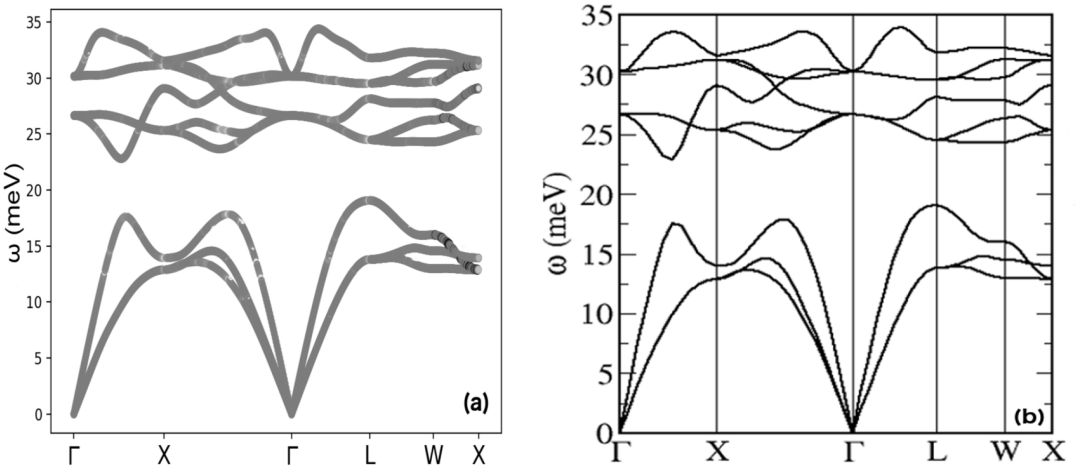

Fig. 3.3 Phonon dispersions plots of a)unfolded phonon dispersion of a 2x2x2 supercell of the TiNiSn primitive fcc unit cell and b) phonon dispersion of the primitive cell of TiNiSn.

Phonon Unfolding

The phonon unfolding has been performed using the Phonon Unfolding Fortran 90 code [91], which uses a generalised projection algorithm. The algorithm projects phonon polarization vectors onto a set of plane waves, in order to compute the unfolding weight. This allows for visualisation analysis of the complex supercell phonon dispersions as the unfolding weight now corresponds to the desired primitive cell Brillouin zone path. An unfolded phonon dispersion for the TiNiSn supercell can be seen in Figure. 3.3a.
The unfolded phonon dispersion now shows agreement with the primitive cell phonon dispersion in Figure. 3.3b. This is evident as the primitive TiNiSn contains only 3 atoms and therefore three acoustic and six optic modes that are now clearly seen on the plot as well as displaying the same frequencies for each mode.

3.1.7 Lattice Thermal Conductivity

As described in Chapter. 2.5.1, one theoretical approach to computing the lattice thermal conductivity, κ_l is through solving the phonon Boltzmann transport equation. This has been done by using the ShengBTE [48] code. This program can compute the mean phonon scattering time, mode Grüneisen parameter, relaxation time, and of course the lattice thermal conductivity for a chosen range of temperatures. The ShengBTE code aims to improve on some limitations of using a relaxation time approximation [92], by solving the Boltzmann transport equation iteratively.
The ShengBTE code requires the knowledge of both the second-order and third-order force constants. As it is only through the addition of anharmonicity in the way of third-order force constants that a finite κ_l may be obtained. The second-order force constants can be obtained using CASTEP as described in Section 1.1.6. Then with the help of a script, *castep2shangbte.py*, the CASTEP output files can be read to generate a set of second-order force constants as a CONTROL file with the required input parameters for the ShengBTE

calculation. This file attempts to provide the correct default input parameters but needs to be edited accordingly. This involves testing and converging the ShengBTE integration grid, adding the desired temperature range as well additional information such as the Born effective charges. In addition, the parameter *scalebroad*, which controls the level of Gaussian smearing to attempt in achieving a speedup in computational time and is set to 1 by default. This ensures the agreement of theory, but it is possible to reduce this parameter can be tested and often reduces the computational expense without sacrificing accuracy.

Third-order Force Constants

The final missing component to compute the thermal conductivity is to obtain the third-order force constants. This can be done using the finite-displacement method using the information about the forces. This is facilitated with the help of a script called *thirdorder.py* [48], which is part of the ShengBTE distribution. The code reads in a relaxed atomic configuration and generated a set of pair displacements. Taking into consideration the symmetry of the system in order to make sure the set of displacements is unique to reduce the computational expense. The code will prepare all of the necessary displaced cells to be calculated. As we are yet again computing the forces on the atoms to construct the now anharmonic force constant matrix, we can use CASTEP again to do so. Here a high level of convergence tolerances is required. The *thirdorder.py* code can then gather all of the data to construct the anharmonic force constant matrix and prepare the third-order constant file in the format required by the ShengBTE calculation.

3.2 Experimental Methods

3.2.1 Inelastic neutron scattering vs *ab initio* phonon DOS

In this work, the phonon density of states were obtained using powder inelastic neutron scattering experiments measured using the MARI chopper time-of-flight spectrometer [106]. The MARI instrument covers a large energy range and achieved good experimental resolution, making it a good choice for measuring the density of states. The Fermi chopper produces a monochromatic neutron beam that scatters neutrons at the sample, then an array of detectors is used to compute the energy transfer. A schematic of the spectrometer design can be seen in Figure. 3.4, showing the beam line and spectrometer set-up. Utilising the incoherent one-phonon approximation to ignore correlation effects between the motions of atoms, we can compute the one-phonon incoherent scattering function S(Q,E) [107]. This scattering function is related to the phonon generalised density of states, $g^n(E)$ and can be written as [108]:

$$g^n(E) = A\langle \frac{e^{2W_k(Q)}}{Q^2} \frac{E}{n(E,T) + \frac{1}{2} \pm \frac{1}{2}} S(Q,E) \rangle, \tag{3.4}$$

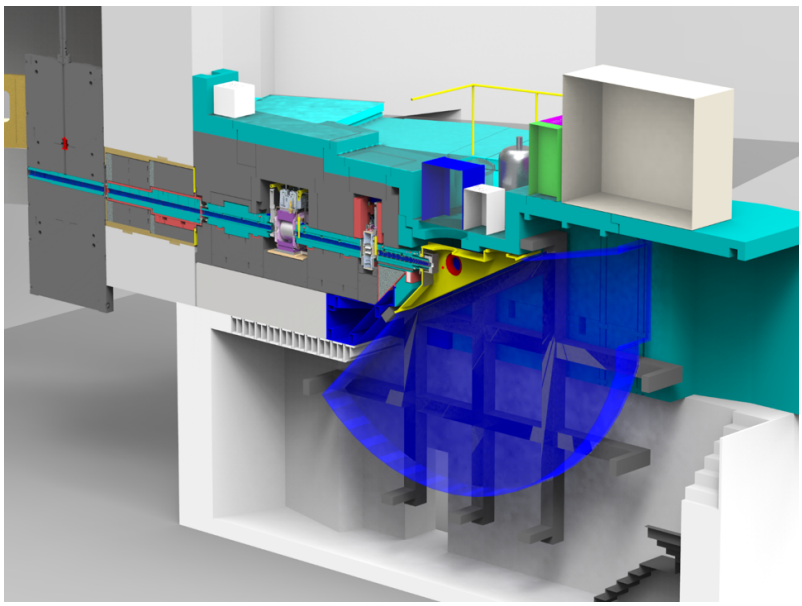

Fig. 3.4 A CAD drawing of the MARI chopper spectrometer. Image received from [8]

where $2W_k(Q)$ is the Debye-Waller factor, Q is the momentum transfer, E is the energy transfer, A is a normalisation constant and $n(E,T) = [e^{E/k_bT} - 1]^{-1}$ and the plus or minus signs are determined by energy loss or gain of the neutrons.
However, in order to compare the phonon DOS from experimental neutron scattering data against the CASTEP theoretical phonon DOS, both data sets need to be post-processed. The raw scattering data is reduced and processed using the Mantid software [109], a python script was used to compute the scattering function of $S(Q,E)$. Finally, it then computes the phonon DOS, $g^n(E)$. Here care should be taken to choose an appropriate energy binning, which should start at a few meV above zero as noise originating from the instrumental resolution dominates at very low energies. On the other hand, CASTEP can compute the partial phonon density of states, $g_k(E)$ for the k^{th} atom in the unit cell. To connect the theoretically computed DOS with an experimental result requires a formalism with the following relationship[108].

$$g^n(E) = \sum_k \frac{4\pi b_k^2}{m_k} g_k(E), \tag{3.5}$$

where b_k and m_k are neutron scattering length and the mass of the k^{th} atom in the unit cell. The neutron scattering lengths were obtained from the NIST database[110].
In addition to this, the CASTEP data has to then be broadened according to the experimental resolution function, which has been computed using a Python script, which is provided as one of the many scripts within the Mantid project [109]. The broadening data and the CASTEP DOS data were combined and plotted using a custom-made Python script.

Chapter 4

Computing lattice thermal conductivity of defective supercells

4.1 Background

This chapter will investigate XNiSn (X = Ti, Zr, Hf) based compositions. This is a class of non-toxic, relatively abundant, and cost-effective materials, when compared to the benchmark thermoelectrics, such as Bi_2Te_3 or PbTe [111]. Half-Heusler compositions are known to have large power factors, but the challenge lies in the optimisation of the relatively high κ_{lat}. This has limited their thermoelectric performance, achieving maximum reported thermoelectric ZT values of around 1.5 with doping [112]. As the ZT value is given by the equation, $ZT = S^2\sigma T/\kappa$, where S is the Seebeck coefficient, σ is the electrical conductivity and κ is the thermal conductivity. We can then see that the aim of optimising thermoelectric properties lies in reducing κ, maintaining as high values of S and σ as possible.

Various approaches with the aim to find mechanisms for reducing κ_{lat} in the aforementioned thermoelectric materials have been undertaken. It is known that the largest contribution to the thermal conductivity in these materials stems from the κ_{lat} and not the electronic component of the thermal conductivity. One of the main attempts for achieving this is through X-site substitution with heavier atoms in order to reduce κ_{lat} through mass-disorder[24]. Moreover, different synthesis and preparation techniques aim to reduce the grain size [113], which has a significant effect on lowering the κ_{lat} as it will be evident from the results in this chapter when incorporating grain boundary scattering with a theoretical model and comparing against experimental data. Additionally, the introduction of interstitials into the half-Heusler matrix provides an alternative route to increase scattering. The most unique structure which encompasses this mechanism is TiNiSn and can be synthesised to contain a significantly larger number of interstitials ($\sim 10\%$), as opposed to the half-Heuslers composed of the heavier ZrNiSn and HfNiSn where the maximal interstitial content is around ($\sim 2-3\%$) in identical preparation conditions. In addition, interstitials in this class of half-Heuslers have experimentally

shown a significant reduction in κ_{lat}, resulting in values of around 4.5 W/mK at around 5% filling of the half-Heusler vacancy sites compared to $\sim 13 W/mK$ in the stoichiometric compositions at an assumed grain size on the order of a few microns. The magnitude of this reduction warrants an investigation of the vibrational spectra in order to exploit this effect for further potential optimisation of the thermoelectric properties, which is the key focus of this chapter.

To begin such an investigation, the first task was to compute the vibrational spectra of stoichiometric compositions XNiSn($X = Ti, Zr, Hf$). This is done as to benchmark the level of theory and parametrisation required to obtain agreement with previous theoretical and experimental results. Moreover, it enables to lay a foundation describing the nature of the phonons without the presence of any defects in the structure. Secondly, we then investigate the effect of interstitials on the nature of the phonon modes and the phonon density of states. The added complexity due to the use of supercells required to model the defective structures makes it difficult to directly compare the phonon dispersion to that of the stoichiometric parent compound. Therefore, a method for unfolding the phonon dispersion back onto the primitive cell BZ has been deployed. In addition to this, together with my experimental collaborator Duc. Le, we have performed an inelastic neutron scattering experiment on powder samples on the MARI spectrometer at Harwell. The beam time proposal, sample synthesis and material characterisation were led by Jan-Willem. G. Bos and Donald. A. MacLaren. The interstitial Ni or Cu content present in the sample was guided as to match closely with the theoretical simulations when preparing the samples. Post-processing of the data using a theoretical framework was used to allow for a direct comparison of the computed and measured phonon density of states, taking into account neutron scattering cross-sections and experimental resolution to gain insight into the effects of interstitials. In this section, we highlight the impact of various arrangements of vacancy site filling on the phonon DOS. The experimental results together with robust testing of the simulations serves as a validation of the model and results. Finally, we compute the lattice thermal conductivity of TiNiSn and $TiNi_{1.125}Sn$ through iteratively solving the phonon Boltzmann Transport equation as implemented in the ShengBTE code [114]. The results are compared to available experimental data as we have not come across previous attempts of obtaining the κ_{lat} for defective structures which originate from a supercell model. Here, we also include the effect of additional scattering due to grain boundaries. In addition, I have used a simpler model, namely the modified Debye-Callaway model of thermal conductivity [54] in an attempt to reduce what turned out to be a prohibitive computational expense, when trying to compute the κ_{lat} of defective compositions with interstitials at the required convergence criteria in systems with clustered defects due to reduced symmetry in the system. Both models were bench-marked against experimental data of stoichiometric TiNiSn.

4.2 Computational Details

4.2.1 Second order vibrational spectra calculations

Phonon calculations were performed using the CASTEP first principles simulation package [51]. Calculations used the Perdew-Burke-Ernzerhof (PBE) generalized gradient approximation (GGA) as the exchange-correlation functional as well as an ultrasoft pseudopotential set (C18), which was generated on-the-fly, with CASTEP version 18.1. Convergence parameters for the plane-wave cut-off were determined to be in the range of 600-800 eV with a grid scale of 2.0 and a fine grid scale set to 3.0. The **k**-point sampling was performed on a $4x4x4$ Monkhorst-Pack grid. This corresponds to a total energy convergence of 0.5 meV per atom or better. A primitive face-centered-cubic (fcc) cell containing 3 atoms was used for the stoichiometric compositions. Whereas the supercell approximation was used in calculations for the defective compositions with interstitials. The supercell was a $2x2x2$ multiple of the primitive fcc cell and contained 24-25 atoms. To achieve the required periodicity for the clustered interstitial Ni case in $TiNi_{1.125}Sn$ a larger $2x2x2$ supercell of a cubic unit cell containing 100 atoms was required. Structural relaxation was performed using the LBFGS [99] optimization method as implemented in CASTEP. The force and stress convergence for the geometry optimisation were 0.03 eV/Å and 0.05 GPa respectively for obtaining the phonon dispersion and phonon DOS. A $4x4x4$ phonon **q**-point grid was used along with Fourier interpolation to obtain the dynamical matrix. This was sufficient to obtain high quality forces for the phonon dispersion and DOS calculations. This level of convergence translated to a phonon frequency convergence of 1% or better. The unfolded phonon dispersion for the relaxed structure was calculated along the $\Gamma - X - \Gamma - L - W - X$ path in the primitive Brillouin zone using the same convergence parameters as for the structural relaxation. The phonon DOS was calculated on a fine $30x30x30$ Monkhorst-Pack grid. Finally, the neutron weighted DOS was calculated using a custom made script. Implementing the same theoretical framework as the one which can be found in Section. 3.2.1. This script also made use of the *pychop.py* script, which is part of the Mantid software package [109], allowing for the computation of the energy dependent experimental resolution function used in the broadening of the phonon DOS. The graphical representation of the data was plotted using the dispersion.pl [51] script that is a part of the CASTEP package as well as matplotlib [115].

4.2.2 Lattice thermal conductivity calculations

The lattice component to the thermal conductivity was computed through iteratively solving the phonon Boltzmann transport equation (BTE), using the ShengBTE code [114]. To do so, the code requires both the second order interatomic force constants (IFC), which is the IFC matrix found within the harmonic approximation. As well as the third order IFC's to compute the anharmonic contributions to thermal conductivity. Second order

Table 4.1 Convergence of forces and their effect on computed κ_{lat}.

Force Tol. (eV/Å)	Energy Tol. (eV)	$\kappa_{lat}(\mathrm{W/mK})$
4 x 10^{-4}	1 x 10^{-10}	0.43
2 x 10^{-7}	8 x 10^{-13}	0.81
6 x 10^{-11}	1 x 10^{-14}	0.82

force constants were obtained using CASTEP, implementing the finite displacement, non-diagonal supercell method [85]. This method also helped to reduce the computational cost in comparison to the standard finite displacement method implementation as found in CASTEP by computing the required phonon q-points on a set of smaller supercells. The calculations used the PBE-GGA exchange and correlation functional and the same C18 "on-the-fly" pseudopotential set, with the same energy cut-off and **k**-point grid mesh as for the second order calculation. However, when computing the κ_{lat} even at this level of convergence the error in the forces can lead to spurious results. Therefore, the force convergence tolerance for obtaining both the second order and third order force constants was subsequently tightened to $< 2\text{x}10^{-7}$ eV/Å and the energy per atom convergence tolerance was increased to $1\text{x}10^{-12}$ eV. A test was performed using a smaller $2x2x2$ phonon **q**-point grid at varying force and energy tolerances before performing the final set of second and third order force constant calculations. The convergence can be seen in Table 4.1.

A script called *castep2shengbte.py* [116] was used to post-process the CASTEP outputs and save the data in ShengBTE's format for the second order IFC's. Computing the third order force constants matrix required a set of supercells with pair displacements to obtain the full anharmonic force constant matrix. A script called *thirdorder.py* was used to help find and generate an irreducible set of displaced supercells [114]. In the case of the stoichiometric TiNiSn a $4x4x4$ supercell was created, taking into account all interactions up to the third nearest neighbour. This supercell contained 192 atoms, requiring 320 displaced supercells and thus 320 self-consistent CASTEP jobs to compute the forces. On the other hand, extracting the third order IFC's in the the defective $TiNi_{1.125}Sn$ model required a $2x2x2$ supercell of the 25 atom primitive cell, resulting in a supercell containing 200 atoms. There were 904 jobs required for the calculation of forces. As the simulation cell was larger a smaller $1x1x1$ **k**-points sampling grid was needed to converge the total energy. The ShengBTE code requires an additional convergence parameter for it's own integration grid. This was found to be $16x16x16$ for both compositions. In addition, the Gaussian smearing parameter, *scalebroad* was kept at the maximum value of 1.0. Lastly, the effect of grain-boundaries was included as a post-processing step as ShengBTE only computes the intrinsic component of κ_{lat}.

To compute the lattice thermal conductivity using the modified Debye-Callaway model, the mDCThermalC [54] code was used. The code required inputs in the Phonopy format [55] of both the second order IFC's as well as mode Grüneisen parameters. Phonopy generated the

required second order displaced cells, but the *ab initio* force calculations were performed using CASTEP [51]. As for the mode Grüneisen parameters, three separate simulations were required to obtain these. One relaxed equilibrium structure and two strained cell calculations which were altered by adding small deviations away from the equilibrium lattice parameters. The strained cells were then relaxed under constrained volume. Finally the lattice thermal conductivity was sampled for a desired set of temperatures.

4.2.3 Experimental details

The elemental powders used to synthesise the samples were purchased from Alfa Aesar and have a purity $> 99.5\%$. Synthesising the samples involved grinding the elemental powders using an agate pestle and mortar, cold pressing and sintering at 1123K for 24 hours, followed by 14 days of annealing. The phonon DOS of the experimental samples was measured using the MARI time-of-flight chopper spectrometer. The powder samples were placed in a vanadium can and placed inside the instrument. Measurements were taken for each powder sample as well as a final measurement of the empty vanadium can under the same experimental conditions. The empty can measurement allows to subtract the DOS of the vanadium can from the sample DOS. The instrument was set to an incident energy of 60meV at a temperature of 300K. The choice of Fermi chopper used was the "sloppy" chopper, with an energy resolution of $3-8\%$ that is dependent on the choice of chopper, incident energy and energy transfer. The data reduction and vanadium can subtraction was performed with the help of the Mantid software [109]. The background corrected data was summed over a $\mathbf{Q}$ range of $0-10$ Å^{-1}.

4.3 Stoichiometric XNiSn (X = Ti, Zr, Hf) compositions

TiNiSn, ZrNiSn and HfNiSn are half-Heusler alloys with a XYZ (X = Ti, Zr, Hf) type composition. The atoms form an fcc crystal structure formed via three interpenetrating fcc sublattices, where the space group is $F\bar{4}3m$ (216). The X element is found at the Wyckoff position 4a (0,0,0), Ni is at the position 4c $(\frac{1}{4},\frac{1}{4},\frac{1}{4})$ and Sn is at the position 4b $(\frac{1}{2},\frac{1}{2},\frac{1}{2})$. Vacancies are present at the Wyckoff position 4d $(\frac{3}{4},\frac{3}{4},\frac{3}{4})$. A graphical representation of TiNiSn can be seen in Figure 1.4. This is a unique composition as even though there are metallic constituents, the resulting structure forms an 18 electron closed shell system.
In addition, I have tabulated the computed and known experimental lattice parameters for some of the key compositions found in this chapter in Table. 4.2. We can see that the X-site substitution leads to an intermediate lattice parameter between the TiNiSn and ZrNiSn lattice parameters, which is perhaps an unsurprising result. Whereas, it can be seen that the introduction of interstitials into the half-Heusler matrix results in a small increase in the lattice parameter. There is a strong agreement between the known experimental lattice parameters and the computed values to within 0.5% or better which is expected when

using the PBE exchange-correlation functional. The structural relaxation was performed with respect to both the cell parameters and internal co-ordinates.

Table 4.2 Equilibrium lattice parameters in computed and experimentally measured stoichiometric and defective half-Heuslers.

Structure	Lattice Param(Å)	Exp. Lattice Param(Å)
TiNiSn	a = 5.942	a = 5.9298[117]
ZrNiSn	a = 6.140	a = 6.1089[117]
HfNiSn	a = 6.112	a = 6.0795[117]
$Ti_{0.5}Zr_{0.5}NiSn$	a = 6.048	a = 6.0385[117]
$TiNi_{1.25}Sn$	a = 5.996	a = N/A
$TiNi_{1.125}Sn$	a = 5.974	a = N/A
$TiNiCu_{0.125}Sn$	a = 5.981	a = N/A

When attempting to analyse and understand the properties of thermoelectrics, one of the crucial starting points is to first obtain and interpret the nature of the phonons. Initially, we begin by analysing the phonon dispersion of the stoichiometric materials before attempting to investigate the more complex defective counterparts. The phonon dispersion is invaluable at revealing many key characteristic features of vibrations. Hence, here we begin by presenting the results of the computed phonon dispersions as seen in Figure 4.1.

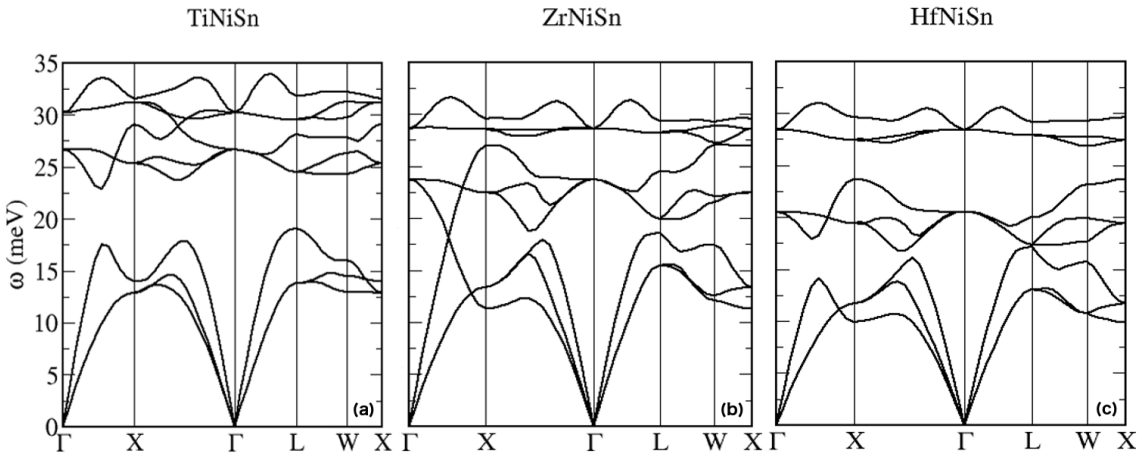

Fig. 4.1 Phonon dispersions of a) TiNiSn, b) ZrNiSn and c) HfNiSn. The phonon dispersion is plotted along the $\Gamma - X - \Gamma - L - W - X$ high symmetry directions through the primitive cell BZ. The plots illustrate the qualitative similarities between the compositions and the effect of increasing mass on lowering the phonon frequencies.

Analysing the phonon dispersion there were no imaginary frequencies found suggesting that the structure is stable and no symmetry breaking is predicted via a displacive phase transition caused by a "soft" or "frozen" phonon mode[118]. At first glance TiNiSn, ZrNiSn and HfNiSn have similarly shaped phonon dispersions as seen in Figure 4.1.
On the other hand, there is a clear reduction in the phonon frequencies as the mass of the X-site atom increases from Ti through to Hf. This change in frequencies is also accompanied by a closing of the largest energy gap in TiNiSn between 17-23meV beginning to close for ZrNiSn and eventually closing in HfNiSn. Instead, opening up a new gap in the higher

frequency optical branches. In addition, some parts of the dispersion show band crossing as in ZrNiSn going from Γ to X in the Brillouin zone. Meaning that at those points phonons can undergo a transition from the acoustic to optic mode at no extra momentum cost. Due to the fact that the finite displacement method was used for the calculations along with the ultrasoft pseudopotential set, the non-analytic correction has not been applied by default. However, effects of LO-TO splitting have been previously investigated [24] where the effect on the high frequency optic modes can be seen, and are therefore not investigated in this chapter. The qualitative similarities allow for isoelectronic substitution of the Ti, Zr, and Hf atoms to be laid out as an optimisation problem to provide one way of lowering the thermal conductivity without dramatically altering the nature of the phonon dispersion.

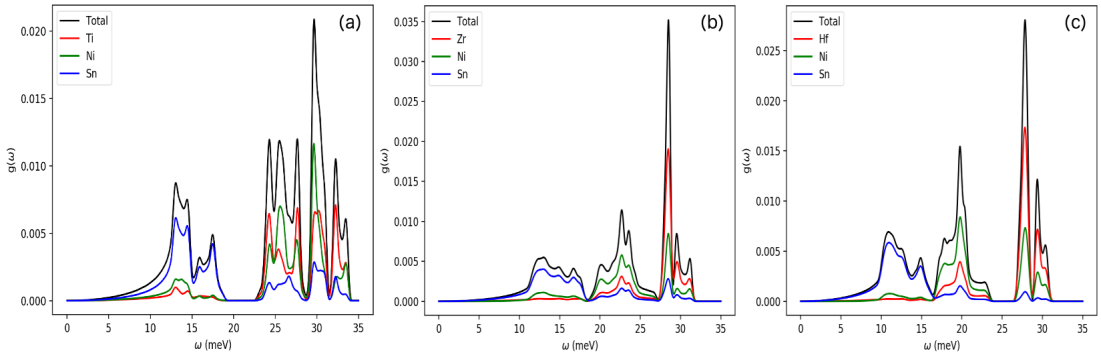

Fig. 4.2 Phonon partial DOS of a) TiNiSn, b) ZrNiSn and c) HfNiSn. The total phonon DOS is shown by the black solid line. The contributions from the individual species are identified by a different colour as indicated in the legend box for each plot. The plots illustrate the low and high frequency modes being dominated by heavy and light atoms respectively.

However, the biggest difference can be seen in Figure 4.2. These show the partial phonon density of states with respect to each species. There is a clear difference for the heaviest atoms taking over the dominant portion of the acoustic phonon contribution at low frequency, for TiNiSn and ZrNiSn this is the Sn atoms. Where as in HfNiSn, the Hf atoms are now the heaviest and most dominant in this frequency range. Since, the low frequency modes tend to carry the most of the contribution to the thermal conductivity, and mass-disorder scattering effects mostly the high frequency range, it is expected that at low temperatures where the phonon mode occupation in the optical range is lower, the effect of mass-disorder scattering will become less sensitive to temperature change after some particular substitution concentration as well as not being the optimal scattering process for lowering thermal conductivity. A study has performed calculations within the virtual crystal approximation and has shown that the most effective reduction occurs up to concentrations of around 10%[24]. To gain some additional insight on the effect of such a substitution. I have computed the vibrational spectra for a binary substitution of the X-site of the $Ti_{0.5}Zr_{0.5}NiSn$ composition, which was modelled using a $2x2x2$ supercell of the fcc

primitive cell, where half of the eight X-site Ti atoms were pseudo-randomly replaced with Zr atoms.

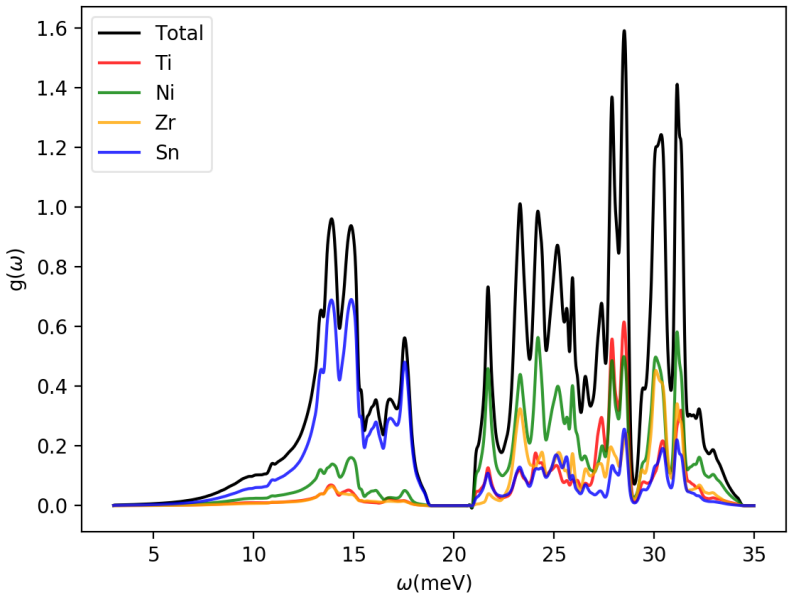

Fig. 4.3 Phonon partial DOS of $Ti_{0.5}Zr_{0.5}NiSn$. The total phonon DOS is shown by the black solid line. The contributions to the total DOS from the individual species are represented by a different colour as indicated in the legend box for each plot.

The effects of the substitution show the expected down shift of phonon frequencies compared to that of the stoichiometric TiNiSn due to the fact Zr is a heavier element. This is why the heaviest Sn atoms still maintain the largest contribution to the DOS at low frequencies. With the largest changes to the individual species being seen for Ni, particularly the peaks present at around 22-24meV. One might assume that since the X-site elements do not have the largest contribution at low frequencies, there will not be a significant reduction in available states for a reduction in κ_{lat}. However, from experimental measurements, a significant reduction is observed. This can be explained by the fact that the whole frequency range contributes to the thermal conductivity, but there needs to be a way to effectively scatter the acoustic phonons as they are our majority carriers for our compositions in question. In fact, a promising way is through boundary scattering. This mechanism assumes that if the grain size in the crystal can be engineered to a specific size that is of a similar scale to the phonon mean free path then boundary scattering will become significant and thus increase thermal resistivity, consequently lowering the thermal conductivity. In the literature there seems to be a large spread of reported grain sizes in produced samples. Ranging from a few micrometers to grain sizes as small as 50nm [119] depending on the processing techniques being used. In the next section, I investigate the thermal conductivity at various grain sizes using a theoretical model, and the effect of this is shown for TiNiSn and $TiNi_{1.125}Sn$ in order to further understand the underlying mechanisms for lowering thermal conductivity.

4.4 Modelling vibrational properties

4.4.1 Interstitial Ni, clustered vs homogeneous defect models

A topic that is more of a mystery and requires more in depth knowledge for these materials is the effect of interstitial defects and how these defects are distributed within the crystal. It is known that there is solubility within TiNiSn that allows for around 10% excess Nickel to enter the structure. Studies investigating defect formation energies found Ni interstitials to be one of the favourable point defect configurations in terms of stability [120]. In addition, experimental measurements of Ni rich TiNiSn have shown a significant reduction in the thermal conductivity at low temperature measured at $4-4.5W/mK$ [121, 1]. A literature study has attempted DFT calculations on small supercells and varied the spacing of the intersitial Ni atoms to try and shed some light if the Ni should be found in clusters of neighbouring 4d site vacancies, closely resembling a full-Heusler $TiNi_2Sn$ inclusions or if the Ni has a random statistical distribution. They have concluded that it is indeed the clustering scenario which appears to be lower in energy and therefore preferred [121]. They did not however perform local studies of the structure, which my collaborators are in fact investigating using electron microscopy techniques. Previously, due to the promising nature of the nano-inclusions, they have investigated this possibility and found no full-Heusler interstitial nano-inclusions[122] with only half-Heusler grains with interstitials of full-Heusler grains present. Instead, they have determined that there must be multi-phase behaviour and effect on thermal conductivity might come into effect on the microstructure scale. An interesting observation lies in the fact that the synthesis route for $TiNi_{1+x}Sn$ requires the reactants to indirectly transition from the full-Heusler to the half-Heusler phase. This is different for the $ZrNi_{1+x}Sn$ and $HfNi_{1+x}Sn$ compositions, which can be directly synthesised as half-Heuslers. This allows for a stronger possibility for a non-random distribution of the Ni atoms in the vacancy sites.

To investigate this, I have prepared simulations where the Ni interstitials have been placed in two different configurations. One aiming to model a pseudo-random statistical distribution of interstitials, where the defect-defect distance is kept constant. Whereas, the second simulation cell includes clustering of Ni interstitials, based on findings of previous work considering energetics of different Ni clustering configurations in defective ZrNiSn [123]. As the $2x2x2$ supercell includes eight primitive cells. The defects were placed to include a cluster of three out of four 4d site vacancies being filled within one of the eight primitive sub-cells and the final Ni interstitial being placed further away from the rest. There are multiple choices of distances for the final Ni atom and my calculation considers one configuration, which is an intermediate and not the maximal achievable separation of the interstitials when taking into account the periodicity of the simulation cell.

A visual representation of example simulation cells for both cases can be seen in Figure 4.4. Modelling the pseudo-random Ni interstitial was possible using a smaller 25 atom supercell of the fcc primitive cell, which enabled to reduce the computational expense.

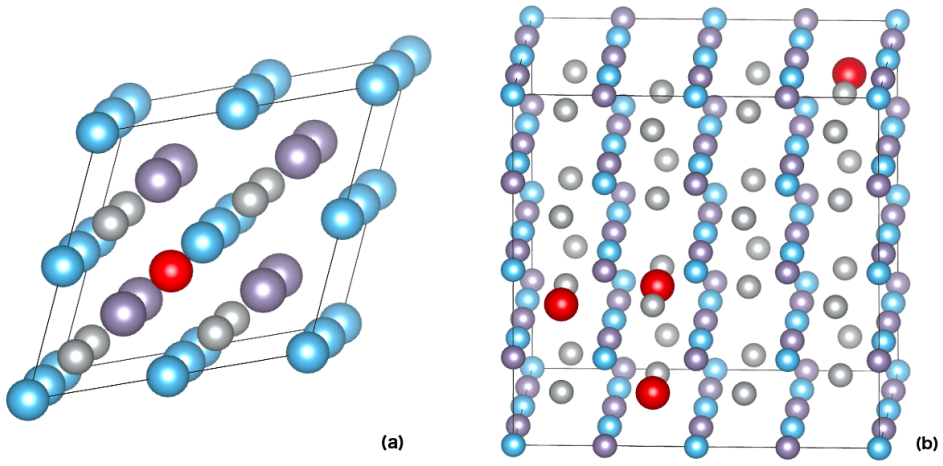

Fig. 4.4 $TiNi_{1.125}Sn$ simulation cells of a) pseudo-randomly distributed defect in a $2x2x2$ supercell of the fcc primitive cell and b) 3-1 clustered Ni interstitials and one separated Ni interstitial in a $2x2x2$ supercell of the fcc conventional unit cell. The colours of the atoms correspond to Ti (blue), Sn(purple), Ni (gray) and Ni defect atoms (red). The size of the atoms for the cubic supercell has been adjusted to highlight the defect atoms.

However, achieving the required configuration for the clustered model called for a larger 100 atom supercell in the cubic fcc unit cell to achieve the desired arrangement of Ni interstitials.

Analysis was performed by computing the neutron weighted (NW) phonon DOS for both models. This enabled a direct comparison with the collected experimental data, which was performed on powder samples of TiNiSn and $TiNi_{1.1}Sn$ using the MARI instrument.

Before tackling the question for the choice of model of interstitial defects, we can take a look at the experimental data in Figure. 4.5, displaying the phonon DOS and error bars. Here we can see the differences in the DOS between the samples. We can see that there is significant DOS present around 20meV for all three samples. Comparing TiNiSn against $TiNi_{1.1}Sn$, we can see there are statistically significant broadened shoulders for $TiNi_{1.1}Sn$ both in the low-frequency range from 5-12meV as well as in the intermediate range of 14-21meV. Albeit, no significant new peaks in the DOS can be seen. In the case of $TiNiCu_{0.1}Sn$, the broadening is less pronounced in the low energy range, but additional DOS can be seen. A slight downshift in the peaks can be seen, likely due to the slightly larger mass of Cu compared to Ni.

In order to then compare the choice of interstitial defect model, phonon DOS for both the homogeneous and clustered Ni interstitial models were computed. The results for both models were plotted against the experimental data, this can be seen in Figure 4.6 (a) and (b) respectively. An additional 5% scaling has been applied to the computed phonon frequencies, this is done due to the known underestimation of the strength of the forces by the PBE functional [124]. We can immediately notice that the calculated DOS for the homogeneous defect is almost zero around the $20-23meV$ range. This is in disagreement with the experimental result and it can be seen that only the clustered model manages to correctly capture this energy range. Although, the DOS does not seem to reveal a single

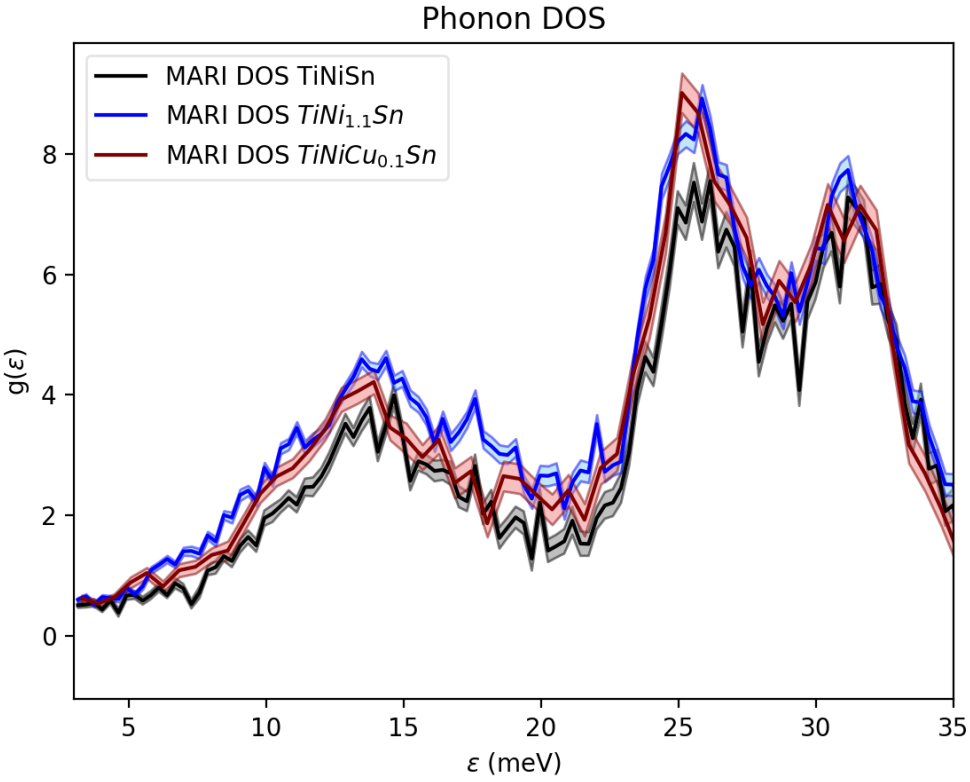

Fig. 4.5 Experimental phonon DOS for stoichiometric fcc primitive cell of *TiNiSn* plotted against the experimental phonon DOS of $TiNi_{1.1}Sn$ and $TiNiCu_{0.1}Sn$. The shaded regions correspond to error bars.

large new peak, it instead displays a clear broadened shoulder in the $14-23$ meV range. I believe this intermediate range broadening is a significant factor in lowering the κ_{lat} and this will be discussed later. It should also be noted that the experimental DOS does not tend to zero at energies $< 5meV$, this is simply an artefact of the limitations of the spectrometer. In addition, what appears to be a peak developing at around 8 meV in Figure 4.6 (a) appears broadened in the clustered case and is not reflected in the experimental DOS.

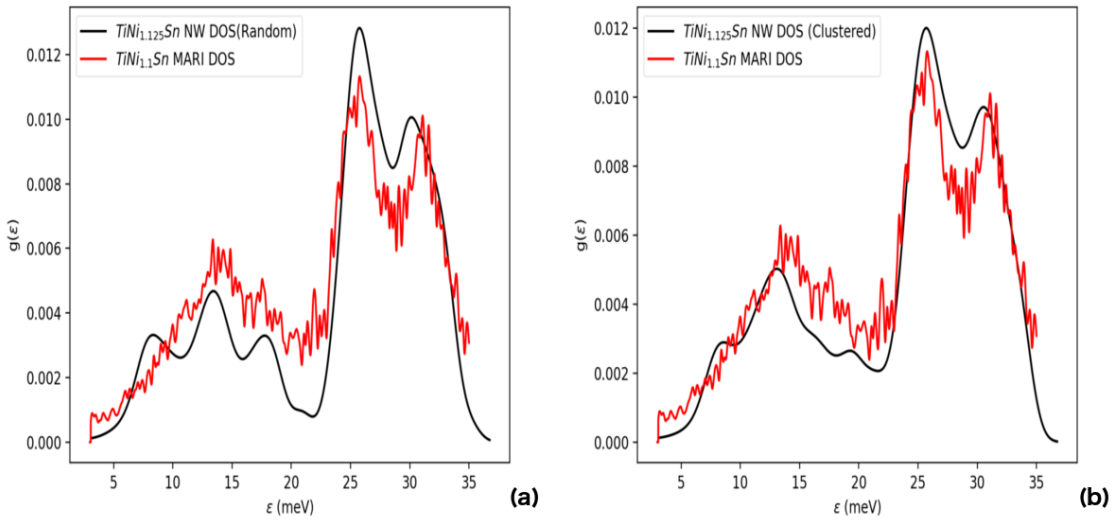

Fig. 4.6 Theoretical vs experimental phonon DOS for a) pseudo-randomly distributed defect in a $2x2x2$ supercell of the fcc primitive cell of $TiNi_{1.125}Sn$ and b) 3-1 clustered Ni interstitials and one separated Ni interstitial in a $2x2x2$ supercell of the fcc conventional unit cell. The experimental phonon DOS result is plotted for $TiNi_{1.1}Sn$.

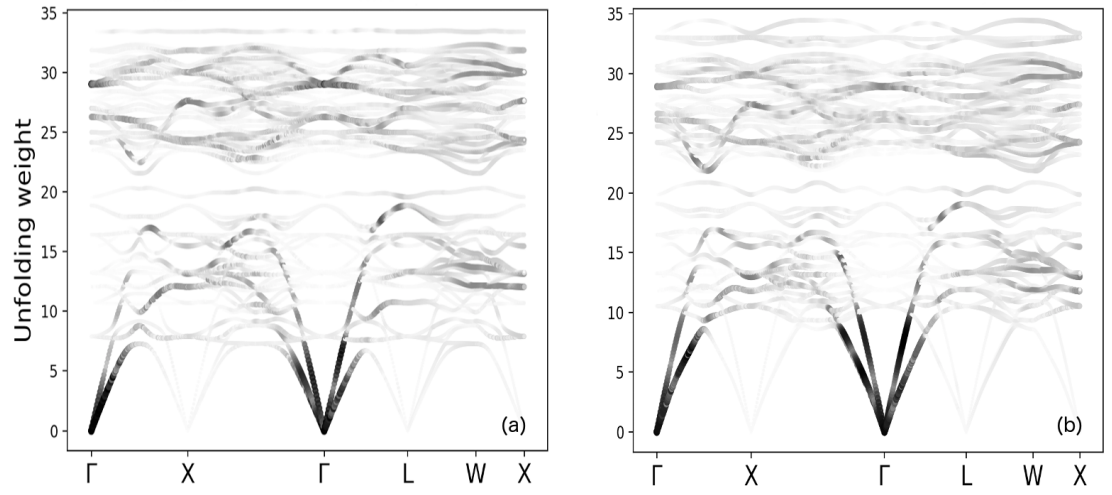

Fig. 4.7 Unfolded Phonon dispersion for a) $TiNi_{1.125}Sn$ and b) $TiNiCu_{0.125}Sn$. Plotted along the $\Gamma - X - \Gamma - L - W - X$ high symmetry directions through the primitive cell BZ. Where the gray-scale intensity bar represents the unfolding weight.

4.4.2 Interstitial Cu defect

Since I have obtained unfolded phonon dispersion curves for the supercell calculations, we can also make a direct comparison between the phonon dispersion and the phonon DOS. The unfolded phonon dispersions for $TiNi_{1.125}Sn$ and $TiNiCu_{0.125}Sn$ are shown in Figure 4.7, where both compositions seem to show a new flat mode around 20meV, which is not present in the stoichiometric compositions.
Continuing the analysis for excess Ni and looking in particular at the low-frequency acoustic modes around the Γ point, we retain the largest unfolding weight and as the frequency increases the unfolding weight is generally lower across the modes in higher frequency regions, suggesting a higher level of broadening. There are low-lying optic modes with a significant weight that can be found at around 8 meV along the $\Gamma - X$ direction. This is in contrast to the stoichiometric TiNiSn, where those modes are not present as seen in Figure 4.1. This suggests additional phonon broadening in the low-frequency region, which would contribute to shorter phonon lifetimes and therefore a reduction in κ_{lat}.

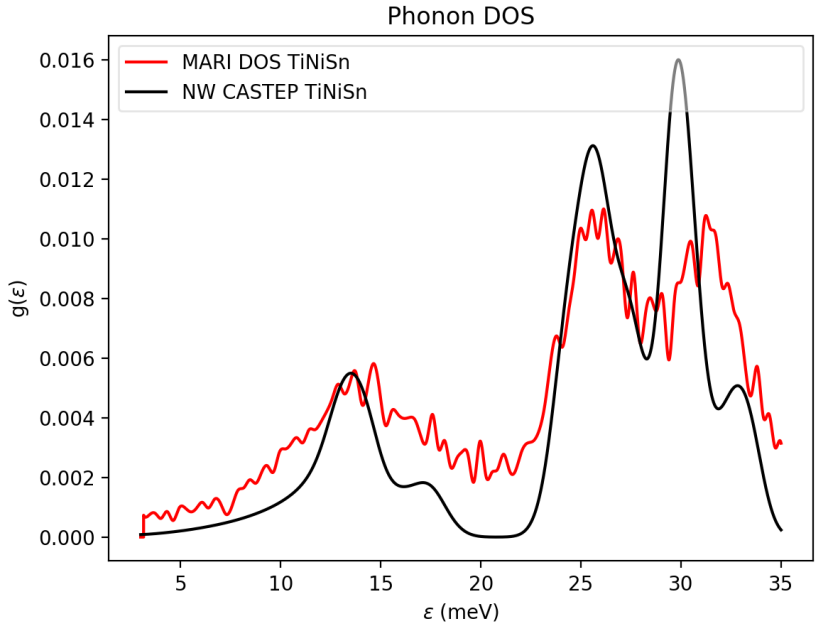

Fig. 4.8 Theoretical vs experimental phonon DOS for stoichiometric fcc primitive cell of TiNiSn plotted against the experimental phonon DOS of TiNiSn.

Naturally, to test the hypothesis of the new agreement in the clustered case, we can try to look at the stoichiometric parent material phonon DOS. This is in fact what can be seen in Figure 4.8. However, here we still have the persistent mismatch at around 20 meV. Nevertheless, what must be kept in mind is that based on tests performed by my collaborators, the stoichiometric samples usually include interstitials at a level of at least 1% as it is very difficult to synthesise a pure sample of TiNiSn due to the synthesis route through a full-Heusler phase. I believe that this level of interstitials could explain why the experimental results differ from the calculated result.

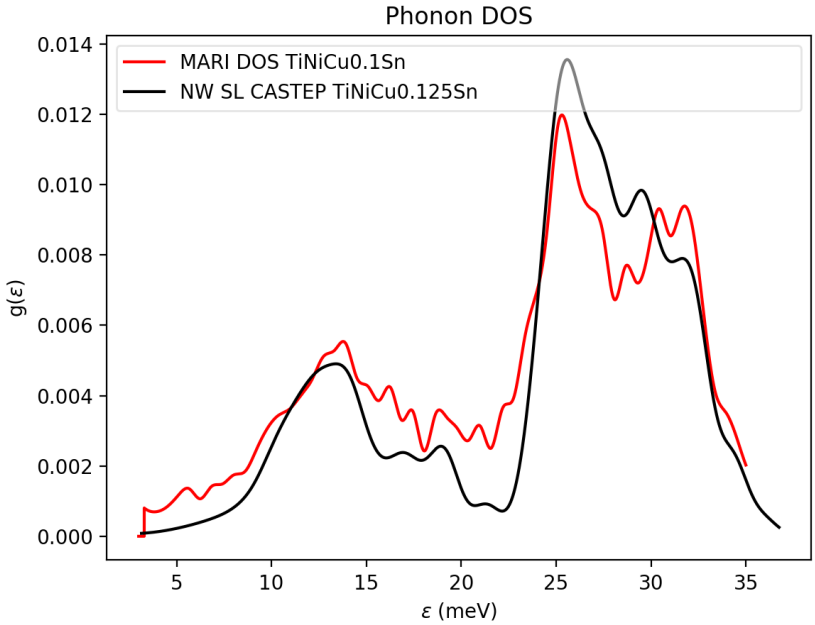

Fig. 4.9 Theoretical vs experimental phonon DOS for pseudo-randomly distributed defect in a $2x2x2$ supercell of the fcc primitive cell of $TiNiCu_{1.125}Sn$ plotted against the experimental phonon DOS of $TiNiCu_{0.1}Sn$.

For the case of Cu interstitials, by comparing Figure. 4.6 (a) against Figure 4.9, we can see that with the homogeneous defect the same mismatch arises in the region of 20 meV. The plots show a comparable level of agreement between the theoretical and experimental phonon DOS as for the stoichiometric case, with the largest shift in frequencies between theory and experiment occurring in the high-frequency regions. What can also be seen is that the computational result with Cu interstitials shows a smoothed DOS in the low acoustic energy range and does not appear to show a peak at around 8 meV as in the case of the model with homogeneous Ni interstitials. It should be noted that once again a 5% scaling factor has been applied to the computed frequencies as it is known that this is the typical DFT error using the PBE functional when computing phonon spectra.
The same trend continues when looking at the results for the experimental phonon DOS of $ZrNi_{1.1}Sn$ and ZrNiSn as seen in Figure. 4.10. Here we can see that in the closing phonon gap seen from the phonon dispersion for the computed ZrNiSn in Figure. 4.1 (b) at around 18 meV, we once again have a phonon DOS present in the experimental result, which is non zero. Synthesised samples usually contain a percentage of interstitials, which deviates from the desired one-to-one stoichiometry that could contribute to the DOS in this region. However, this can also be largely attributed to the fact that the phonon gap present in TiNiSn at around 17-23meV begins to close in the ZrNiSn system as seen in Figure. 4.1. When comparing the composition with 10% of Ni interstitials we do not see clear broadening present in the acoustic region for $ZrNi_{1.1}Sn$, but there is clear broadening in the optic region around the peak at around 29 meV. The interesting point to be made here is that even though it is expected to find some interstitials when

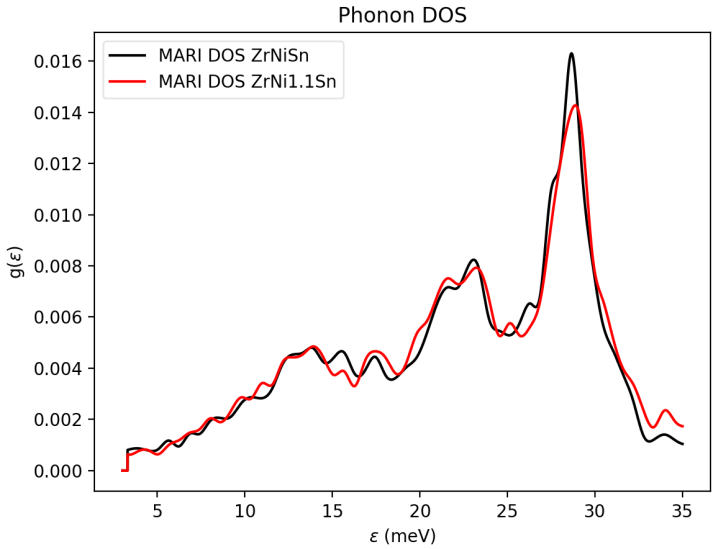

Fig. 4.10 Experimental phonon DOS for stoichiometric fcc primitive cell of ZrNiSn plotted against the experimental phonon DOS of $ZrNi_{1.1}Sn$ defective structure.

attempting to synthesise a defect-free ZrNiSn sample. The synthesis route for the defective compositions of $ZrNi_{1+x}Sn$ is simpler than that for $TiNi_{1+x}Sn$ as the elemental mixture can directly form the half-Heusler phase and not have to pass through a full-Heusler phase in the process. This suggests that interstitial defects in both compounds could have a preference for clustering regardless of the chemical pathway, but the preferential clustering arrangement in both would have to be investigated. Furthermore, my collaborators had prepared additional samples for the MARI INS experiment. Namely ZrNiSn, HfNiSn, $Ti_{0.5}Zr_{0.25}Hf_{0.25}NiSn$, $Ti_{0.5}Zr_{0.5}NiSn$ and $ZrNi_{1.1}Sn$. The plot of the experimental data for these samples can be found in Appendix. A for a further comparison.

4.5 Lattice thermal conductivity

Now we can try to tackle one of the key questions for optimising the thermoelectric performance of our systems, the lattice thermal conductivity. Here, I will present the results for the computationally predicted κ_{lat}, these have been obtained using two different theoretical approaches to provide an additional layer of model testing. Due to the prohibitive computational expense, the clustered defect model for the Ni interstitials was not possible to compute given the time constraints and resources of the project. Therefore results were computed for the homogeneous defect model as this could be achieved using a smaller simulation cell to capture the pseudo-random arrangement of Ni interstitials and reach the required convergence criteria for obtaining the second and third-order force constants. The most computationally demanding calculation for the determination of third-order force constants of the 100 atom $TiNi_{1.125}Sn$ supercell, required over 900 independent DFT calculations parallelised using 54 processors, each running for up to 8 hours.

Table 4.3 Lattice thermal conductivity as well as Grüneisen parameters calculated as a weighted sum of mode contributions for TiNiSn and $TiNi_{1.125}Sn$ at 300K. Computed theoretical values are shown as well as available theoretical and experimental values from the literature.

Structure & Method	κ_{latt}(W/mK)	Grüneisen parameter
TiNiSn (ShengBTE)	13.4	1.7
TiNiSn (Debye-Callaway)	7.9	n/a
TiNiSn (Literature Expt.)	8 [113]	n/a
TiNiSn (Literature Theory)	14.5 [24], 15.4 [125]	n/a
$TiNi_{1.125}Sn$ (ShengBTE)	0.43	2.2
$TiNi_{1.125}Sn$ (Debye-Callaway)	0.24	n/a

The results for the calculated and literature values of κ_{lat} can be seen in Table. 4.3. Calculations obtained through the solution to the linearised phonon Boltzmann transport equation as implemented in the ShengBTE code [114] give the intrinsic part of the κ_{lat} and we can see that the obtained value of $13.4W/mK$ is in good agreement with previous theoretical work [24, 125], however the value is significantly larger than the experimentally obtained results. This can be attributed to the fact that extrinsic scattering effects have not been included. Hence, I have also investigated the effect of grain boundaries using a simple model according to $\kappa_{gb} = \frac{\kappa_{int}}{1+\frac{L_{mpf}}{L_{gb}}}$, where κ_{gb} is the intrinsic lattice thermal conductivity including grain boundary scattering, κ_{int} is the intrinsic lattice thermal conductivity, L_{mpf} is the phonon mean free path, as obtained using ShengBTE and L_{gb} is the size of the grain boundaries. In Figure. 4.11, we can see that lowering the grain size has a significant effect on lowering the κ_{lat} and converges on the experimental results for grain sizes in the order of a few hundred nanometers, with a value of $7.4W/mK$ at a grain size of $1x10^{-7}$ m.

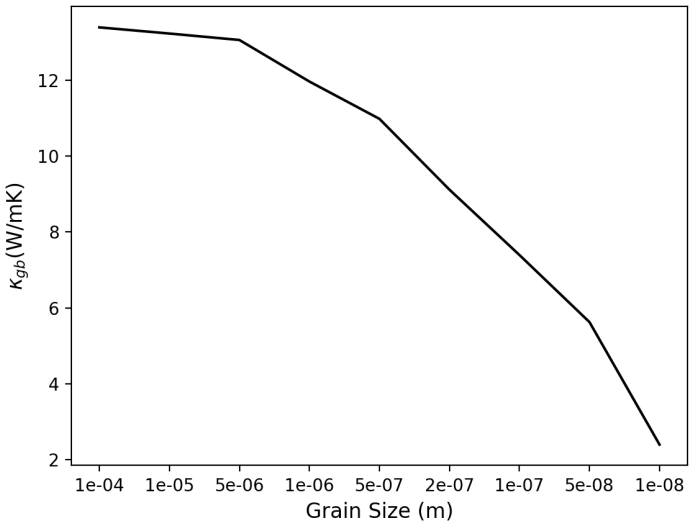

Fig. 4.11 Plot showing the effect of different grain sizes on the computed value of the thermal conductivity for TiNiSn at 300K.

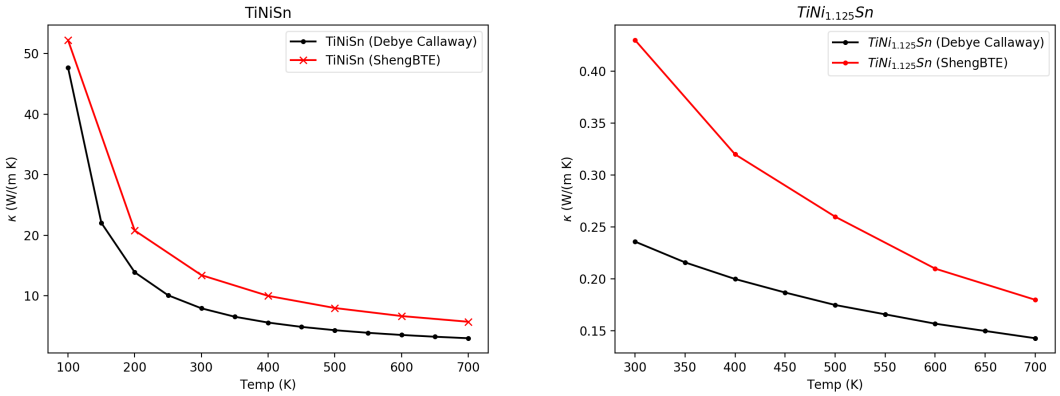

Fig. 4.12 Thermal conductivity of TiNiSn and $TiNi_{1.125}Sn$ plotted as a function of temperature, calculated using the modified Debye-Callaway model (black line) and ShengBTE (red line).

The only experimental values for $TiNi_{1.125}Sn$ are those from measurements taken by my experimental collaborators, which are in the range of 2-4 (WmK) at 300K. Looking at the computed results this is an order of magnitude difference for the values of 0.43 W/mK and 0.24 W/mK obtained from the solutions of the phonon Boltzmann transport equation and the modified Debye-Callaway model respectively. The latter theoretical result seems to be consistently smaller than the result obtained from the ShengBTE model by around 40%, this could be because only a fraction of the optic modes are included in the calculation for the modified Debye-Callaway model, we can see this trend across the predicted thermal conductivity values as a function of temperature as seen in Figure. 4.12. The lower than experimental predicted value of κ_{lat} may be due to the fact that this calculation was performed for the homogeneous Ni interstitials model, which we have seen to be in disagreement with the experimental result when analysing the neutron weighted phonon DOS. This means that a further calculation for the clustered Ni model could lead to better agreement with experimental results and test the accuracy of the theoretical approach.
The curve in Figure. 4.13 can show the value of the cumulative κ_{lat} up to a maximum allowed phonon mean free path (MFP), here we can see a vast difference between TiNiSn and $TiNi_{1.125}Sn$ where the final converged value of κ_{lat} can be found at 750 nm and 30 nm respectively. This is an order of magnitude in difference and could suggest the possibility of a large variation in grain sizes could dominate over the anharmonic scattering as a possible explanation. However, as the experimentally obtained thermal conductivity values have their own significant variations as observed for TiNiSn and often attributed to the different sample processing techniques [126], it may be worthwhile to investigate the optimal grain size which can be engineered for defective compositions with significant excess Ni content of perhaps 10% as synthesised by my collaborators and modelled in my investigations.

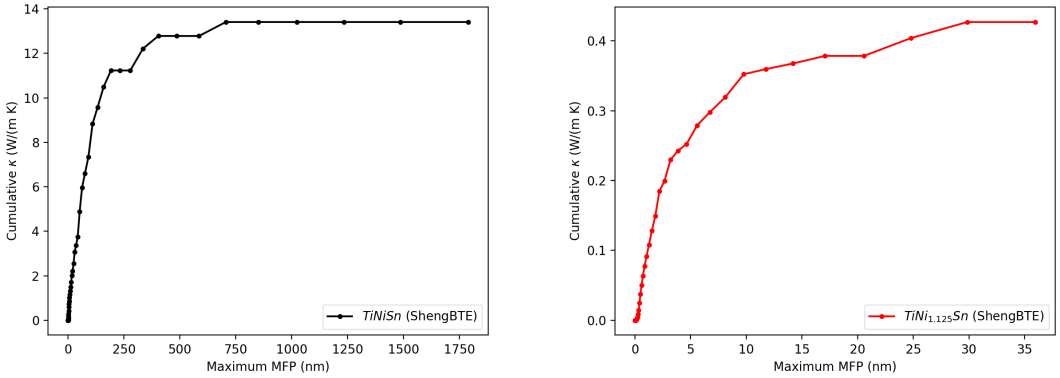

Fig. 4.13 Cumulative lattice thermal conductivity of TiNiSn and $TiNi_{1.125}Sn$ as a function of the maximum mean free path at a temperature of 300K. Both results were computed using ShengBTE.

4.6 Conclusions

This chapter studies the vibrational properties of n-type XNiSn (X = Ti, Zr, Hf) based compositions with a focus on exploring the effects of interstitial defects on the vibrational spectrum and lattice component of the thermal conductivity. The phonon spectra were theoretically modelled using an ab initio approach in conjunction with conducting measurements of phonon DOS from powder inelastic neutron scattering experiments. Calculations of κ_{lat} involved solving the Boltzmann transport equation as well as incorporating the effect of grain boundaries. The use of supercells was required to theoretically model the desired concentration and ordering of interstitial defects. Hence, a scheme for unfolding their phonon dispersion was utilised to enable comparison against stoichiometric parent compounds to unpack the complexity of the folded supercell phonon dispersions.

Calculations of the phonon spectra of the stoichiometric parent materials of TiNiSn, ZrNiSn and HfNiSn were performed to understand the nature of the phonon modes and benchmark against literature and experimental results. Good agreement of structural parameters as well as qualitative features of the phonon dispersion was obtained. Due to the promising experimental measurements of reduced κ_{lat} in the presence of interstitial Ni on the half-Heusler vacancy sites, an in-depth investigation of the role of interstitial defects was undertaken. Analysis of the results has shown that a clustered model for Ni interstitials provides the best agreement with the experimentally measured phonon DOS in contrast to a homogeneous interstitial Ni ordering. In addition, studying the effect on the phonon modes has shown that the presence of Ni interstitials, a significant level of phonon broadening in the low to intermediate phonon frequency range is present that can contribute to a reduction of the mean phonon lifetimes. This effect is less pronounced in the low frequency region for the compositions containing Cu interstitials, however significant phonon broadening is still observed in the intermediate frequency range. Calculations of the κ_{lat}, were performed for TiNiSn as well as the homogeneous defect model containing Ni interstitials, the latter was chosen due to the lower computational cost in comparison to the clustered intestitial

defect model, allowing for the calculation to be computationally feasible. There is a range of values reported for the κ_{lat} for TiNiSn in literature for both theoretical and experimental approaches. This stems from the knowledge that different synthesis and preparation techniques seem to have an impact on the thermoelectric properties in the case of experimental measurements. Moreover, due to difficulty in theoretical predictions of κ_{lat}, the varying levels of theory, assumptions, and parameters used in theoretical calculations that can impact the final result and agreement with experiment. However, we have successfully demonstrated calculations solving the iterative Boltzmann transport equation as implemented in ShengBTE for TiNiSn, resulting in good agreement with the theory. Here it was evident that the inclusion of grain boundaries plays a major role in the reduction of the κ_{lat} and an improvement of the synthesis process to optimise grain size would be of great interest. In addition, demanding supercell defect calculations of $TiNi_{1.125}Sn$ were successfully performed, showing an order of magnitude reduction in the lattice thermal conductivity in predictions stemming from both the Boltzmann transport equation and Debye-Callaway model. Clustering of Ni interstitials was not modelled for the calculations of κ_{lat} due to the computational expense and time constraints of the project but would be a useful future research direction to fully understand the role of interstitials as a mechanism for lowering the κ_{lat} and optimising thermoelectric performance.

Chapter 5

Electronic properties of XNiSn (X = Ti, Zr, Hf) with interstitial defects

5.1 Background

In chapter four we investigated the effects of interstitial defects on the phonon spectrum and lattice component of the thermal conductivity. However, the viability of these half-Heusler materials as good thermoelectrics is largely attributed to their good power factors. A combination of X-site alloying and interstitial Cu defects was deployed and experimentally measured in $Ti_{0.5}Zr_{0.25}Hf_{0.25}NiCu_{0.025}Sn$, achieving a power factor of 3.6 $mWm^{-1}K^{-2}$ [1]. Unlike the good power factors, half-Heusler's have a relatively large thermal conductivity, which impedes performance. It can be seen from the results presented in chapter four that interstitial defects can be a beneficial mechanism for optimising thermoelectric performance, but the Seebeck coefficient, electrical conductivity, and thermal conductivity are often interdependent mechanisms forming the optimisation challenges that we are trying to solve. Attempts to understand and optimise thermal conductivity have been made through different methods. For example, binary and tertiary X-site substitution led to greater phonon scattering, primarily due to mass difference [24] as well as grain size engineering through changing the synthesis method [127]. On the other hand, in this chapter we will focus on the effects of Ni and Cu interstitials on the electronic properties of these materials. We assess the consequences of interstitials as a mechanism for lowering thermal conductivity and test if this route for optimising performance can be achieved without significantly impeding the electrical properties. Previous efforts to compute the band gap in the stoichiometric compositions of TiNiSn, ZrNiSn and HfNiSn resulted in a mismatch with an experiment where the experimental band gap was measured at around 0.12 eV [128] compared to a significantly larger theoretical band gap of around 0.43 eV [129]. These calculations were performed using the PBE (GGA) approximation and a well known artefact of this exchange-correlation potential is that it often underestimates the band gap, but here we see the contrary. Further experimental investigations have demonstrated that TiNiSn has the ability to accommodate as much as around 10% of interstitials [1] and a

smaller amount between 2-3% in ZrNiSn and HfNiSn. One study has modelled a low concentration of 1% Ni interstitials and its effect on the band gap, with the study reporting a band gap of 0.08 eV [129], now in much better agreement with the experimental result. Nevertheless, no study to our knowledge has attempted to replicate interstitial content close to the maximal experimental concentrations, which is what forms the main part of the investigation in this chapter. In addition, the introduction of interstitial Cu doping has been shown to improve the power factor. Electronic structure properties are studied and analysed in this chapter in order to understand the origins of this improvement as well as the effect of interstitial Ni and Cu concentration on the nature of the electronic band structure.

To perform this analysis, I begin by first computing the stoichiometric electronic structure properties of TiNiSn, ZrNiSn and HfNiSn using the CASTEP code [51] to establish baseline results and benchmark against existing literature, presenting the electronic band structures. In order to model the effect of various interstitial concentrations, supercell calculations were required. This introduces band folding due to the reduction of the Brillouin Zone upon increasing supercell size. Therefore, a procedure for obtaining effective band structures was utilised with the help of the *bs_sc2pc.f90* code [103] to enable the comparison against the stoichiometric band structure along the primitive cell BZ. Modelling was performed for 6.25% and 12.5% interstitial content of Ni and Cu. Qualitative and quantitative comparisons against experimental findings are made for compositions with comparable interstitial content. To understand the possible roots of mismatch with predicted metallic behaviour for experimentally semiconducting compositions, calculations were performed for charged systems via the removal of electrons. In addition, calculations applying the Hubbard U correction were undertaken with the aim of understanding possible localisation effects through the application of the Hubbard U parameter to the Ni d states. A further investigation was completed to compare the performance of the RSCAN meta-GGA exchange-correlation functional, to determine whether this introduces any qualitative differences in the result. In addition, a calculation of the effective band structure of $Ti_{0.5}Zr_{0.5}NiSn$ showing the effects of X-site substitution is presented and contrasted against the effect of interstitial defects. Finally, a finite difference method is utilised to compute the effective electron masses for the conduction band minima for relevant compositions, using the formalism implemented in the *emc.py* code [105]. This allows approximating the effective masses within the parabolic band approximation.

5.2 Computational Details

Electronic structure calculations were performed using the CASTEP first principles simulation package [51]. The same choice of pseudopotentials, calculation parameters, and exchange-correlation potential was used as in chapter four, with the addition of the RSCAN (meta-GGA) functional being utilised for a subset of the electronic structure calculations.

A primitive face-centered-cubic cell containing 3 atoms was used for the stoichiometric compositions. On the other hand, the supercell approximation was used in calculations for the defective compositions to incorporate the interstitial defects. This was modelled in supercells containing a 2*x*2*x*2 multiple of the primitive fcc cell, containing 25 atoms. Structural relaxation was also performed using the same convergence criteria as in chapter four. The electronic band structures of supercell calculations were unfolded to obtain a primitive cell representation of the supercell band structure using the *bs_sc2pc* code [103] which implements the scheme described by Popescu and Zunger [90], modified for use with ultrasoft pseudo-potentials. The effective band structure (EBS) for the relaxed structure was calculated along the G–X–G–L–W–X path in the primitive Brillouin zone using the same convergence parameters as for the structural relaxation. Altering the number of electrons in the system was specified using the CHARGE parameter as required. The Hubbard U was specified within the <seedname>.cell file for the chosen species and orbitals. The electronic DOS was calculated on a fine 30*x*30*x*30 Monkhorst-Pack grid. The graphical representation of the electronic DOS was plotted using the *dispersion.pl* [51] script and matplotlib [115] was used for plotting the primitive cell band structures and well as the supercell effective band structures. For the effective mass calculations the step size controlling the grid for evaluating the energy derivatives with respect to **k** was set at 0.05 1/Bohr.

5.3 Stoichiometric electronic structure properties

TiNiSn, ZrNiSn and HfNiSn are half-Heusler alloys are a unique composition as even though there are metallic constituents, the resulting structure forms an 18 electron closed-shell system. In this chapter, the same simulation cell as for the calculations of vibrational properties of the stoichiometric half-Heuslers was used to compute the electronic properties. Similarly, the defective structure calculations containing 12.5% of interstitials were performed in a 2*x*2*x*2 multiple of the primitive fcc cell, where the homogeneous defect placement was chosen to keep the computational expense relatively low, placed at the 4d (0.75, 0.75, 0.75) Wyckoff position. To model the lower 6.25% concentrations of Ni in a larger 2*x*2*x*4 supercell containing 49 atoms was required. Lastly, a 2*x*2*x*5 supercell containing 61 atoms was used to incorporate 5% of Cu interstitials.

The band structure plots of TiNiSn, ZrNiSn and HfNiSn can be seen in Figure. 5.1 with all three stoichiometric compositions being predicted as semiconducting with the Fermi level placed within the band gap. The valence band maximum (VBM) is triply degenerate, positioned at the Γ, and the conduction band minimum (CBM) can be found at X. There is a small indirect band gap for each of the three systems at a size of 0.46 eV for TiNiSn, 0.5 eV for ZrNiSn, and 0.42 eV for HfNiSn. These values are in good agreement with literature [130, 129]. However, the band gap in TiNiSn is bigger than the experimentally reported gap of 0.12eV and as the PBE exchange-correlation functional

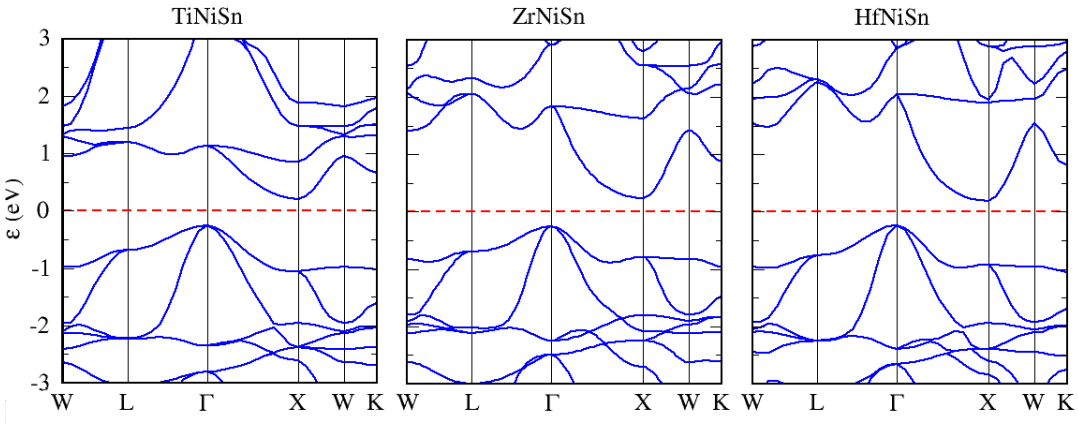

Fig. 5.1 Electronic band structures of TiNiSn, ZrNiSn and HfNiSn. Plotted along the $W-L-\Gamma-X-W-K$ path through the Brillouin zone. The dashed red line represents the Fermi energy.

is well known for underestimating the band gap, the significantly smaller experimental band gap cannot be attributed to this discrepancy but would suggest the difference is even larger. Consequent attempts to investigate this have found that measured samples contained Ni interstitials, generally, when attempting to synthesise the stoichiometric half-Heusler compound between 1-3% of Ni interstitials were present [1, 131]. In addition, TiNiSn was shown to be unique, in that it is able to accommodate even larger concentrations of Ni interstitials of up to 10%. This turns out to be significant as measurements of κ_{lat} have shown a significant effect of lowering the κ_{lat} when increasing interstitial content, which is crucial to optimising the thermoelectric performance in half-Heuslers. Investigations of a small concentration with 1% of Ni interstitials have been computed within the GGA treatment of the exchange and correlation and a band gap of 0.08 eV was stated. This would suggest agreement with experimental data. Moreover, the study noted the presence of in-gap Ni defect states, which would explain the closing of the gap in the presence of interstitials. However, no further investigation was made to determine the optimal content of Ni interstitials and their effect on the electronic properties.

Structure	Direction	Effective mass
TiNiSn	$\Gamma-X$	2.92, 2.89[130]
TiNiSn	$X-W$	0.59, 0.56[130]
ZrNiSn	$\Gamma-X$	3.13, 3.23[130]
ZrNiSn	$X-W$	0.41, 0.38 [130]
HfNiSn	$\Gamma-X$	3.13 , 3.14[130]
HfNiSn	$X-W$	0.39, 0.36 [130]

Table 5.1 Effective Masses of the conduction band minima represented in units of free electron mass for TiNiSn, ZrNiSn, HfNiSn obtained from ab-intio calculations, computed along high symmetry directions though the BZ.

Tests were performed to compute the effective masses of the CBM for the stroichiometric compositions of TiNiSn, ZrNiSn and HfNiSn along a chosen set of high-symmetry

directions through the Brillouin zone. In Table. 5.1 we can see that calculated effective masses are in close agreement with the values found in the literature [130]. This agreement provides additional confidence to apply the methodology for calculating effective masses of the more complex defective structures of these parent materials. The results of which will be presented in Section. 5.4 where they will be analysed further.

5.4 Interstitial Ni and Cu defects in $XNi_{1+x}Cu_ySn$ (X = Ti, Zr, Hf)

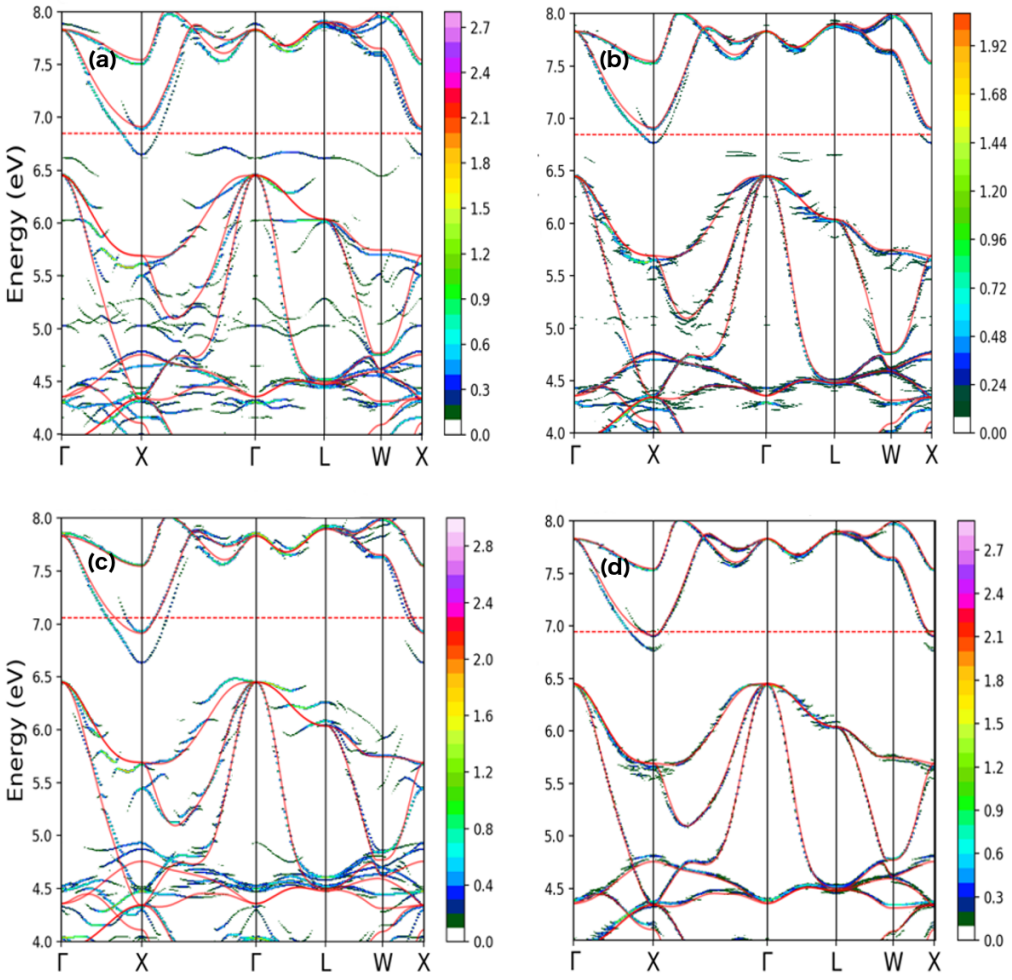

Fig. 5.2 Unfolded bandstructures of 2 x 2 x 2 supercells for (a) $TiNi_{1.125}Sn$, (b) $TiNi_{1.0625}Sn$, (c) $TiNiCu_{0.125}Sn$ and (d) $TiNiCu_{0.05}Sn$ showing the effect of varying interstitial concentrations. The value of 1 on the colour bar corresponds to a single non-degenerate band per energy interval. The continuous red line is the band structure for TiNiSn, calculated using a primitive fcc unit cell. The dotted red line indicates the Fermi energy.

This section of the chapter explores the unique ability of TiNiSn to accommodate larger interstitial content. In addition to investigating the effect of Ni interstitials, we will also explore the choice of Cu interstitials to act not only as a potential enhancement to phonon

scattering but as a simultaneous n-type dopant. Results of the computed effective band structures of these systems are presented in Figure. 5.2 with the PBE exchange-correlation functional being used in this set of calculations. We can see in Figure.5.2 (a) and (b), the appearance of in-gap Ni states, these have a rather flat curvature, suggesting localised defect states. This is not seen with the addition of Cu interstitials that is in agreement with experimental data showing no change to the electron mobility, which could've been otherwise decreased due to carrier scattering [1]. Both the Ni and Cu interstitials show the development of a new partially filled band at the CBM. Band fitting using a finite differences approach and a valley degeneracy, $N_v = 3$ was used to compute the effective masses for the band at the CBM that can be found at the X-point. This resulted in an $m^*_{dos} = 2.5$ for $TiNiCu_{0.125}Sn$, this higher value is due to an overall decrease in band anisotropy even though the gradient of the band is steeper for the $\Gamma - X$ direction and is in line with the experimental result of $m^*_{dos} = 4.1$ [1], suggesting that addition of Cu increases the effective mass. The computed m^*_{dos} of TiNiSn was found as $m^*_{dos} = 2.1$, compared to the experimental $m^*_{dos} = 2.8$ for TiNiSn. The absolute values of the effective masses are not in exact agreement with experimental values, but this can be attributed to the fact that the method of fitting the effective mass is approximate, where the choice of step size and degree of anisotropy will skew the result. In addition, the choice of GGA exchange-correlation functional leads to approximations of the exchange energy, which can lead to differences between the computed and experimentally found effective masses [132].

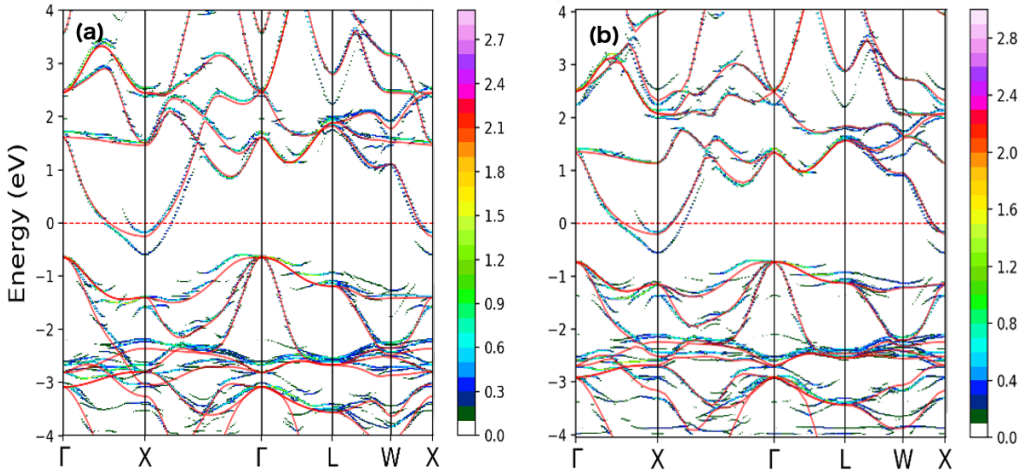

Fig. 5.3 Unfolded bandstructures of 2 x 2 x 2 supercells for (a) $HfNiCu_{0.125}Sn$, (b) $ZrNiCu_{0.125}Sn$ showing the effect of varying interstitial Cu concentrations. The value of 1 on the colour bar corresponds to a single non-degenerate band per energy interval. The continuous red line is the band structure for TiNiSn, calculated using a primitive fcc unit cell. The dotted red line indicates the Fermi energy.

In addition, experimental samples contain defects and additional phases, which have an impact on the electrical properties. For comparison calculations including Cu interstitials were also performed for $ZrNiCu_{0.125}Sn$ and $HfNiCu_{0.125}Sn$, the unfolded band structures

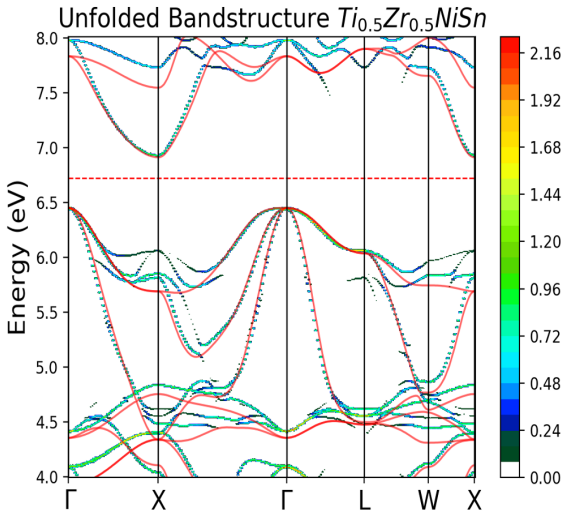

Fig. 5.4 Unfolded bandstructure for the binary X-site substitution in $Ti_{0.5}Zr_{0.5}NiSn$ showing the effect of varying interstitial Cu concentrations. The value of 1 on the colour bar corresponds to a single non-degenerate band per energy interval. The continuous red line is the band structure for TiNiSn, calculated using a primitive fcc unit cell. The dotted red line indicates the Fermi energy.

can be seen in Figure. 5.3. As it was demonstrated experimentally that these compositions can only accommodate up to around 2-3% of interstitials, but 12.5% of interstitials was modelled for consistency. This allows us to reinforce the presence of a new partially filled band at the CBM as well as the lack of in-gap states for both $ZrNiCu_{0.125}Sn$ and $HfNiCu_{0.125}Sn$. In contrast, the EBS of $Ti_{0.5}Zr_{0.5}NiSn$ modelling the effect of binary X-site substitution is also computed and presented in Figure. 5.4, here the band structure resembles that of the stoichiometric TiNiSn, with the presence of additional spectral weight only near the X and W-points, but at energies distant from the Fermi level, so they are not expected to play a role in conduction. Moreover, we do not see the development of a new partially filled band at the CBM and no in-gap defect states can be seen. This behaviour is to be expected as the band structures of the stoichiometric compounds show the same qualitative features as it was seen in Figure. 5.1.

Structure	Theoretical m^*_{dos}	Exp. m^*_{dos}
TiNiSn	2.1	2.8
ZrNiSn	1.7	2.7
HfNiSn	1.6	2.7
$TiNi_{1.25}Sn$	2.3	3.1
$TiNiCu_{0.125}Sn$	2.5	4.1

Table 5.2 Effective masses for the conduction band minima of TiNiSn, ZrNiSn, HfNiSn, $TiNi_{1.25}Sn$ and $TiNiCu_{0.125}Sn$ obtained from ab-intio calculations compared against experimental data collected by my collaborators [9] for comparable compositions.

5.4.1 Localised effects using Hubbard model

To try and understand the cause for the prediction of a metallic state in the case of the calculations with Ni interstitials, one approach is to investigate localisation effects. Use of the GGA exchange and correlation functional often suffers from an excessive delocalisation error, which neglects correlation effects. Resulting in the localised states being placed too close to the Fermi energy. This can be addressed using the DFT+U approach to apply a Hubbard U model [71], which has been performed on the $TiNi_{1.125}Sn$ system. Applying the Hubbard U is appropriate particularly for open shell d and f shell systems. When looking at the nature of the DOS decomposed onto the angular momentum channels as shown in Figure. 5.5, we can see that the open shell Ni d states have a significant DOS near the Fermi level, providing for motivation in testing the ability of PBE in capturing their correct band structure. The choice of the U parameter is semi-empirical and tests for a range of U values (1-5 eV) have been undertaken as the U value is not known unless tuned against known experimental results or computed using higher level calculations, such as a DFT+DMFT approach [133]. The results of an unfolded electronic band structure of $TiNi_{1.125}Sn$ with a U = 3 applied are presented in Figure. 5.6. We can see that the is still partial filling of the conduction band at the X-point, with only a slight up-shift of the bands in comparison to the calculation without the Hubbard U. This was consistent for all tested U values and suggests that correlated Mott insulator type behaviour [71] is not evident from the results and another mechanism for charge compensation may be involved.

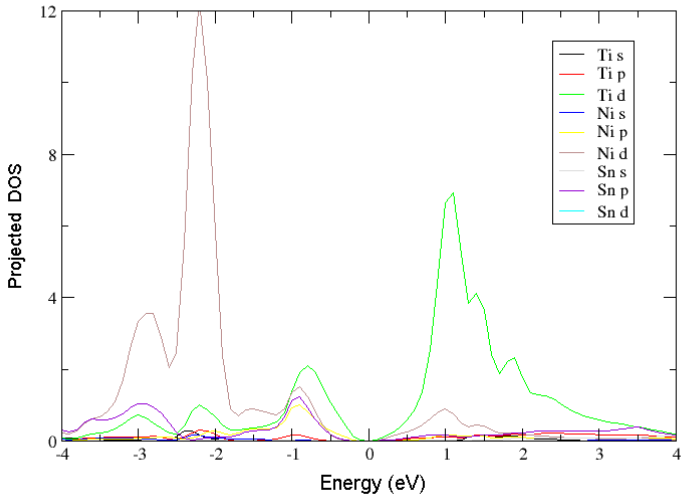

Fig. 5.5 Partial DOS decomposed onto species and angular momentum channels for TiNiSn.

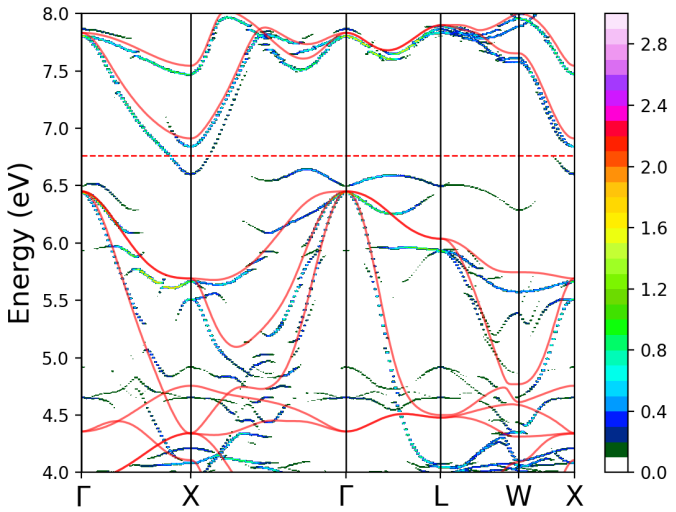

Fig. 5.6 Unfolded bandstructure for $TiNi_{1.125}Sn$ with a Hubbard U parameter of 3 applied. The value of 1 on the colour bar corresponds to a single non-degenerate band per energy interval. The continuous red line is the band structure for TiNiSn, calculated using a primitive fcc unit cell. The dotted red line indicates the Fermi energy.

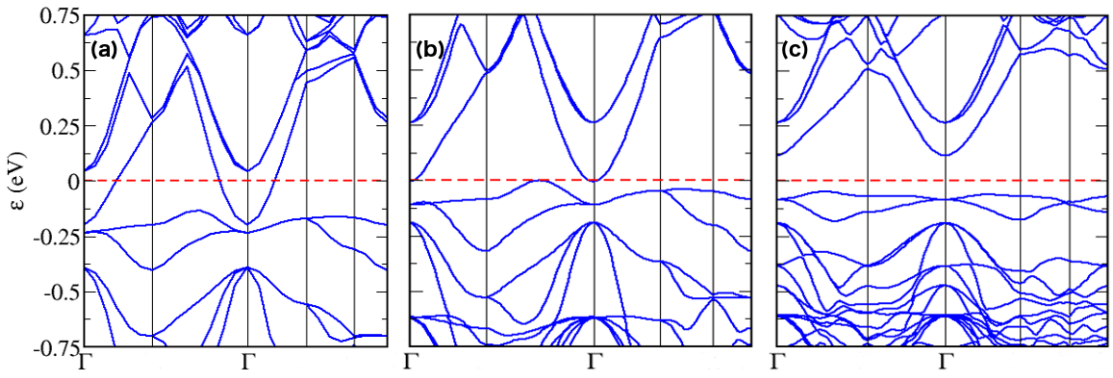

Fig. 5.7 Folded supercell bandstructure of (a) $TiNi_{1.125}Sn$ with no charge removed, (b) $TiNi_{1.125}Sn$ with a +1 charge and (c) $TiNi_{0.0625}Sn$ with a +1 charge. The supercell BZ path is shorter than that of the primitive cell BZ. The red dashed line represents the Fermi energy.

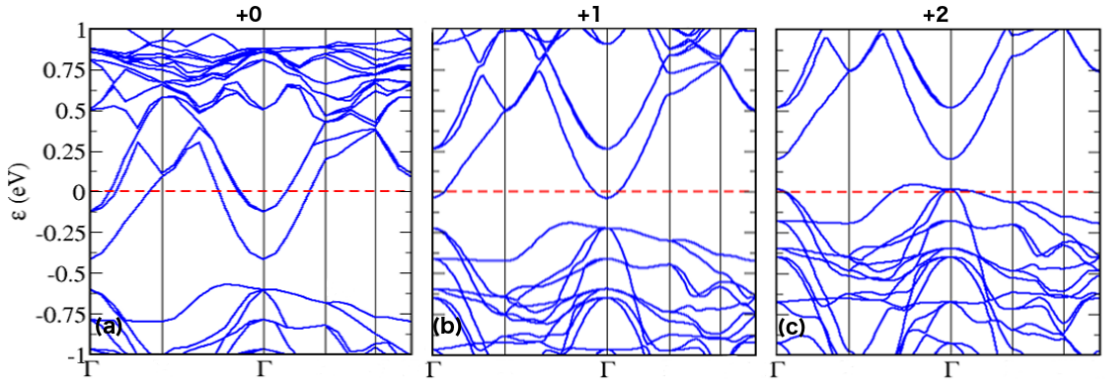

Fig. 5.8 Folded supercell bandstructure of $TiNiCu_{0.125}Sn$ computed with 0, 1 and 2 electrons removed. The supercell BZ path is shorter than that of the primitive cell BZ. The red dashed line represents the Fermi energy.

5.4.2 Charged calculations

Due to the additional electron from Cu, the Fermi energy has shifted upwards more significantly than in the case of Ni, resulting in a larger volume of the conduction band being partially filled around the CBM. The compositions with Ni and Cu both indicate metallic behaviour in disagreement with the experiment. To understand the possible roots of this mismatch and gain an estimate of the extent of charge compensation mechanisms that may be present, calculations were performed for charged systems with the removal of electrons. This was done by modifying the total number of electrons for the total energy calculation in CASTEP. The results for the effect of a +1 charge on the $TiNi_{1+x}Sn$ composition at varying Ni concentration can be seen in Figure. 5.7. This figure shows the folded supercell BS, which is not representative of the primitive cell E(**k**) relationship apart from Γ and the position of the Fermi energy. We can see that the removal of charge does in fact allow for the band gap to form, with the lower excess Ni concentration at 6.25% forming a gap of around 0.2 eV. In the case of adding Cu interstitials, the overall net system charge was set and the band structure was re-calculated calculated for charge values ranging from +1 to +2 charge in the case of Cu. The results are presented in Figure. 5.8. Here unlike in the case of interstitial Ni, removing electrons to achieve a +1 net charge still results in metallic behaviour, with partial filling of the conduction band. In Figure. 5.8 (c) for the Cu +2 system, the Fermi level now placed in the valence band. Hence, an intermediate level of charge compensation is expected. However, the numerical convergence of the Brillouin Zone integral in the calculation of the Fermi level is difficult to accomplish. Therefore, taking into account a margin of error and the fact that a discrete number of electronic states is expected, it's likely that the Cu +1 system would result in the Fermi level within the band gap. From the computed results with the present level of convergence, n-type semiconducting behaviour might be expected with a net charge between +1 and +2 electrons. This could arise from grain boundaries, point defects, and other mechanisms that could explain the experimentally observed behaviour if additional charge compensation is a real effect. Experimental Hall data [9] for the $TiNiCu_{1+x}Sn$ composition shows carrier concentrations greater than 1 e^-/Cu. This coincides with the obtained theoretical results. However, it was not possible to establish the specific macroscopic mechanism responsible for this effect from the current results. The charge compensation for the Ni interstitials in the experimental samples can occur due to other negative species in the sample, possibly in the form of metal vacancies or the presence of oxygen. This would allow the composition containing interstitials to retain semiconducting behaviour and allow the Fermi energy to be found in the band gap.

5.4.3 GGA vs meta-GGA

Another approach to tackle potential sources of inaccuracy through the use of semi-local GGA functionals is to go a step further and use newer formulations for exchange

functionals, which aim to provide greater accuracy through the addition of the orbital kinetic energy density, namely meta-GGA's. This is precisely the approach deployed in this section using the rSCAN functional [100]. Structural relaxation of the atomic positions was performed. This was followed by a calculation of the electronic DOS for $TiNi_{1.125}Sn$, the results are shown in Figure. 5.9. Here we can see that there is still non-zero density present around the Fermi energy, meaning that the prediction of a metallic state still persists. There is a small change to the DOS around the Fermi energy with additional DOS near the conduction band minimum. This suggests further evidence of the need to investigate additional charge compensation effects apart from only considering the localisation of Ni d states.

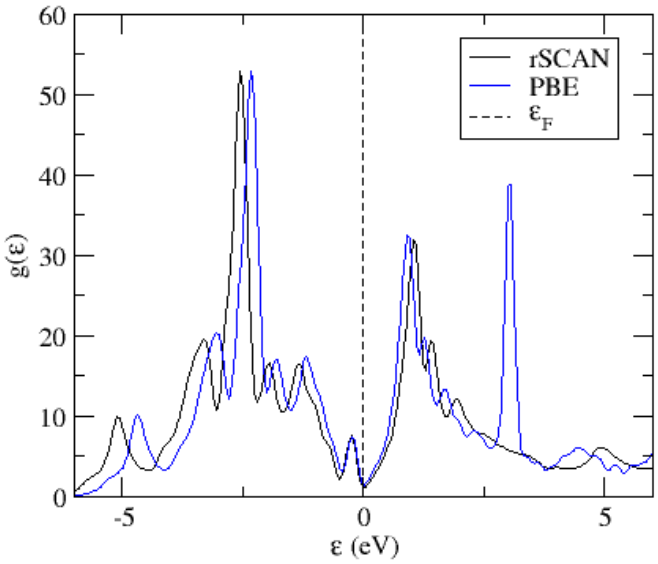

Fig. 5.9 Electronic DOS computed for $TiNi_{1.125}Sn$ with PBE (blue) and rSCAN (black) exchange-correlation functionals.

5.5 Conclusion

In summary, the baseline results for structural parameters and electronic structure properties of stoichiometric compositions are in good agreement with benchmark literature results. This chapter establishes the impact of large Ni and Cu interstitial content on the electronic structure properties. The results of the calculations considering the addition of interstitial Cu have shown to provide the most promising effect in enhancing thermoelectric properties compared to Ni interstitials. This is due to the lack of in-gap states being present that could otherwise lead to carrier scattering and impede carrier mobility. The experimental semi-conducting behaviour and band gap require further investigation as applying the Hubbard U correction on the Ni d states does not provide a conclusive result with metallic behaviour still being predicted in disagreement with experimental findings. Moreover, using the rSCAN meta-GGA functional for the treatment of the exchange and correlation, did not change to prediction of a metallic state from calculation. Performing charged

calculations revealed that the compensation of 1 e^- charge for systems with interstitial Ni reproduces the semi-conducting behaviour and presence of a band gap, consistent with experiment and literature [134, 129], even at an interstitial content of 12.5%. Whereas in the case of Cu interstitial, where the additional electron in Cu leads to an intermediate level of charge compensation between 1-2 electrons. However, a discrete number of electronic states is expected and there is a likely hood that the Cu +1 system would result in the Fermi level within the band gap as some uncertainty can arise due to numerical convergence errors when computing the exact position of the Fermi level. Further studies could consider investigating applying the Hubbard U parameter to additional states or alternative treatments of correlated systems using approaches such as DFT + DMFT [135] as well as modelling the effects of other charge compensation mechanisms due to the presence grain boundaries or other defects. Moreover, it would be of interest to compute charged calculations for the Zr and Hf based half-Heuslers containing interstitial Ni and Cu to compare and contrast against the TiNiSn based compositions.

Chapter 6

Electronic structure properties of $Nb_{1-x}CoSb_ySn_{1-y}$

6.1 Background

Generally, when considering half-Heuslers as potential thermoelectrics, we search compositions that satisfy the 18 electron rule for the valence electrons. This often ensures semiconducting behaviour, allowing for further attempts in optimising the electronic properties to enhance performance, commonly achieved through doping. However, it has been found that only searching for compositions that satisfy the 18 electron rule, may omit potential candidates for good thermoelectric materials. We will begin this chapter by computing the stoichiometric electronic structure properties of NbCoSn and NbCoSb, which are 18 and 19 electron compositions respectively. Interestingly, the 19 electron NbCoSb system is found to be one such potential composition and behaves as an n-type material showing good thermoelectric performance, with a measured ZT value of 0.4 at 973K [25]. Similar to the XNiSn (X = Ti, Zr, Hf) compositions, the series of compositions in this chapter benefits from the desirable low cost, non-toxic, and relatively abundant materials [136]. This prompted investigations to optimise thermoelectric performance in these materials. One of the initial endeavours involved Sn doping in $NbCoSb_xSn_{1-x}$, where an improved ZT of 0.56 was achieved at 20% (x = 0.2) Sn doping [25]. Further experimental efforts analysing synchrotron data had revealed significant numbers of stable Nb site vacancies, tending towards a composition of $Nb_{0.8}CoSb$, which leads the system back to an average count of 18 valence electrons. It was subsequently theoretically predicted that the NbCoSb structure is unstable [137]. My investigations model this system through DFT calculations, in order to benchmark and perform analysis of the electronic structure of these compositions through analysis the band structures, electronic DOS, and computing the effective electronic masses, $m*_{dos}$. In addition, my collaborators have measured the thermoelectric properties of the defective $Nb_{0.85}CoSb$ composition, which resulted in a ZT of 0.5 at 950K. Even though this experimentally measured composition contains 18.25 valence electrons, the material displays semiconducting behaviour and can be treated as

a heavily doped semiconductor. I then investigate the composition of $Nb_{0.9}CoSb_{0.5}Sn_{0.5}$, which allows the composition to maintain an average 18 electron count at a smaller number of Nb vacancies, but reducing the average number of electrons through replacing 50% of the Sb atoms with Sn. The behaviour of this system is found to be semiconducting, with an effective mass, $m*_{dos}$ of 1.0 m_e for $Nb_{0.8}CoSb$ and 9.5 m_e in $Nb_{0.9}CoSb_{0.5}Sn_{0.5}$ at the CBM. It is shown that the position and ordering of the CBM minimum are sensitive to Sn concentration enabling band convergence to increase the valley degeneracy and therefore increasing the $m*_{dos}$. This provides additional insight in understanding the effects on the electronic band structure in a composition with a complex defect structure. However, the nature of thermal transport has not yet been fully investigated.

6.2 Computational Details

Electronic structure calculations were performed using the CASTEP first-principles simulation package [51]. The same choice of pseudopotentials, calculation parameters, and exchange-correlation potential was used as in chapter four. A primitive face-centered-cubic cell containing 3 atoms was used for the stoichiometric compositions. On the other hand, the supercell approximation was used in calculations for the defective compositions with interstitials. The supercell was a $2x2x5$ multiple of the primitive fcc cell, containing between 56 atoms for the case of $Nb_{0.8}CoSb$ and 58 atoms for $Nb_{0.9}CoSb_{0.5}Sn_{0.5}$. Structural relaxation, supercell band structure unfolding and plotting of the effective band structure and electronic DOS were performed using the same methods and parameters as in chapter five. The effective band structure for the relaxed structure was calculated along the Γ–X–Γ–L–W–X path in the primitive Brillouin zone.

6.3 18 vs 19 electron properties, NbCoSb vs NbCoSn

As NbCoSb and NbCoSn are half-Heusler alloys, they share the same structure with XYZ (X = Ti, Zr, Hf) type compositions described in chapters four and five. The key difference of this chapter is the modelling of defects due to deficiency of the X-site Nb atoms, without modelling any potential interstitial content in the half-Heusler vacancy sites. In the case of the effect of heavy Sn doping, the Z-site atoms of Sb are substituted to achieve the desired concentration. The relaxed lattice parameter for NbCoSb is in good agreement with theoretical literature results [138]. There is more than a 1% mismatch between the experimental lattice parameter for NbCoSb. However, this result did not take into account the possibility of Nb defects, we can see in Table. 6.1 that the lattice parameter of $Nb_{0.8}CoSb$ is in better agreement with the experimental result, differing by 0.04 Å, the slight overestimation is within the expected error of the GGA approximation [139].
We begin the journey to understanding more about the electronic properties in these materials by plotting the electronic band structures of NbCoSb and NbCoSn as seen in

Structure	Lattice Param. (Å)	Exp. Lattice Param (Å)
NbCoSb	5.978, 5.975 [138]	5.897[25]
NbCoSn	5.968	5.954 [140]
$Nb_{0.8}CoSb$	5.938	5.899 [137]
$Nb_{0.9}CoSb_{0.5}Sn_{0.5}$	5.952	n/a

Table 6.1 Equilibrium Lattice Parameters of NbCoSb and NbCoSn

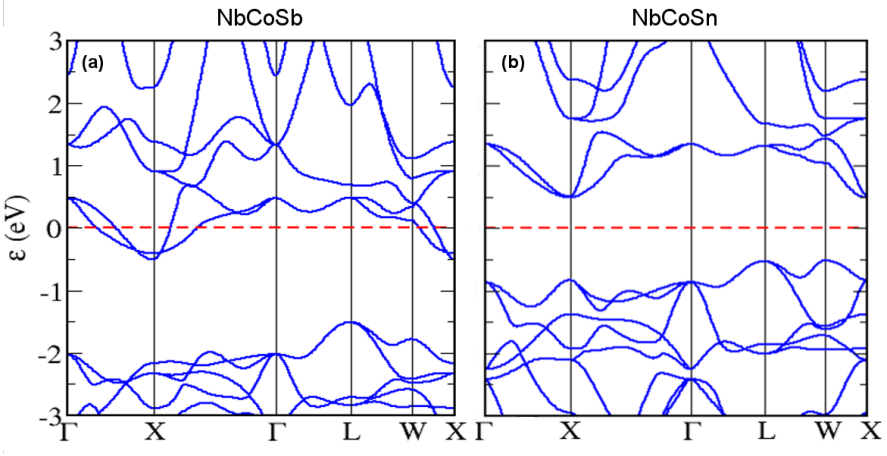

Fig. 6.1 Electronic bandstructures of a) 19 valence electron NbCoSb and b) 18 valence electron NbCoSn half-Heuslers. The dashed red line represents the Fermi energy.

Figure. 6.1. The latter predicts semi-conducting behaviour with a clear band-gap of around 1 eV. The CBM can be located at the X-Point in the primitive cell BZ and band convergence can be observed. Where as the 19 valence electron NbCoSb system is predicted to have the Fermi level situated well into the conduction band, predicting metallic behaviour with the position of the Fermi level relative to the valence and conduction bands can be clearly seen in Figure. 6.2, which displays the electronic DOS. This is an expected finding as the usual 18-electron rule is not satisfied, but one that was puzzling at first as in an initial study, semi-conducting behaviour was experimentally observed [25]. However, further studies have shown that this composition is unstable [137] and in fact diffraction data has shown a formation of between 15-17% of Nb vacancies on the X-site [141]. This provides a mechanism that reduces the electron count down in the range of 18.15-18.25 electrons, with the additional electrons above 18 acting as a dopant.

6.4 Maintaining 18 electron count through X-site vacancy and doping

To gain further insight into the behaviour of the Nb vacancies. I have computed the unfolded band structure of $Nb_{0.8}CoSb$ along the Γ-X-Γ-L-W-X high symmetry path of the fcc primitive cell of NbCoSb. This supercell is a 2x2x5 multiple of the primitive cell and due to the Nb vacancies, the symmetry has been reduced, leading to a change from the space group of $F\bar{4}3m$ (216) to a space group of Cm (8). Because this is an attempt to

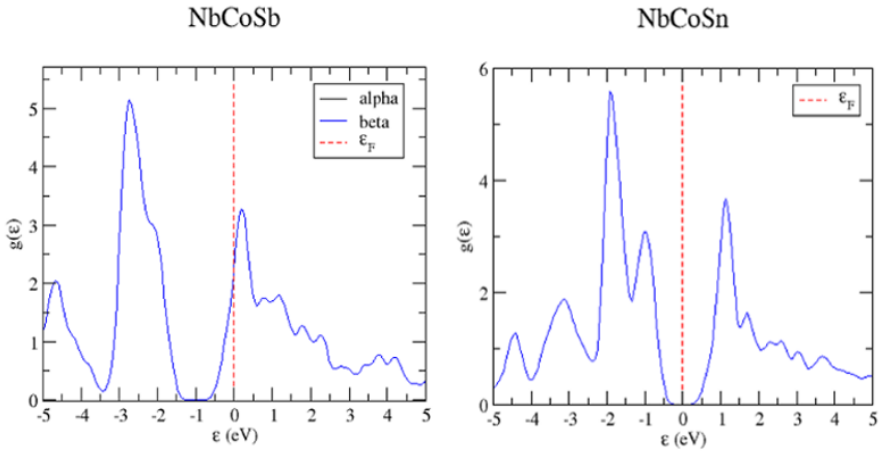

Fig. 6.2 Density of states of a) 19 valence electron NbCoSb and b) 18 valence electron NbCoSn half-Heuslers. The dashed red line represents the Fermi energy.

model one configuration from a cubic ensemble, only internal coordinates were structurally optimised and not the cell parameters. This result is presented in Figure. 6.3. We can see the Fermi energy is in the band gap, predicting semiconducting behaviour in agreement with experimental findings. The position of the VBM and CBM at the L-Point and X-Point remains unchanged. The presence of a significant level of defects due to the presence of 20% Nb vacancies and symmetry breaking leads to broadening of the bands, with some additional spectral weight present in the band gap. The CBM at the X-point appears to have a single minimum, with the closest higher energy band at a separation of around 0.1 eV, corresponding to a temperature greater than 1000 K. This suggests no increase to the valley degeneracy as the states in the flatter band would not be thermally available, which does not suggest an increase of the $m*_{dos}$. However, the literature mentions the development of a new minimum forming at the high-symmetry point U [137] with a different space group symmetry of $I4\bar{(}82)$ that could result in a higher valley degeneracy. This high-symmetry point was not sampled in the chosen BZ high-symmetry path for the result in Figure. 6.3. The experimental samples show a global cubic symmetry with the $F\bar{4}3m$ (216) space group. Meaning that the choice of the ordering of the Nb vacancies may not exactly represent the experimental electronic structure properties.

The next set of results presents an investigation into a complex defective structure model of $Nb_{0.9}CoSb_{0.5}Sn_{0.5}$, which contains both Nb vacancies as well as Sn substitution on the Z-site. As Sn has one less valence electron per atom, this composition allows to satisfy the 18-electron rule exactly. The unfolded band structure for this composition can be seen in Figure. 6.4. We can see that the calculation predicts semiconducting behaviour and exhibits band convergence at the X-point, with a flattening of the heavier band, particularly in the X - Γ direction. The effects of this can be quantified by looking at the results for the effective masses, which were obtained according to the effective mass density of states formula $m*_{dos} = (N_v^2 * m_l * m_t * m_t)^{\frac{1}{3}}$, where $m*_{dos}$ is the effective electron mass, N_v is the valley degeneracy, m_l and m_t are the longitudinal and transverse masses. The results

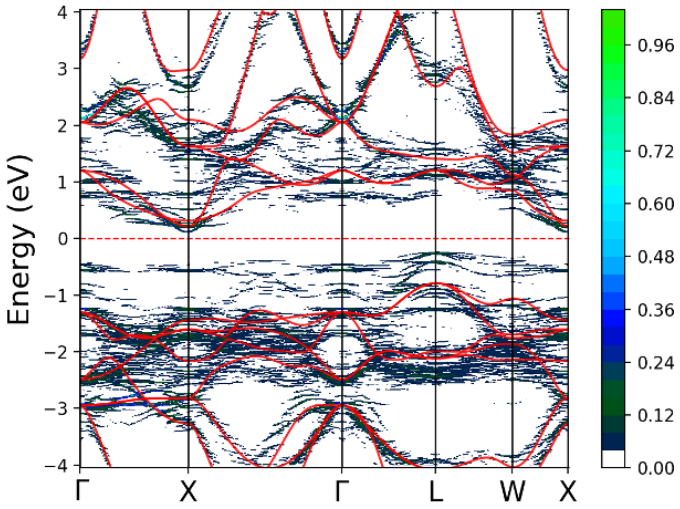

Fig. 6.3 Unfolded band structure of a 2 x 2 x 5 supercell of $Nb_{0.8}CoSb$. The value of 1 on the colour bar corresponds to a single non-degenerate band per energy interval. The continuous red line is the band structure for NbCoSb, calculated using a primitive fcc unit cell. The dotted red line indicates the Fermi energy.

are presented in Table 6.2. The effective masses are computed using a finite difference method at the band extrema. An effective mass of $m*_{dos} = 5.1$ is found for NbCoSn, in reasonable agreement with the experimental result of $m*_{dos} = 6$ [9]. The literature investigating Sn doping, reports an increase in the effective mass to about $m*_{dos} = 10$, this trend is in agreement with the increase for $Nb_{0.9}CoSb_{0.5}Sn_{0.5}$, which was computed to have an $m*_{dos} = 9.5$. As the two bands at the CBM are converged to around 0.01eV, both are expected to contribute to the effective mass. However, the band fitting can only approximate the $m*_{dos}$ of a single band, upon looking at Figure. 6.4 we can see that the two band curvatures are different and anisotropic along the plotted Γ - X and X - Γ directions with additional anisotropy possible along directions that can not be seen from the plot. Normally the valley degeneracy of the half-Heusler X-point is $N_v = 3$, but to account for the two bands converging this is increased to $N_v = 6$. Therefore, only the flatter band has been considered and no further theoretical model was deployed to consider the curvatures of both bands simultaneously. This will contribute to discrepancies in the computed and experimental values of $m*_{dos}$. Comparing with the result when modelling only the Nb vacancies, there appears to be sensitivity to Sn doping on band convergence, but not in the case of X-site Nb content. This is beneficial as the level of Sn can be tuned in order to optimise the power factor, with a trade-off between maximising the Seebeck co-efficient and not impeding the carrier mobility. When considering the effective mass of $Nb_{0.8}CoSb$ as a single contributing band at the CBM, the band shows a steep curvature and has a valley degeneracy of $N_v = 3$. This results in a low $m*_{dos} = 1$ that is almost an order of magnitude smaller from the result of $m*_{dos} = 9.6$ obtained experimentally [141]. The current computational result cannot completely disregard the current ordering of the light and heavy band in this system, but it is possible that the heavy band is in fact the one

contributing at the CBM. This stems from the fact that the computational model does not always fully reflect the real system. This may suggest that there is another mechanism that impacts the band structure, band ordering, or valley degeneracy. This could include the dependence of Nb vacancy ordering [142] or Co interstitials.

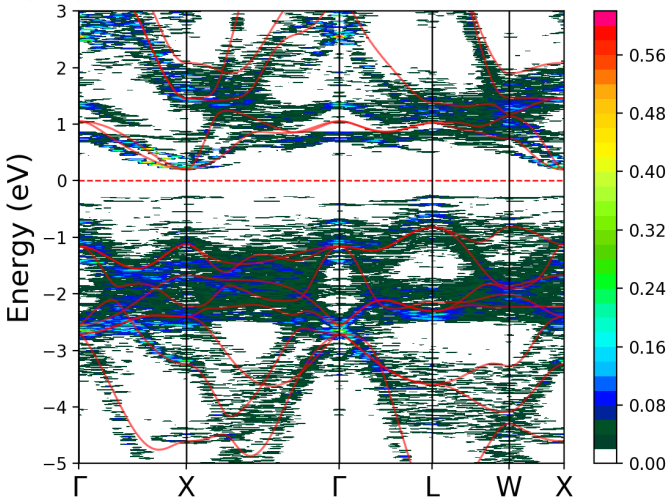

Fig. 6.4 Unfolded band structures of a 2 x 2 x 5 supercell of $Nb_{0.9}CoSb_{0.5}Sn_{0.5}$. The value of 1 on the colour bar corresponds to a single non-degenerate band per energy interval. The continuous red line is the band structure for NbCoSn, calculated using a primitive fcc unit cell. The dotted red line indicates the Fermi energy.

Structure	Theoretical m^*_{dos}	Lit. m^*_{dos}
NbCoSn	5.1	6.0[9],
NbCoSb	5.2 (heavy band), 0.0 (light band)	7.7[9], 7.6 [25]
$Nb_{0.9}CoSb_{0.5}Sn_{0.5}$	9.5	n/a
$Nb_{0.8}CoSb$	5.6 (heavy band), 1.0 (light band)	7.7[9]

Table 6.2 Effective Masses of NbCoSn, NbCoSb, $Nb_{0.9}CoSb_{0.5}Sn_{0.5}$ and $Nb_{0.8}CoSb$ obtained from ab-intio calculations compared against literature data of approximate compositions.

6.5 Conclusions

We have investigated the electronic band structure properties for $Nb_{1-x}CoSb_ySn_{1-y}$ type compositions. The presence of X-site Nb vacancies and their effect of the band structure was investigated due to an initial mismatch between computational efforts to model the stoichiometric NbCoSb composition and experimental structural measurements which later revealed the presence of X-site vacancies. To model this effect, a simulation cell of $Nb_{0.8}CoSb$ was prepared to contain 20% of Nb-site vacancies, providing good agreement with experimental structural parameters. A method for unfolding for computing the effective band structure for the defective supercell calculations was used, to capture the effect of the Nb defects in comparison to the stoichiometric parent materials. The

presence of a band gap is shown in agreement with the experiment, with a single band expected to contribute to conduction, leading to an $m*_{dos}$ significantly smaller than for experimental measurements, due to the computed ordering of the bands in the chosen defect model. Different orderings of the Nb vacancies should be considered to determine the consequences on the electronic properties to investigate if behaviour of the really system can be theoretically found. Additional mechanisms for optimisation of thermoelectric properties and achieving band convergence to increase valley degeneracy, such as the role of interstitial defects may be of interest in future calculations. An effort was made to understand the effect of heavy Sn doping in the $Nb_{0.9}CoSb_{0.5}Sn_{0.5}$ composition, designed to satisfy the 18-electron rule through both Nb-site vacancy and substitution of 50% Sb with Sn. The outcome of computing the effective band structure also predicts a band gap as well as band convergence at the CBM. Consequently, leading to a higher valley degeneracy and a m^*_{dos} that is good agreement with the experiment. This revealed the sensitivity of conduction bands to Sn concentration. These findings suggest that tuning the Nb vacancy content and level of Sn doping can be used as a mechanism for optimising the carrier concentration and increasing the Seebeck coefficient. Furthermore, studies of thermal transport properties would be of considerable interest, to understand the effect of Nb vacancies on the thermal conductivity and to gain predictive power in further optimisation of the thermoelectric properties of these materials.

Chapter 7

Conclusions

This thesis has focused on investigating the thermoelectric properties of half-Heusler alloys using first-principles simulations as well as inelastic neutron scattering experiments. The field of thermoelectrics was introduced discussing thermoelectric materials, real-world applications, and approaches to optimise performance. In Chapter 2, the required theoretical framework underpinning the first-principles calculations was laid out. Whereas, Chapter 3 contains the methodology required to perform and repeat the simulations and experiments found in this work.

Chapter 4, examines the effects of interstitial Ni and Cu defects on the vibrational spectra and lattice component of the thermal conductivity in n-type XNiSn (X = Ti, Zr, Hf) based compositions. The results begin by presenting the benchmark calculations of the stoichiometric materials, showing good agreement with the literature. Results of the unfolded phonon spectra and neutron weighted phonon DOS are presented for defective supercells containing interstitials. In-depth analysis of Ni interstitials has shown that a clustered model in which Ni interstitials are found in clusters of neighbouring vacancy sites results in the best agreement with the experimentally measured phonon DOS. In addition, a significant level of phonon broadening was found in the presence of both Ni and Cu interstitials, which can act to reduce the phonon lifetimes and lower the κ_{lat}. This was followed by calculations of κ_{lat} and the effect of grain boundaries in $TiNi_{1+x}Sn$ using the homogeneous Ni defect model, here the Ni interstitials are placed on the same supercell vacancy site in each periodic repetition of the supercell with no clustering on neighbouring vacancy sites. This has revealed a large reduction in the κ_{lat} for the defective composition when computed via both the iterative solution of the phonon BTE approach and the modified Debye-Callaway model. A significant impact of grain boundaries can be seen on lowering the value of κ_{lat}, providing an additional optimisation mechanism via modification of the material synthesis process. Therefore, the ability to model the different configurations of complex defective structures in these materials has yielded a greater understanding of the possible microstructure in the real system. This is a novel set of calculations and we have not come across previous attempts of obtaining the κ_{lat} using

a full iterative solution of the phonon BTE for defective structures which originate from a supercell model.

In Chapter 5, we investigate whether the presence of interstitials does not impede the electronic properties of $TiNi_{1+x}Sn$ and $TiNiCu_xSn$. Results of the calculations have shown the addition of interstitial Cu into the TiNiSn half-Heusler matrix provides an enhancement of the thermoelectric properties and can simultaneously serve as a dopant. Unlike in the case of Ni interstitials, no in-gap states were present for the $TiNiCu_xSn$ composition that could otherwise lead to carrier scattering and impede carrier mobility, suggesting Cu is the better choice which is in agreement with experiment. The discrepancy between the experimentally observed semi-conducting and predicted metallic behaviour in the defective systems containing Ni and Cu interstitial was investigated by applying the Hubbard U model on the Ni d state electrons as well as through the use of the RSCAN meta-GAA exchange-correlation functional. The results did not reveal conclusive evidence for Mott like behaviour of the Ni electrons as the mechanism for charge compensation, but we can approximate the charge compensation to lie in the region between 1-2 electrons. We have also ruled out the choice of exchange-correlation functional as a source of error through the use of the RSCAN functional. This raises the question of potential existence of unknown microscopic origin, perhaps due to charge compensation at the grain boundaries or other defects that would merit an investigation.

Lastly, in Chapter 6, we compute the electronic structure properties of NbCoSb and NbCoSn half-Heusler alloys and their defective structures. Experimental structural measurements have shown a significant level of stable Nb vacancies lowering the average number of valence electrons to satisfy the half-Heusler 18-electron rule. This class of defect was modelled using the supercell approach, resulting in a prediction of semi-conducting behaviour in agreement with the experiments and good agreement with structural parameters, which had previously shown a large deviation for the stoichiometric NbCoSb system. The effect of Sn doping in $Nb_{0.9}CoSb_{0.5}Sn_{0.5}$ was explored, designed to satisfy the 18-electron rule through both Nb-site vacancy and substitution of 50% Sb with Sn. The outcome of computing the effective band structure predicted a band gap as well as band convergence at the CBM. Consequently, leading to a higher valley degeneracy and higher m^*_{dos} in good agreement with experiment. This also revealed the sensitivity of conduction bands to Sn concentration, suggesting an expected improvement in the Seebeck coefficient.

7.1 Future Research

Calculations of κ_{lat} of the clustered Ni interstitial model was not performed in this work due to a prohibitive computational expense. As the clustered Ni model provided good agreement with the experimental phonon DOS, future calculations of the clustered Ni defect model may provide a better prediction of the κ_{lat} in the real system. We have shown that calculation for estimating the κ_{lat} by solving the Boltzmann transport equation can

be used to investigate and provide insight in complex defective systems, which would not be possible to model using smaller simulation cells. However, it is clear that modelling of disordered systems requires large supercells and multiple configurations to reduce the uncertainty of a particular defect model and its ability to correctly model the real system. This is a clear limitation of the method, where a degree of mismatch with experiment is to be expected and improvements through the increase of supercell size carry a large increase in the computational expense.

Regarding the mismatch in the experimental measurement of a semi-conducting state and a prediction of a metallic state for the electronic structure properties of compositions involving Ni and Cu interstitials in Chapter 5. Further studies could consider investigating applying the Hubbard U parameter to additional states or alternative treatments of correlated systems using approaches such as DFT + DMFT [135] or model the effects of other charge compensation mechanisms due to grain boundaries or impurity defects. In addition, it has been shown in Chapter 4 that clustered Ni model provides a better description of the nature of lattice dynamics, an obvious route would be to consider Ni clustering to determine the potential impact on the electronic structure. Furthermore, the method used in this work to compute m^*_{dos} has consistently shown reasonable agreement with experimental findings, showing that this method has value for calculations of m^*_{dos} in a range of material compositions.

Different orderings of the Nb vacancies should be considered to determine the consequences on the electronic structure properties. Additional mechanisms for optimisation of thermoelectric properties and achieving band convergence to increase valley degeneracy, such as the role of interstitial defects are of considerable interest. Moreover, studies of thermal transport properties to understand the effect of Nb vacancies on the vibrational spectra and thermal conductivity can provide a route to further optimisation of the thermoelectric properties in these materials.

References

[1] S. A. Barczak, R. J. Quinn, J. E. Halpin, K. Domosud, R. I. Smith, A. R. Baker, E. Don, I. Forbes, K. Refson, D. A. MacLaren, and J. W. G. Bos. Suppression of thermal conductivity without impeding electron mobility in n-type xnisn half-heusler thermoelectrics. *J. Mater. Chem. A*, 7:27124–27134, 2019.

[2] R. Freer and A. V. Powell. Realising the potential of thermoelectric technology: a roadmap. *J. Mater. Chem. C*, 8:441–463, 2020.

[3] Byeongmoon Lee, Hyeon Cho, Kyung Tae Park, Jin-Sang Kim, Min Park, Heesuk Kim, Yongtaek Hong, and Seungjun Chung. High-performance compliant thermoelectric generators with magnetically self-assembled soft heat conductors for self-powered wearable electronics. *Nature Communications*, 11(5948), 2020.

[4] Yu Xiao and Li-Dong. Zhao. Charge and phonon transport in PbTe-based thermoelectric materials. *npj Quantum Materials*, 3(55), 2018.

[5] K. Momma and F. Izumi. Vesta 3 for three-dimensional visualization of crystal, volumetric and morphology data. *Journal of Applied Crystallography*, 44:1272–1276, 2011.

[6] Krishna M. Chaturvedi. Synthesis and investigation of thermo-electric properties of skutterudites $CoSb_3$/graphene particles nanocomposite. Master's thesis, Amity University, 2014.

[7] Keith Refson. Introduction to DFT and the plane-wave pseudopotential method. https://www.archer.ac.uk/training/course-material/2014/04/PMMP_UCL/Slides/castep_1.pdf, 2014.

[8] Duc. Le. personal communication, 2021.

[9] J. W. G. Bos. personal communication, 2021.

[10] Jiangtao Wei, Liangliang Yang, Peishuai Song Zhe Ma, Mingliang Zhang, Jing Ma, Fuhua Yang, and Xiaodong Wang. Review of current high-ZT thermoelectric materials. *Journal of Materials Science*, 55:12642–12704, 2020.

[11] Genadi A. Naydenov. First principles modelling of thermoelectric materials, 2019.

[12] MarketResearchEngine. Global thermoelectric generators market research report - industry analysis, size, share, growth, trends and forecast, 2021-2026. http://marketresearchengine.com/reportdetails/thermoelectric-generators-market-research-report, 2021.

[13] Markets and Markets. Thermoelectric generators market by application (waste heat recovery, energy harvesting, direct power generation, co-generation), wattage (<10 w, 10-1kw, >1kw), temperature (<80°c, 80°- 500°c, >500°c, material, vertical, component, region - global forecast to 2025. https://www.marketsandmarkets.com/Market-Reports/thermoelectric-generators-market-91553904.html#:~:text=%5B165%20Pages%20Report%5D%20The%20thermoelectric,8.3%25%

20during%20the%20forecast%20period.&text=Thermoelectric%20generators%20play%20an%20essential,efficiency%20by%20utilizing%20waste%20heat., 2019.

[14] J. Yang and F. R. Stabler. Automotive applications of thermoelectric materials. *Journal of Electronic Materials*, 38:1245–1251, 2009.

[15] R. Bechtel. Multi-mission radioisotope thermoelectric generator (mmrtg). https://mars.nasa.gov/mars2020/files/mep/MMRTG_FactSheet_update_10-2-13.pdf, 2020.

[16] A. Schock. RTGs using PbTe/TAGS thermoelectric elements for Mars environmental survey (Mesur) mission. https://www.osti.gov/servlets/purl/1033397, 1992.

[17] L. Baker. Coolmed launch the coolmed portable vaccine carrier to help with the covid vaccination roll-out. https://healthcare-newsdesk.co.uk/coolmed-launch-the-coolmed-portable-vaccine-carrier-to-help-with-the-covid\-vaccination-roll-out/, 2021.

[18] Dongna Shen, Jung-Hyun Park, Joo Hyon Noh, Song-Yul Choe, Seung-Hyun Kim, Howard C. Wikle, and Dong-Joo Kim. Micromachined PZT cantilever based on SOI structure for low frequency vibration energy harvesting. *Sensors and Actuators A: Physical*, 154(1):103–108, 2009.

[19] Huaizhou Zhao, Jiehe Sui, Zhongjia Tang, Yucheng Lan, Qing Jie, Daniel Kraemer, Kenneth McEnaney, Arnold Guloy, Gang Chen, and Zhifeng Ren. High thermoelectric performance of MgAgSb-based materials. *Nano Energy*, 7:97–103, 2014.

[20] Yixuan Shi, Cheryl Sturm, and Holger Kleinke. Chalcogenides as thermoelectric materials. *Journal of Solid State Chemistry*, 270:273–279, 2019.

[21] Xiao-Lei Shi, Xinyong Tao, Jin Zou, and Zhi-Gang Chen. High-performance thermoelectric snse: Aqueous synthesis, innovations, and challenges. *Advanced Science*, 7(7):1902923, 2020.

[22] S Joseph Poon. Half heusler compounds: promising materials for mid-to-high temperature thermoelectric conversion. *Journal of Physics D: Applied Physics*, 52(49):493001, Sep 2019.

[23] Chenguang Fu, Shengqiang Bai, Yintu Liu, Yunshan Tang, Lidong Chen, Xinbing Zhao, and Tiejun Zhu. Realizing high figure of merit in heavy-band p-type half-heusler thermoelectric materials. *Nature Communications*, 6, 2015.

[24] S.N.H Eliassen. A first principles study of lattice thermal conductivity in XNiSn (X = Ti, Zr, Hf) half-Heusler alloys for thermoelectric applications. Master's thesis, University of Oslo, Department of Physics, 2016.

[25] L. Huang, Q. Zhang, Y. Wang, R. He, J. Shuai, J. Zhang, C. Wang, and Z. Ren. The effect of sn doping on thermoelectric performance of n-type half-heusler NbCoSb. *Phys. Chem. Chem. Phys*, 19:25683, 2017.

[26] Son D.N. Luu and Paz Vaquiero. Layered oxychalcogenides: Structural chemistry and thermoelectric properties. *Journal of Materiomics*, 2:131–140, 2016.

[27] G. Nolas, D. Morelli, and T.M. Tritt. Skutterudites: a phonon-glass-electron crystal approach to advanced thermoelectric energy conversion applications. *Ann. Rev. Matter. Sci.*, 29:89–116, 2003.

[28] Juli-Anna Dolyniuk, Bryan Owens-Baird, Jian Wang, Julia V. Zaikina, and Kirill Kovnir. Clathrate thermoelectrics. *Materials Science and Engineering: R: Reports*, 108:1–46, 2016.

[29] Jaime Andrés Pérez-Taborda, Olga Caballero-Calero, and Marisol Martín-González. Silicon-germanium (sige) nanostructures for thermoelectric devices: Recent advances and new approaches to high thermoelectric efficiency. In Vitalyi Igorevich Talanin, editor, *New Research on Silicon*, chapter 8. IntechOpen, Rijeka, 2017.

[30] W. B. Fowler. Point defects. *Encyclopedia of Condensed Matter Physics*, pages 318–323, 2005.

[31] Edmund G. Seebauer and Meredith C. Kratzer. Extrinsic defects. in: Charged semiconductor defects. *Engineering Materials and Processes. Springer, London*, pages 233–289, 2009.

[32] Matt Beekman, Donald T. Morelli, and George S. Nolas. Better thermoelectrics through glass-like crystals. *Nature Materials*, 14:1182–1185, 2015.

[33] Dr. Zhong-Zhen Luo, Songting Cai, Dr. Shiqiang Hao, Dr. Trevor P. Bailey, Dr. Ioannis Spanopoulos, Dr. Yubo Luo, Prof. Jianwei Xu, Prof. Ctirad Uher, Prof. Christopher Wolverton, Prof. Vinayak P. Dravid, Prof. Qingyu Yan, and Prof. Mercouri G. Kanatzidis. Strong valence band convergence to enhance thermoelectric performance in PbSe with two chemically independent controls. *Angewandte Chemie*, 133:272–277, 2020.

[34] Joseph P. Heremans, Bartlomiej Wiendlocha, and Audrey M. Chamoire. Resonant levels in bulk thermoelectric semiconductors. *Energy and Environmental Science*, 5:5510–5530, 2012.

[35] Adam A. Wilson, Patrick J. Taylor, Ddaniel S. Choi, and Shashi P. Karna. Grain boundary engineering for thermal conductivity reduction in bulk nanostructured thermoelectric materials. In S. Skipidarov and M. Nikitin, editors, *Novel Thermoelectric Materials and Device Design Concepts*, pages 255–275. Springer, Cham, 2019.

[36] Sang Il Kim, Kyu Hyoung Lee, Hyeon A Mun, Hyun Sik Kim, Sung Woo Hwang, Jong Wook Roh, Dae Jin Yang, Weon Ho Shin1, Xiang Shu Li, Young Hee Lee, G. Jeffrey Snyder, and Sung Wng Kim. Dense dislocation arrays embedded in grain boundaries for high-performance bulk thermoelectrics. *Science*, 348:109–114, 2015.

[37] Mildred S. Dresselhaus, Gang Chen, Ming Y. Tang, Ronggui Yang, Hohyun Lee, Dezhi Wang, Zhifeng Ren, Jean-Pierre Fleurial, and Pawan Gogna. New directions for low-dimensionalthermoelectric materials. *Advanced Materials*, 19:1043–1053, 2007.

[38] Kanishka Biswas, Jiaqing He, Ivan D. Blum, Chun-I Wu, Timothy P. Hogan, David N. Seidman, Vinayak P. Dravid, and Mercouri G. Kanatzidis. High-performance bulk thermoelectrics with all-scale hierarchical architectures. *Nature*, 489:414–418, 2012.

[39] B. Poudel, Y. Ma Q. Hao, Y. Lan, A. Minnich, B. Yu, and et al. High-thermoelectric performance of nanostructured bismuth antimony telluride bulk alloys. *Science*, 320:634–638, 2008.

[40] X. W. Wang, H. Lee, Y. C. Lan, G. H. Zhu, G. Joshi, D. Z. Wang, J. Yang, A. J. Muto, M. Y. Tang, J. Klatsky, S. Song, M. S. Dresselhaus, G. Chen, and Z. F. Ren. Enhanced thermoelectric figure of merit in nanostructured n-type Silicon Germanium bulk alloy. *Applied Physics Letters*, 93(19):193121, 2008.

[41] Wei Xu, Yong Liu, Bo Chen, Da-Bo Liu, Yuan-Hua Lin, and Augusto Marcelli. Nano-inclusions: a novel approach to tune the thermal conductivity of In_2O_3. *Phys. Chem. Chem. Phys*, 15:17595–17600, 2013.

[42] Keith T. Regner, Daniel P. Sellan, Zonghui Su, Cristina H. Amon, Alan J.H. McGaughey, and Jonathan A. Malen. Broadband phonon mean free path contributions to thermal conductivity measured using frequency domain thermoreflectance. *Nature Communications*, 4:1640, 2013.

[43] Zhi-Gang Chen, Guang Han, Lei Yang, Lina Cheng, and Jin Zou. Nanostructured thermoelectric materials: Current research and future challenge. *Progress in Natural Science: Materials International*, 22:535–549, 2012.

[44] Wei Chen, Jan-Hendrik Pöhls, Geoffroy Hautier, Danny Broberg, Saurabh Bajaj, Umut Aydemir, Zachary M. Gibbs, Hong Zhu, Mark Asta, G. Jeffrey Snyder, Bryce Meredig, Mary Anne White, Kristin Perssonae, and Anubhav Jain. Understanding thermoelectric properties from high-throughput calculations: trends, insights, and comparisons with experiment. *Journal of Materials Chemistry C*, 4:4414–4426, 2016.

[45] Georg K.H. Madsen and David J.Singh. BoltzTraP. a code for calculating band-structure dependent quantities. *Computer Physics Communications*, 175:67–71, 2006.

[46] Georg K.H. Madsen, Jesús Carrete, and Matthieu J.Verstraete. BoltzTraP2, a program for interpolating band structures and calculating semi-classical transport coefficients. *Computer Physics Communications*, 231:140–145, 2018.

[47] Giovanni Pizzi, Dmitri Volja, Boris Kozinsky, Marco Fornari, and Nicola Marzari. BoltzWann: A code for the evaluation of thermoelectric and electronic transport properties with a maximally-localized wannier functions basis. *Computer Physics Communications*, 185:422–429, 2014.

[48] Wu Li, Jesús Carrete, Nebil A. Katcho, and Natalio Mingo. ShengBTE: a solver of the Boltzmann transport equation for phonons. *Comp. Phys. Commun.*, 185:1747–1758, 2014.

[49] Jesús Carrete, Bjorn Vermeersch, Ankita Katre, Ambroise van Roekeghem, Tao Wang, Georg K.H.Madsen, and Natalio Mingo. almaBTE : A solver of the space–time dependent Boltzmann transport equation for phonons in structured materials. *Computer Physics Communications*, 220:351–362, 2017.

[50] Atsushi Togo, Laurent Chaput, and Isao Tanaka. Distributions of phonon lifetimes in brillouin zones. *Phys. Rev. B*, 91:094306, Mar 2015.

[51] S. J. Clark, M. D. Segall, C. J. Pickard, P. J. Hasnip, M. J. Probert, and M. C. Payne K. Refson. First principles methods using castep. *Zeitschrift fuer Kristallographie*, 220(5-6):567–570, 2005.

[52] Paolo Giannozzi, Stefano Baroni, Nicola Bonini, Matteo Calandra, Roberto Car, Carlo Cavazzoni, Davide Ceresoli, Guido L Chiarotti, Matteo Cococcioni, Ismaila Dabo, Andrea Dal Corso, Stefano de Gironcoli, Stefano Fabris, Guido Fratesi, Ralph Gebauer, Uwe Gerstmann, Christos Gougoussis, Anton Kokalj, Michele Lazzeri, Layla Martin-Samos, Nicola Marzari, Francesco Mauri, Riccardo Mazzarello, Stefano Paolini, Alfredo Pasquarello, Lorenzo Paulatto, Carlo Sbraccia, Sandro Scandolo, Gabriele Sclauzero, Ari P Seitsonen, Alexander Smogunov, Paolo Umari, and Renata M Wentzcovitch. Quantum espresso: a modular and open-source software project for quantum simulations of materials. *Journal of Physics: Condensed Matter*, 21(39):395502 (19pp), 2009.

[53] G. Kresse and J. Furthmüller. Efficiency of ab-initio total energy calculations for metals and semiconductors using a plane-wave basis set. *Computational Materials Science*, 6:15–50, 1996.

[54] Tao Fan and Artem R. Oganov. Aicon: A program for calculating thermal conductivity quickly and accurately. *Computer Physics Communications*, 251:107074, Jun 2020.

[55] Atsushi Togo and Isao Tanaka. First principles phonon calculations in materials science. *Scripta Materialia*, 108:1–5, 2015.

[56] T. M. Tritt. Thermoelectric materials: Principles, structure, properties, and applications. *Encyclopedia of Materials: Science and Technology (Second Edition)*, pages Pages 1 – 11, 2002.

[57] D. M. Rowe. *CRC handbook of thermoelectrics. 1st edition. Boca Raton*. CRC Press, 1995.

[58] C. Kittel. *Introduction to Solid State Physics 8th Ed.* John Wiley and Sons, 2004.

[59] Philip J. Hasnip, Keith Refson, Matt I. J. Probert, Jonathan R. Yates, Stewart J. Clark, and Chris J. Pickard. Density functional theory in the solid state. *Philosophical Transactions of the Royal Society A: Mathematical, Physical and Engineering Sciences*, 372(2011):20130270, 2014.

[60] Attila Szabo and Neil S. Ostlund. *Modern Quantum Chemistry: Introduction to Advanced Electronic Structure Theory*. Dover Publications, Inc., Mineola, first edition, 1996.

[61] P. Hohenberg and W. Kohn. Inhomogeneous electron gas. *Phys. Rev.*, 136:B864–B871, Nov 1964.

[62] W. Kohn and L. J. Sham. Self-consistent equations including exchange and correlation effects. *Phys. Rev.*, 140:A1133–A1138, Nov 1965.

[63] Feliciano Giustino. *Materials modelling using density functional theory : properties and predictions / Feliciano Giustino.* Oxford University Press, Oxford, England ; New York, New York, 2014.

[64] Tsuneda Takao and Hirao Kimihiko. Self-interaction corrections in density functional theory. *The Journal of Chemical Physics*, 140, 04 2014.

[65] Bernd Meyer. The pseudopotential plane wave approach. *Computational Nanoscience: Do It Yourself!*, 31:71–83, 2006.

[66] Robert G. Parr and Weitao Yang. *Density-Functional Theory of Atoms and Molecules*. Oxford University Press, 1994.

[67] Yiqun Wang, Danilo Puggioni, and James M. Rondinelli. Assessing exchange-correlation functional performance in the chalcogenide lacunar spinels GaM_4Q_8 $(m = \mathrm{Mo, V, Nb, Ta}; q = \mathrm{S, Se})$. *Phys. Rev. B*, 100:115149, Sep 2019.

[68] D. M. Ceperley and B. J. Alder. Ground state of the electron gas by a stochastic method. *Phys. Rev. Lett.*, 45:566–569, Aug 1980.

[69] John P. Perdew, Kieron Burke, and Matthias Ernzerhof. Generalized gradient approximation made simple. *Phys. Rev. Lett.*, 77:3865–3868, Oct 1996.

[70] Jiri Klimes, David Bowler, and Angelos Michaelides. Chemical accuracy for the van der Waals density functional. *Journal of physics. Condensed matter : an Institute of Physics journal*, 22:022201, 01 2010.

[71] Burak Himmetoglu, Andrea Floris, Stefano de Gironcoli, and Matteo Cococcioni. Hubbard-corrected dft energy functionals: The lda+u description of correlated systems. *International Journal of Quantum Chemistry*, 114(1):14–49, 2014.

[72] J. Hubbard. Electron correlations in narrow energy bands III. an improved solution. *Proc. R. Soc. Lond. A*, 281:401–419, 1964.

[73] Alex Willand, Yaroslav O. Kvashnin, Luigi Genovese, Álvaro Vázquez-Mayagoitia, Arpan Krishna Deb, Ali Sadeghi, Thierry Deutsch, and Stefan Goedecker. Norm-conserving pseudopotentials with chemical accuracy compared to all-electron calculations. *The Journal of Chemical Physics*, 138(10):104109, 2013.

[74] Gokhan Ozgur. The effective mass theory. https://s2.smu.edu/ee/smuphotonics/Gain/CoursePresentationFall03/Effective_Mass_Theory_July25-03.pdf, 2003.

[75] Dragica Vasileska. Simplified band-structure models and carrier dynamics. https://nanohub.org/resources/1522/download/simplifiedbandstructurecarrierdynamics_word.pdf, 2021[Online].

[76] Masatsugu Suzuki and Itsuko S. Suzuki. *Lattice Waves, Lecture Note on Solid State Physics*. Department of Physics, State University of New York, Binghamton, 2017.

[77] Atsushi Togo and Isao Tanaka. First principles phonon calculations in materials science. *Scripta Materialia*, 108:1–5, 2015.

[78] Martin T. Dove. *Introduction to Lattice Dynamics*. Cambridge Topics in Mineral Physics and Chemistry. Cambridge University Press, 1993.

[79] Keith Refson, Paul R. Tulip, and Stewart J. Clark. Variational density-functional perturbation theory for dielectrics and lattice dynamics. *Phys. Rev. B*, 73:155114, Apr 2006.

[80] Martin T. Dove. *An atomic view of Materials*. Oxford University Press, 2003.

[81] G Kresse, J Furthmüller, and J Hafner. *Ab initio* force constant approach to phonon dispersion relations of diamond and graphite. *Europhysics Letters (EPL)*, 32(9):729–734, dec 1995.

[82] Stefano Baroni, Paolo Giannozzi, and Andrea Testa. Green's-function approach to linear response in solids. *Phys. Rev. Lett.*, 58:1861–1864, May 1987.

[83] Peter Byrne. Lattice dynamics. https://www-users.york.ac.uk/~mijp1/teaching/grad_FPMM/lecture_notes/lec13_14_phonons.pdf, 2019.

[84] Keith Refson. Vibrational spectroscopy methods. http://www.castep.org/files/workshop_lectures_2012/Phonons_Spectroscopy-print.pdf, 2012.

[85] Jonathan H. Lloyd-Williams and Bartomeu Monserrat. Lattice dynamics and electron-phonon coupling calculations using non-diagonal supercells. *Phys. Rev. B*, 92:184301, Nov 2015.

[86] Stefano Baroni, Stefano de Gironcoli, Andrea Dal Corso, and Paolo Giannozzi. Phonons and related crystal properties from density-functional perturbation theory. *Rev. Mod. Phys.*, 73:515–562, Jul 2001.

[87] R. M. Sternheimer. Electronic polarizabilities of ions from the hartree-fock wave functions. *Phys. Rev.*, 96:951–968, Nov 1954.

[88] Xavier Gonze. Perturbation expansion of variational principles at arbitrary order. *Phys. Rev. A*, 52:1086–1095, Aug 1995.

[89] Stefano Baroni, Stefano de Gironcoli, Andrea Dal Corso, and Paolo Giannozzi. Phonons and related crystal properties from density-functional perturbation theory. *Rev. Mod. Phys.*, 73:515–562, Jul 2001.

[90] Voicu Popescu and Alex Zunger. Extracting **e** versus **k** effective band structure from supercell calculations on alloys and impurities. *Phys. Rev. B*, 85:085201, Feb 2012.

[91] Fawei Zheng and Ping Zhang. Phonon unfolding: A program for unfolding phonon dispersions of materials. *Computer Physics Communications*, 210:139–144, 2017.

[92] Amelia Carolina Sparavigna. The Boltzmann equation of phonon thermal transport solved in the relaxation time approximation – I – Theory. *Mechanics, Materials Science Engineering Journal*, pages 34–45, 2016.

[93] Yongsheng Zhang. First-principles Debye–Callaway approach to lattice thermal conductivity. *Journal of Materiomics*, 2:237–247, 2016.

[94] Hendrik J. Monkhorst and James D. Pack. Special points for brillouin-zone integrations. *Phys. Rev. B*, 13:5188–5192, Jun 1976.

[95] M. R. Jarvis, I. D. White, R. W. Godby, and M. C. Payne. Supercell technique for total-energy calculations of finite charged and polar systems. *Physical Review B*, 56(23):14972–14978, Dec 1997.

[96] Péter Pulay. Convergence acceleration of iterative sequences. the case of scf iteration. *Chemical Physics Letters*, 73(2):393–398, 1980.

[97] J. Neugebauer P. Kratzer. The basics of electronic structure theory for periodic systems. *Front Chem*, 7, 2019.

[98] R. Fletcher. *Practical methods of optimization*. Wiley, 1987.

[99] Jolyon Aarons. A new castep and onetep geometry optimiser. http://www.hector.ac.uk/cse/distributedcse/reports/castep-geom/castep-geom/HTML/dCSE_project.html, 2011.

[100] A. P. Bartók and J. R. Yates. Regularized scan functional. *J. Chem. Phys*, 150:161101, 2019.

[101] Larry Wall, Tom Christiansen, and Jon Orwant. *Programming Perl*. " O'Reilly Media, Inc.", 2000.

[102] James M. Ortega. *Introduction to FORTRAN 90 for Scientific Computing*. Oxford University Press, Inc., 1994.

[103] P. Brommer and D. Quigley. Automated effective band structures for defective and mismatched supercells. *Journal of Physics: Condensed Matter*, 26(48):485501, 2014.

[104] Andrew J. Morris, Rebecca J. Nicholls, Chris J. Pickard, and Jonathan R. Yates. Optados: A tool for obtaining density of states, core-level and optical spectra from electronic structure codes. *Comput. Phys. Commun.*, 185(5):1477–1485, 2014.

[105] A. Fonari and C. Sutton. Effective mass calculator. 2012.

[106] Mari. https://www.isis.stfc.ac.uk/Pages/mari.aspx, 2021.

[107] Samarath L. Chaplot, Narayani Choudhry, Subrata Ghose, Mala N. Rao, Ranjan Mittal, and Prabhatasree Goel. Inelastic neutron scattering and lattice dynamics of minerals. *Eur. J. Mineral*, 14:291–329, 2002.

[108] R.Mittal and et al. Spin-phonon coupling in $K_{0.8}Fe_{1.6}Se_2$ and KFe_2Se_2: Inelastic neutron scattering and ab initio phonon calculations. *Physical Review B*, 87:184502, 2013.

[109] et al. O. Arnold. Mantid - data analysis and visualization package for neutron scattering and μSR experiments. *Nuclear Instruments and Methods in Physics Research Section A*, 764:156–166, November 2014.

[110] Varley F. Sears. Neutron scattering lengths and cross sections. *Neutron News*, 3:26–37, 1992.

[111] Ian T. Witting, Thomas C. Chasapis, Francesco Ricci, Matthew Peters, Nicholas A. Heinz, Geoffroy Hautier, and G. Jeffrey Snyder. The thermoelectric properties of bismuth telluride. *Advanced Electronic Materials*, 5(6):1800904, 2019.

[112] S. Sakurada and N. Shutoh. Effect of Ti substitution on the thermoelectric properties of (Zr, Hf)NiSn half-Heusler compounds. *Appl. Phys. Lett.*, 86:082105, 2005.

[113] S. Bhattacharya, M. J. Skove, M. Russell, and T.M Tritt et al. Effect of boundary scattering on the thermal conductivity of TiNiSn-based half-heusler alloys. *Phys. Rev. B*, 77:184203, 2008.

[114] Wu Li, Jesús Carrete, Nebil A. Katcho, and Natalio Mingo. ShengBTE: a solver of the Boltzmann transport equation for phonons. *Comp. Phys. Commun.*, 185:1747–1758, 2014.

[115] J. D. Hunter. Matplotlib: A 2d graphics environment. *Computing in Science & Engineering*, 9(3):90–95, 2007.

[116] Genadi Naydenov. Castep2shengbte interface. https://github.com/ganphys/castep2shengbte, 2017.

[117] R. A. Downie, S. A. Barczak, S. A. Smith, and J. W. G. Bos. Compositions and thermoelectric properties of XNiSn (x = Ti, Zr, Hf) half-heusler alloys. *J. Mater. Chem . C*, 3:10534–10542, 2015.

[118] N. Nakanishi, A. Nagasawa, and Y. Murakami. LATTICE STABILITY AND SOFT MODES. *Journal de Physique Colloques*, 43(C4):C4–35–C4–55, 1982.

[119] J. S. Young and R. G. Reddy. Processing and thermoelectric properties of tinisn materials: A review. *Journal of Materials Engineering and Performance*, 28, 5917-5930, 2019.

[120] Meena Rittiruam, Anucha Yangthaisong, and Tosawat Seetawan. Enhancing the thermoelectric performance of self-defect tinisn: A first-principles calculation. *Journal of Electronic Materials*, 47:7456–7462, 2018.

[121] Jason E. Douglas, Philip A. Chater, Craig M. Brown, Tresa M. Pollock, and Ram Seshadri. Nanoscale structural heterogeneity in ni-rich half-heusler tinisn. *Journal of Applied Physics*, 116(16):163514, 2014.

[122] R. A. Downie, D. A. Maclaren, and J-W. G. Bos. Thermoelectric performance of multiphase XNiSn (x = ti, zr, hf) half-heusler alloys. *Journal of Materials Chemistry A*, 2:6107–6114, 2014.

[123] S. D Mahanti Dat T. Do and Jiji J. Pulikkoti. Electronic structure of Zr–Ni–Sn systems: role of clustering and nanostructures in half-Heusler and Heusler limits. *Journal of Physics: Condensed Matter*, 26(27):275501, Jun 2014.

[124] Lianhua He, Fang Liu, Geoffroy Hautier, Micael J. T. Oliveira, Miguel A. L. Marques, Fernando D. Vila, J. J. Rehr, G.-M. Rignanese, and Aihui Zhou. Accuracy of generalized gradient approximation functionals for density-functional perturbation theory calculations. *Phys. Rev. B*, 89:064305, Feb 2014.

[125] L. Andrea, G. Hug, and L. Chaput. Ab initio phonon properties of half-heusler NiTiSn, NiZrSn and NiHfSn. *Journal of Physics: Condensed Matter*, 27(42):425401, 2015.

[126] S. Bhattacharya, M. J. Skove, M. Russell, and T.M Tritt et al. Processing and thermoelectric properties of TiNiSn materials: A review. *Journal of Materials Engineering and Performance*, 28:5917–5930, 2019.

[127] Jeffrey D Germond, Paul J Schilling, Nathan J. Takas, and Pierre F. P. Poudeu. Thermoelectric performance of nanostructured zrnisn compounds synthesized by mechanical alloying. *MRS Proceedings*, 1267:1267–DD03–12, 2010.

[128] F. G. Aliev. Gap at fermi level in some new d- and f-electron intermetallic compounds. *Physica B: Condensed Matter*, 171:199–205, 1991.

[129] Alexandre Berche and Philippe Jund. Fully ab-initio determination of the thermoelectric properties of half-heusler nitisn: Crucial role of interstitial ni defects. *Materials*, 11(6), 2018.

[130] A. N. Gandi and U. Schwingenschlöogl. Electron dominated thermoelectric response in MNiSn (M: Ti, Zr, Hf) half-heusler alloys. *Phys. Chem. Chem Phys.*, 18:14017, 2016.

[131] Hidetoshi Miyazaki, Osman Murat Ozkendir, Selen Gunaydin, Kosuke Watanabe, Kazuo Soda, and Yoichi Nishino. Probing local distortion around structural defects in half-heusler thermoelectric NiZrSn alloy. *Scientific Reports*, 10:19820, 2020.

[132] Lucy D. Whalley, Jarvist M. Frost, Benjamin J. Morgan, and Aron Walsh. Impact of nonparabolic electronic band structure on the optical and transport properties of photovoltaic materials. *Phys. Rev. B*, 99:085207, Feb 2019.

[133] Sarah A. Tolba, Kareem M. Gameel, Basant A. Ali, Hossam A. Almossalami, and Nageh K. Allam. The dft+u: Approaches, accuracy, and applications. 2018.

[134] Colinet Catherine, Philippe Jund, and Jean-Claude Tedenac. NiTiSn a material of technological interest: Ab initio calculations of phase stability and defects. *Intermetallics, Elsevier*, 46:103–110, 2013.

[135] E. Pavarini, E. Koch, D. Vollhardt, and A. Lichtenstein. The LDA+DMFT approach to strongly correlated materials. *Deutsche Nationalbibliothek, Forschungszentrum, Julich*, 2011.

[136] Jian He and Terry M. Tritt. Advances in thermoelectric materials research: Looking back and moving forward. *Science*, 357(6358), 2017.

[137] L. Huang, Y. Wang, G. Samsonidze, B. Kozinsky, Q. Zhang, and Z. Ren. Enhanced thermoelectric properties of n-type NbCoSn half-heusler by improving phase purity. *APL Mater*, 4:104804, 2016.

[138] H. B. Ozisik, E. Deligoz, H. Ozisik, and E. Ateser. Phonon transport properties of NbCoSb compound. *Mater. Res. Express*, 7:025004, 2020.

[139] G. Zhang and et al. Performance of various density-functional approximations for cohesive properties of 64 bulk solids. *New. J. Phys*, 20:063020, 2018.

[140] F. Serrano-Sánchez, T. Luo, J. Yu, and et al. Thermoelectric properties of n-type half-heusler NbCoSn with heavy-element Pt substitution. *J. Mater. Chem. A*, 8:14822–14828, 2020.

[141] D. A. Ferluccio, J. E. Halpin, K. L. MacIntosh, R. J. Quinn, E. Don, R. I. Smith, D. A. MacLaren, and J. G. Bos. Low thermal conductivity and promising thermoelectric performance in A_xCoSb (A = V, Nb or Ta) half-heuslers with inherent vacancies. *J. Mater. Chem. A*, 7:6539, 2019.

[142] Nikolaj Roth, Tiejun Zhub, and Bo B. Iversen. A simple model for vacancy order and disorder in defective half-heusler systems. *IUCrJ*, 7(4):673–680, 2020.

Appendix A

Experimental INS Results

Additional results of the inelastic neutron scattering measurements of the phonon DOS for the half-Heusler compositions of TiNiSn, ZrNiSn, HfNiSn,$Ti_{0.5}Zr_{0.5}NiSn$ and $Ti_{0.5}Zr_{0.25}Hf_{0.25}NiSn$ are provided to display the effects of binary and ternary X-site substitution and can be seen in Figure. A.1.

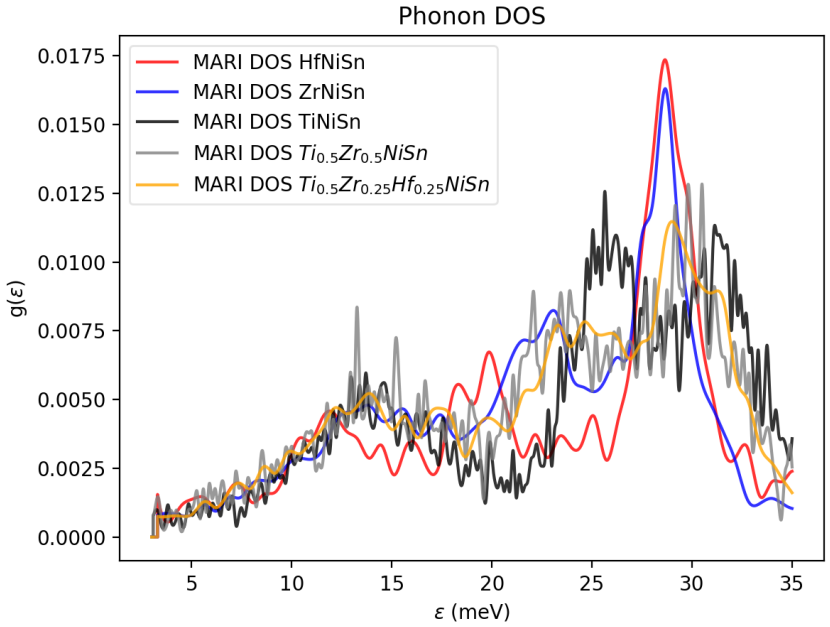

Fig. A.1 Experimental phonon DOS for TiNiSn, ZrNiSn, HfNiSn, $Ti_{0.5}Zr_{0.5}NiSn$ and $Ti_{0.5}Zr_{0.25}Hf_{0.25}NiSn$ as measured on the MARI instrument.

We can see that the introduced mass disorder due to the X-site substitution of TiNiSn with heavier elements of Zr and Hf. The largest effect can be seen from the down-shift of the high frequency optic phonon modes. Where the stoichiometric TiNiSn peaks at around 26 meV and 33 meV have down-shifted by about 3 meV. This suggests that mass-disorder scattering is the most effective at scattering the high frequency phonons in this system.